

## ON THE COVER

Globular clusters are one of the oldest structures in the galaxy and are known for their compactness and high stellar density. On page 46, Barton et al. propose that globular clusters were seeded from cosmic strings in the early universe.

The cover image shows the Milky Way with representations of globular clusters.





# BOARD 2015-2016

## Editors-in-Chief

Ariana Aimani  
*Computer Science & Biology*

Meng Zhang  
*Pharmacology*

## Managing Editors

Adam Pietrobon  
*Biochemistry*

Helen Lai  
*Biology*

Nick Pant  
*Electrical Engineering*

Sapan Patel  
*Anatomy & Cell Biology*

## Senior Editors

Jasmine Li-Brubacher  
*Biochemistry*

Lavinia Lee  
*Anatomy & Cell Biology*

Lindsay Brabant  
*Anatomy & Cell Biology*

Rachel Greben  
*Physiology*

Tatiana Sanchez  
*Psychology*

## Junior Editors

Aditya Mohan  
*Microbiology & Immunology*

Alexander Chatron-Michaud  
*Computer Science*

Sebastian Andric  
*Biology*

## Advisor

Victor Chisholm  
*Office for Undergraduate Research in Science*

## Layout Designer

Nick Pant

## Graphic Designer

Samer Richani  
*Architecture*



# TABLE OF CONTENTS

---

**7** Foreword

**9** Acknowledgements

## RESEARCH ARTICLES

**11** The Relationship between Large Herbivore Abundance and Algal Cover on Coral Reefs on West Coast Barbados  
*Vanessa Caron et al.*

**16** Scale-Invariant Adaptation in Response to Second-Order Electro-Sensory Stimuli in Weakly Electric Fish  
*Zhubo Zhang et al.*

**22** Preserved Vestibular Function in Mice with Loss of  $\alpha$ -9 Subunit of the  $\alpha$ -9/10 Nicotinic Acetylcholine Receptor ( $\alpha$ -9/10 nAChR)  
*Jesse Mendoza et al.*

**28** Reduction in Noise Correlation is Associated with Improved Behavioural Performance  
*Moushumi Nath et al.*

**32** Fluorescence Imaging of RANKL-mediated Calcium Oscillations in Osteoclasts  
*Mariya Stavnichuk et al.*

**36** Loss-of-Function Analysis Elucidates Essential Roles of eIF4E Isoforms in *Drosophila* Spermatogenesis  
*Liang Chen et al.*

**46** Cosmic Strings and the Origin of Globular Clusters  
*Alistair Barton et al.*

## REVIEW ARTICLES

**53** Understanding the 2013-2015 Ebola Outbreak  
*Janna Shapiro et al.*

**58** Dead but not gone: The case for PRL as a pseudophosphatase  
*Howie Wu et al.*



# FOREWORD

---

## **Dear Reader,**

We present to you a curation of some of the most forward thinking, novel, and innovative research done by undergraduates. This polished publication represents diligence and passion from our editors, and most importantly from our authors. The scientific process is rigorous as countless hours of planning, experimentation, analysis, discussion, and revision are done for every hypothesis that is developed in the many laboratories and research centers at McGill University and the world.

Each year, we receive an increasingly strong set of submissions from undergraduate students from around the globe. This year, we are proud to present to you two review papers and seven original research papers. We hope that MSURJ can continue provide a platform for students to inspire their peers and foster a vivacious scientific undergraduate community.

Almost 150 years after Sir William Osler (MDCM, 1872) started the first formal journal club, the McGill Science Undergraduate Research Journal continues to introduce research to undergraduates and forges a place for undergraduates in the McGill research community. As MSURJ is entering a brand new decade, its success is attributed to our hard working editorial board, our generous donors and most importantly you, our dedicated readers that support MSURJ's cause.

On behalf of the entire editorial board, we thank you.

**Ariana Aimani & Meng Zhang**  
**Co-Editors-in-Chief**



# ACKNOWLEDGEMENTS

---

The McGill Science Undergraduate Research Journal would like to thank its generous contributors without whom this journal would not have been possible.

We thank Dean Bruce Lennox who played a pivotal role in helping MSURJ set new goals for the upcoming decade, without his advice and expertise, MSURJ would not be the success it is currently. We would also like to thank the McGill Librarians for their help in transitioning MSURJ to an online electronic system. Lastly, we would like to acknowledge Mr. Victor Chisholm for his continuous support and guidance.

We thank all the donors in the McGill community for their generous support:

Faculty of Science  
Faculty of Medicine  
Department of Biochemistry  
Department of Biology  
Department of Pharmacology and Therapeutics  
Department of Physiology  
McGill Anatomy and Cell Biology Students' Society (MACSS)  
McGill Biology Student Union (MBSU)  
Biochemistry Undergraduate Society (BUGS)  
Microbiology and Immunology Students Association  
Science Undergraduate Society of McGill (SUS)

We extend our gratitude to the numerous peer reviewers who took the time to review all of the submissions. Lastly, we wish to recognize the student contributors whose efforts have made the journal possible.



Research Article

<sup>1</sup>School of Environment,  
McGill University, Montreal,  
QC, Canada

<sup>2</sup>Department of Biology, Mc-  
gill University, Montreal, QC,  
Canada

<sup>3</sup>Department of Biology,  
Dalhousie University, Halifax,  
NS, Canada

Vanessa Caron<sup>1</sup>, Ariel Greiner<sup>2</sup>, Krista Ransier<sup>3</sup>, Bryna Cameron-Steinke<sup>2</sup>

# The Relationship between Large Herbivore Abundance and Algal Cover on Coral Reefs on West Coast Barbados

Keywords

Grazing, eutrophication, water quality, top-down control, phase shifts

Email Correspondence

vanessa.caron@mail.mcgill.ca

## Abstract

**Background:** Over the past few decades, climate change and the intensification of coastal development significantly contributed to the degradation of coral reefs across the Caribbean Sea. Widespread increase in algal cover on coral reefs since the 1970s has made it difficult for the corals to recover. Thus, algae regulating factors, such as herbivorous grazers and groundwater nutrient concentrations, have important implications for the conservation of coral reefs. In this study we conducted a small-scale assessment of the relationship between the abundance of two families of herbivorous fishes, *Scaridae* and *Acanthuridae*, and algal cover on the coral reefs of West Coast Barbados was conducted, and we hypothesized that a direct negative correlation exists between them.

**Methods:** Herbivorous fish abundance and percent algal cover were quantified for three different coral reefs, and the data was analyzed using linear regressions and analyses of variance.

**Results:** We found that although there were no significant relationship between herbivorous fish abundance and algal cover, there was a significant difference between them across the three reefs studied. These results suggest the presence of other factors influencing algal cover. One such factor could potentially be groundwater input levels, which was found to differ at each of the three sites studied.

**Limitations:** The limited timeframe of this study did not allow for extensive sampling.

**Conclusion:** In order to effectively protect the coral reefs in Western Barbados, further studies are needed to increase the understanding of the relationship between herbivory and algal cover in Western Barbados as well as to further investigate the role of groundwater seepage on algal growth.

## Introduction

Many coral reef ecosystems around the world have shown a significant decline in coral cover and species diversity over the past four to five decades. Estimates suggest that 20% of the world's coral reefs are already lost, 20% are under imminent risk of collapse, and another 26% face threats of irreparable damage. (1) Such coral cover decline is attributed to indirect human disturbances including ocean warming, which cause coral bleaching and diseases the growth of human coastal populations, and overfishing of key herbivorous fishes, namely scarids and acanthurids. A loss of coral cover can result in a phase shift from coral to macroalgae dominance and cause further coral loss as coral death reduces competition for space, allowing algae to grow more easily. (2) In addition, excessive macroalgal cover is thought to harm coral reefs by reducing recruitment of juvenile corals from the plankton. (2)

Between 1983 and 1984, the entire Caribbean Sea experienced mass mortality of the sea urchin *Diadema antillarum*, an important algal grazer, due to a waterborne pathogen. Mortality rates ranged from 85% to 100%. (3) A significant decrease in herbivory on coral reefs and dramatic increases in algal cover ensued. (4) This event, combined with habitat loss as a result of increased coastal development, sedimentation, and eutrophication - the process by which excessive nutrients cause algal blooms and subsequent oxygen dead zones, was a strong contributor to the observed phase shift from corals to macroalgal-dominated reefs. Algal growth is promoted by eutrophication from groundwater seepage. Meanwhile, coral's ability to recover is hindered by many factors, including sedimentation, global warming, and reduced herbivory. The massive die offs of *Diadema*, and increased fishing pressure on herbivorous fish have therefore both con-

tributed to the lack of recovery of coral cover in Caribbean reefs. Herbivorous fishes are important in coral reef ecosystems because they reduce algal cover by grazing, contributing to the maintenance of reef health and the recovery of the reef from disturbances such as hurricanes. (5) Specifically, the families *Scaridae* (parrotfish) and *Acanthuridae* (surgeonfish) are thought to have the greatest impact on the regulation of algal cover via grazing, with adult scarids capable of maintaining 10% to 30% of a fore reef in a grazed state alone. (4) While damselfish (*Pomacentridae*) are also known grazers, their activity is confined to selectively maintaining algal "farms" in small territories, limiting their reef-wide impact on regulating benthic algae. (5)

In Barbados, the significance of herbivorous fishes' role as grazers in the coral reef ecosystem increased substantially with a 93.2% mortality of Barbadian *Diadema* populations from 1983 to 1984. (3) The increasing threats of overfishing and eutrophication on Barbados' reefs are bringing about lower numbers of herbivores and greater algal growth promotion, likely decreasing the health of the coral reef ecosystem. (6) To protect the reefs from algal dominance and loss of coral cover, one must first understand the extent of the top-down effects of herbivorous fish. The purpose of this study is to assess the relationship between the abundance of scarids and acanthurids and percent algal cover on the coral reefs of Western Barbados. We predict that a large abundance of scarids and acanthurids in an area will result in a low percent algal cover in that area.

## Methods

### Site Selection

Three individual coral reefs were selected along the West Coast of Barbados for sampling, which was done in May 2014. At each reef, scarid and acanthurid abundance and algal cover were measured. The sites were, from North to South: Mullin's Bay Beach, Folkestone Marine Reserve, and Sandy Lane Beach. The sites were chosen due to their proximity to one another (maximum distance of 11 km), as the focus of this study is to determine the small-scale effects of herbivore grazing on algal cover. This proximity enabled us to normalize the degree of coastal development, general oceanographic conditions, and physiography. One of our sites, the Folkestone Marine Reserve, is a Marine Protected Area in which fishing has been prohibited since 1981. (7) Fishing is permitted at the other two reefs.

### Data Collection - Set Up

At each site, data were collected along five 30-meter long transects extended perpendicular to the shoreline. At each reef, the transects were positioned a short distance beyond the crest of the reef (Fig. 1). This was done to ensure rough standardization of the water depth in each reef studied. Throughout the reef area studied, water depth ranged from 1 to 3.5 meters. The start of each transect was positioned by a snorkeler swimming on their back - thereby assuring a haphazard assignment of each transect location. From this point, a 15-meter long weighted rope marked with tape at 5-meter intervals was laid along the reef. A dive buoy, attached to the rope, was used at Mullin's Bay and Sandy Lane as boats were prevalent in both places. Because the placement of the transects created a disturbance, our team waited five minutes to allow fish to return to the area before beginning data collection. One group of two observers (Team 1) assessed herbivore abundance and water clarity while the other group of two (Team 2) assessed percent algal cover - these teams remained constant throughout all the observations, and the same person assessed water clarity at each site. While collecting data along the transect, a minimum distance of 10 meters was maintained between the two teams to ensure minimal disturbance for the fish. Once both teams reached the end of the 15-meter rope, Team 2 displaced the rope so that it covered the second half of the transect (15-30 meters), and then the process explained above was repeated starting at the 20-meter point. Data was not collected at the 0-meter and 15-meter marks, as pilot studies showed that setting-up the buoy and transect disturbed algal cover.

### Data Collection - Assessing Herbivore Abundance

At each five-meter mark, both observers of Team 1 completed two 360° turns on themselves, the first to count the number of acanthurids visible, and the second to count the number of scarids visible. All species within the two families were grouped together but juveniles of all of the species were ignored because they have been shown not to have a significant effect on algal abundance. (8) Both observers then recorded their results on slates with lead pencils. The number of scarids of three loosely defined and relative size ranges (small (~10cm), medium (~30cm), large (~50cm)) was recorded. Acanthurid abundance was recorded as the frequency of schools of 1, <10, 10-30, 30-50 individuals observed. This was done owing to acanthurids' proclivity for travelling in schools and the difficulty of recording exact number of fish in large schools moving away quickly. For data analysis, the number of observed acanthurids in a school was converted to a midpoint value (<10 was converted to 5, 10-30 to 20, and 30-50 to 40).

### Data Collection - Assessing Percent Algal Cover

Percent algal cover and grazing pressure at each 5-meter point along transects was estimated with a one square foot (929.03 cm<sup>2</sup>) quadrat. The quadrat was placed first to the left and then to the right of the rope at each meter mark (ignoring the 0-meter mark). At each position, a visual assessment of the percent algal cover and number of grazer marks observed in the quadrat was recorded by both observers on their own slates. This was done to ensure two independent assessments of each replicate. Grazer marks are sometimes left by scarids (but not by acanthurids), therefore the number of marks is an additional indication of the level of grazing pressure on algae. Grazer marks were recorded as being either absent (n/a),

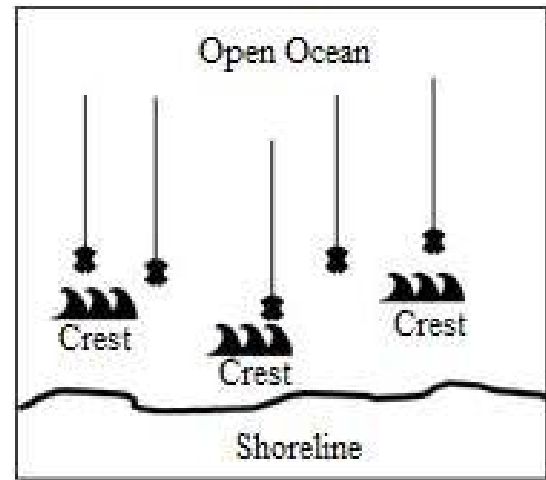


Fig. 1. Transect selection design

a single mark (1), few (2-9) and many ( $\geq 10$ ). These values were then analyzed in pivot tables to assess the frequency of each category of bite in each site. In cases when the reef surface did not allow easy viewing of the quadrat, a picture was taken and later examined by both of the original observers. A final estimate of algal cover and number of grazer marks for each 5-meter point was obtained by taking the average of the independent assessments for each side and subsequently taking the average of the left and right mean value.

### Data Collection - Assessing Groundwater Input into the Reef

Conductivity and salinity were assessed at each reef using a salinity meter. Salinity, the total concentration of all dissolved salts in water, is a strong contributor to conductivity, a measure of water's capability to pass electrical flow. Measurements were taken every 5 meters along the shore of each site, starting 20 meters before the onset of the reef and, from that point, continuing for 100 meters down the coast.

### Data Analysis - Statistical Analyses

Null hypotheses that algal cover and herbivorous fish abundance were independent of the reef being measured were tested using one-way analysis of variance (ANOVAs). Additionally, pairwise comparisons of the three sites were conducted using Bonferroni confidence intervals. To test our null hypothesis that herbivorous fish abundance negatively affects algal cover, we used a simple linear regression model using data combined from all sites. Additional linear regressions were performed to evaluate the individual relationships of acanthurid abundance and scarid abundance versus algal cover both at the reef scale and across all reefs. Additionally, an analysis of covariance (ANCOVA) was used to test the effect of reef (grouping variable) on algal cover (response variable), while controlling for the effect of herbivore abundance (independent continuous co-variable).

Mean conductivity was computed for each site in order to determine which site had the highest groundwater input. Conductivity values were plotted respective to distance from the start of the reef (South end on the shore) in order to locate groundwater input (if any).

## Results and Discussion

Algal cover (ALCO) was found to be significantly different between reefs (ANOVA,  $F_{alco}=4.107$ ,  $P_{alco}=0.0198$ ). Similarly, mean herbivorous fish abundance (HAB) significantly differed between reefs (ANOVA,  $F_{hab}=11.6700$ ,  $P_{hab}=3.2400e^{-05}$ ) (Table 1).

Pairwise comparisons revealed that mean algal cover in Folkestone was not significantly different from Sandy Lane or Mullins Bay at  $\alpha=0.05$ , with Bonferroni confidence intervals of [-2.46, 16.07] and [-13.90, 5.11] respectively. However, Sandy Lane's mean algal cover was significantly less than

| Site        | Mean algal cover (%) | Standard deviation | Mean herbivorous fish abundance | Standard deviation |
|-------------|----------------------|--------------------|---------------------------------|--------------------|
| Folkstone   | 76.15                | 11.67              | 5.92                            | 4.50               |
| Sandy Lane  | 69.08                | 20.57              | 4.23                            | 6.36               |
| Mullins Bay | 80.51                | 12.99              | 12.60                           | 9.50               |

Table 1. Summary for ANOVA

that of Mullins Bay CI[-20.97, -1.89]. Folkstone mean herbivorous fish abundance was found to be significantly less than Mullins Bay, CI[-2.64, 6.02], but not significantly different from Sandy Lane, CI[-2.64, 6.02]. Sandy Lane herbivorous fish abundance was significantly less than Mullins Bay CI[-12.7, -4.04].

Mean percent algal cover (Fig. 2A) was found to be the highest at Mullins Bay (80.51%) and the lowest at Sandy Lane (69.08%). Though total and mean herbivore abundance was highest at Mullins Bay (5.92) and lowest at Sandy Lane (4.23) the most scarids were observed at the Folkstone Marine Reserve (Fig. 2B). Of the 79 scarids observed, 25 were judged to be larger than the acanthurids observed around them. In total, around ten times more acanthurids were observed than scarids.

Simple linear regression models comparing the pooled herbivorous fish abundance and algal cover across all reefs indicated an insignificant relationship at all scales. More specifically, non-significant positive relationships were observed between total herbivore abundance and algal cover at Sandy Lane and at Mullins Bay and a non-significant negative relationship was observed at Folkstone Marine Reserve (Table 2A).

Linear regressions comparing scarid abundance and algal cover were even less conclusive (Table 2B) - P values were all greater than 0.05 and the slopes closer to zero. A non-significant positive relationship was observed between scarid abundance and algal cover for pooled sites and at the Mullins Bay reef specifically. The relationship was also non-significant but negative for Sandy Lane and Folkstone. Comparing acanthurid abundance with algal cover at Sandy Lane and Mullins Bay showed a positive relationship - with a very high P value, as when the two herbivore families were

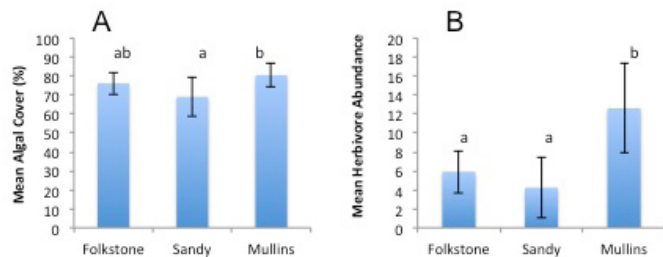


Fig. 2. (A) Mean Algal Cover, (B) Mean Herbivore Abundance; error bars represent standard deviation by sites. If two sites have the same letter above them that means that their means are not significantly different.

| Combined Herbivore Abundance |        |         |        |
|------------------------------|--------|---------|--------|
| All                          | 0.0201 | 0.2894  | 0.1820 |
| Folkstone Marine Reserve     | 0.0835 | -0.1113 | 0.1215 |
| Sandy Lane                   | 0.0085 | 0.0285  | 0.6279 |
| Mullins Bay                  | 0.0086 | 0.0678  | 0.6258 |
| Scarid Abundance             |        |         |        |
| All                          | 0.0014 | 0.0025  | 0.7276 |
| Folkstone Marine Reserve     | 0.0353 | -0.0191 | 0.3204 |
| Sandy Lane                   | 0.0003 | -0.0004 | 0.3212 |
| Mullins Bay                  | 0.0378 | 0.0129  | 0.3032 |
| Acanthurid Abundance         |        |         |        |
| All                          | 0.0195 | -0.0670 | 0.1898 |
| Folkstone Marine Reserve     | 0.0684 | -0.0923 | 0.0317 |
| Sandy Lane                   | 0.0089 | 0.0290  | 0.6478 |
| Mullins Bay                  | 0.0061 | 0.0549  | 0.6811 |

Table 2. Linear Regression Models – Herbivore Abundance vs. Algal Cover

combined. Lower P values, negative slopes and slightly higher R2 values were observed for the linear regressions performed at Folkstone Marine Reserve and pooled sites (Table 2C).

In the first ANCOVA model (with an interaction effect between reef (the grouping variable) and herbivore abundance (the independent continuous co-variate)), herbivore abundance was not found to significantly predict algal cover at the reef scale (ANCOVA with interaction,  $F_{hab} = 1.892$ ,  $P_{hab} = 0.1726$ ). However, algal cover significantly differed between reefs, which in this case could be interpreted as a significant difference in intercepts between the regression lines of Folkstone, Sandy lane and Mullins Bay (ANCOVA,  $F_{reef} = 3.138$ ,  $P_{reef} = 0.0485$ ). Furthermore, no interaction between reef and herbivore abundance was found (ANCOVA,  $F_{hab:reef} = 0.944$ ,  $P_{hab:reef} = 0.3933$ ) (Fig. 3). Therefore, on the small scale the effect of herbivore abundance on algal cover does not depend on the reef. These results suggest that the slope of the regression lines between herbivore abundance and algal cover did not vary across reefs. The results of a second ANCOVA model (without interaction) confirmed that there was no significant difference in the slopes of the regression lines of each reef (ANCOVA without interaction,  $F_{hab} = 1.895$ ,  $F_{reef} = 3.142$ ,  $P_{hab} = 0.1722$ ,  $P_{reef} = 0.0482$ ). A subsequent comparison of both models using a one-way ANOVA showed that the effect of reef and herbivore abundance on algal cover are independent of one another (ANOVA(mod1,mod2),  $F = 0.9436$ ,  $P = 0.3933$ ).

Overall, the analysis shows that algal cover and herbivorous fish abundance significantly differ between the three sites. However, herbivorous fish abundance does not significantly predict algal cover, suggesting that other factors may be responsible for the regulation of algal growth on these reefs.

### Bite Mark Analysis

Bite marks in the coral from scarids were observed at Folkstone, but neither at Sandy Lane nor at Mullins Bay. Out of the observations at Folkstone, 0 bite marks were observed 20 times, a single bite mark was observed 8.5 times, 2-15 bite marks were observed 20 times, and 15+ bite marks were observed 11.5 times.

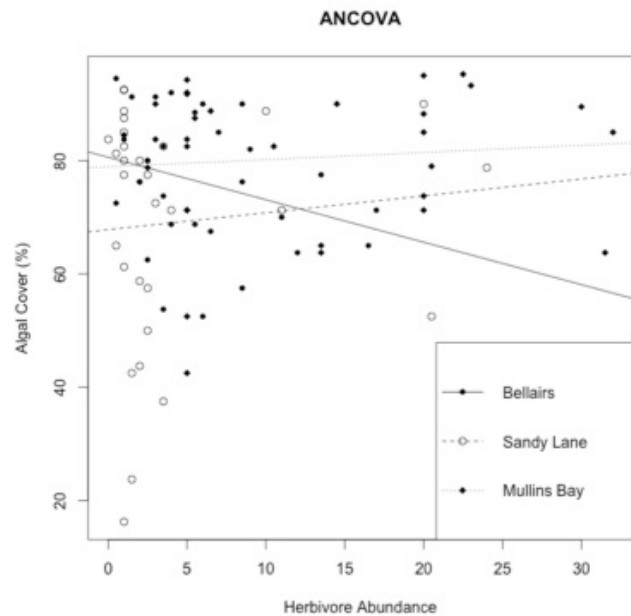


Fig. 3. Results of the ANCOVA – Reef (REEF) was used as the grouping variable and is dimensionless. Herbivore abundance (HAB) was used as the continuous predictor and is in units of individual fish. Algal cover (ALCO) was used as the response variable and was recorded as a percentage.

## Conductive Value Analysis

The highest mean conductivity, 56163  $\mu\text{S}/\text{cm}$ , was found at Sandy Lane, while the lowest was recorded at Folkestone Marine Reserve, which had a conductivity value of 56163  $\mu\text{S}/\text{cm}$ . Mullins Bay had an intermediate conductivity value of 56455  $\mu\text{S}/\text{cm}$ . Important drops in conductivity were observed in front of the Bellairs Research Institute (located near the shore where the Folkestone reef is found), before the reef at Mullins Bay and 20 meters after the start of the reef at Sandy Lane (Fig. 4).

## Discussion

While a negative relationship between scarid and acanthurid abundance and algal cover has been observed and confirmed in previous studies (12, 16) (Table 2), only the relationship between acanthurid abundance and algal cover in the Folkestone Marine Reserve was found to be significant ( $P < 0.05$ ). No inferences can therefore be made from our data concerning whether acanthurids or scarids had a more significant impact on algal cover, as neither were found to have a strong impact. From the linear regression analysis performed, we saw that herbivore abundance does not affect algal cover, irrespective of the reef analyzed.

We interpret dips in conductivity values as marking sources of groundwater input into the reef. In our study, we found groundwater input sources near each of our three reefs, with the most significant being that found in the Folkestone Marine Reserve. Since it is likely that the nutrient levels within the groundwater inputs at all three sites are comparable, it can be said that the Folkestone Marine Reserve receives the highest amount of

nutrient input via groundwater discharge.

It is important to take into account the limitations of our data arising from the limited time of our study and the small sample size. Due to time constraints, we only analyzed a small number of reefs and transects at each reef. The small sample size reduces the power of the statistical tests used, making it harder to make any inference about our data. Furthermore, multiple factors affected the process of data collection. For example, fish counts as well as algal cover measurements, could be affected by differing abilities among researchers to correctly identify fish families and algae. The researchers in our study had limited experience in identifying fish prior to this experiment. While the observers usually made similar fish counts in this study, additional experience in fish identification would likely have decreased the frequency of divergent results between individuals. These factors may have resulted in higher variance across replicates, reducing the significance of our data. Further studies could therefore be done with greater replication in the number of sites and transects, and additional training given to the people collecting data, both of which would act to reduce the limitations of our data.

Despite seeing a direct impact of herbivorous fish on algal cover in the form of grazing marks, we found in our analysis that there is no significant correlation between the abundance of said fish and algal cover. This suggests that herbivorous fish do not have a significant effect on algal growth in the coral reef ecosystems of Western Barbados. However, other factors may be responsible for algal covers that were not addressed in our experiment.

Some other factors that were not assessed but observed and could therefore be influential were: (1) the presence of *Diadema* in certain reefs; (2) biological interactions between fish; and (3) varying structural complexity of our study reefs. Many reefs across the Caribbean have yet to recover their *Diadema* populations. (9) We noticed higher numbers of *Diadema* on the Sandy Lane and Mullins Bay reefs than in Folkestone Marine Reserve reefs. Thus, *Diadema* grazing could be replacing the low grazing of scarids in Sandy Lane and Mullins Bay. In addition, interactions between fish that were not accounted for in our analysis may have had an impact on the data we collected. For example, damselfish (*Pomacentridae*) are territorial, and attack other fishes entering their territories. (10) This behavior may have contributed to lower scarid and acanthurid sightings; however, we did not assess the presence of damselfish across sites in this study. Finally, structural complexity has been documented as positively affecting coral reef fish population density and species richness. (11) The variation in topography across sites could not only have contributed to varying fish abundances, but also affected our range of visibility. Furthermore, differences in topography may also have caused a variation in our estimates of algal cover across the different sites, with a flat reef surface being much easier to visualize than a quadrat placed on a more uneven surface, for example.

We interpreted all of the scarids and acanthurids as being equivalent but there are various reasons why that might not have been a valid assumption, since both groups are of different sizes and display different feeding behaviors. Firstly, roughly one third of the scarids observed were found to be larger than the observed acanthurids. The relationship between scarid size and volume of algae consumed was found to be roughly curvilinear, with larger fish consuming more algae. (12) Intuitively, it makes sense that a similar relationship between fish size and algal biomass consumed exists across all herbivores. It is then reasonable to assume that scarids should not be considered equivalent grazers to acanthurids. Larger scarids have also been shown to make deeper grazing marks and therefore change both the algal cover and the underlying substratum resulting in new colonization sites on the reef. (12) This implies that the larger scarids may play a more significant role in the reduction of algal cover and subsequent resurgence of coral than the acanthurids and smaller scarids. We recommend that further studies investigating the effect of herbivore abundance on algal cover should carefully record scarid size and account for it in the analysis.

While we predicted that herbivore abundance would significantly affect algal cover, other ecological elements, such as eutrophication, may be used to help explain the variation of our results from those hypothesized. Eutrophication has been shown to contribute significantly to high algal cov-

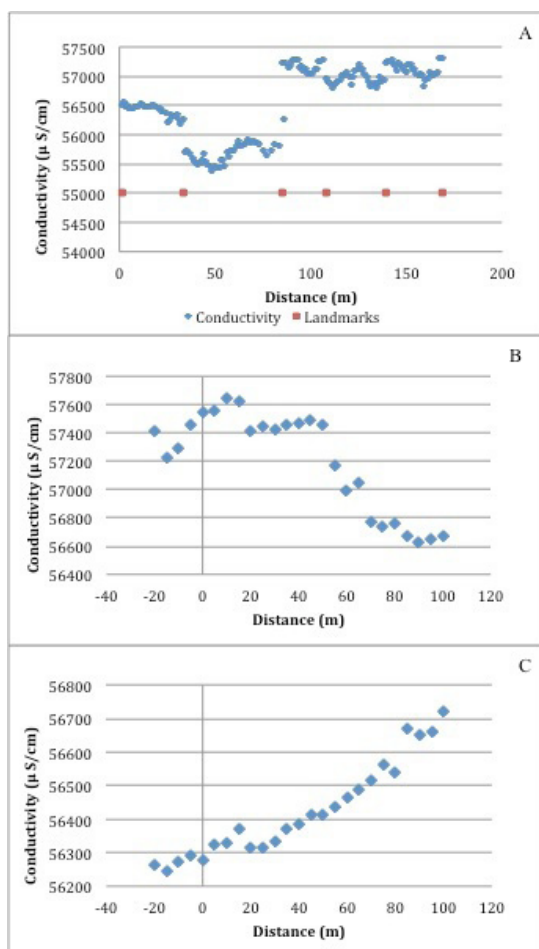


Fig. 4. (A) Folkestone Marine Reserve conductivity measurements. The red boxes indicate position of landmarks relative to the conductivity measurements. (B) Sandy Lane conductivity measurements recorded along the beach. The zero point represents the starting point of the reef, and the negative values before it indicate groundwater measurements taken north of the reef. (C) Mullins Bay conductivity measurements recorded along the beach.

er. (13) Therefore, it is possible that the nutrient input from groundwater seepage is impacting the growth of algae in the coral reefs that we examined, thereby accounting in part for the high algal cover across our three chosen sites and potentially overshadowing the effect of herbivorous grazing on algal growth. While we did not directly measure nutrient concentrations, our conductivity data indicated the presence of a large amount of groundwater input, which may have affected levels of algal cover. This relationship is consistent with previous research on the bottom-up effect of eutrophication on algal growth in coral reef ecosystems. Studies have determined that nutrient input has a strong effect on algal cover, both in Barbados as well as worldwide. (14) However, it is important to note that groundwater input is directly related to tidal level, as can be seen in our study of Folkestone Marine Reserve conductivity. (15) Consequently, our results could have been influenced by the variance in sampling time in relation to the closest high tide across sites. We attempted to account for this since we observed a clear difference, but in order to avoid possibly over or under-compensating for this factor, salinity and conductivity values should be taken at the same time at all sites.

## Conclusion

While our data does not indicate a strong relationship between algal cover and herbivorous fish abundance, many previous studies do demonstrate that a negative relationship exists between the two. It is therefore important to conduct a similar study with greater replication both within and across sites in order to foster a greater understanding of the relationship between herbivory and algal cover in Western Barbados. This additional knowledge of the importance of the role of herbivorous fish in Barbados could be used to support more ecological fishing regulations (i.e. restrictions on fishing of large scarids). However, in the scientific community, there remains a debate over whether the top-down effects of herbivory on algal growth are significant in comparison to the bottom-up effects of eutrophication. (14) Thus, further studies should be performed to quantify the amount of groundwater seepage, its nutrient composition, and its effect on algal growth. The results of this research would then demonstrate the importance of limiting groundwater discharge and pollution in Barbados. Coral reef ecosystems worldwide are expected to face further threats from such coastal development and climate change over the next few decades. It is thus crucial for conservation efforts that we understand these mechanisms behind algal regulation to prevent coral loss and algal dominance in the future.

## Acknowledgements

We would like to thank the professors Frederique Guichard, Neil Price, and Thomas E. Bureau of the Department of Biology of McGill University for their continuous guidance and support in conducting this study. We also highly appreciate the comments from the anonymous reviewers at MSURJ for their constructive feedback.

Additionally, we wish to thank the McGill Bellairs Research Institute, located in St. James, Barbados for providing us with accommodations and allowing us to utilize their facilities and equipment to conduct this research. We extend special thanks to its staff for making our stay comfortable and enjoyable.

## References

- Riegl B, Bruckner A, Coles SL, Renaud P, Dodge RE. Coral reefs: threats and conservation in an era of global change. *Annals of the New York Academy of Sciences* 2009; 1162(1):136-86.
- Bruno JF, Precht WF, Vroom PS, Aronson RB. Coral reef baselines: how much macroalgae is natural? *Marine Pollution Bulletin* 2014; 80:24-29.
- Hunte W, Côté I, Tomascik T. On the dynamics of the mass mortality of *Diadema antillarum* in Barbados. *Coral Reefs* 1986; 4(3):135-39.
- Mumby PJ. The impact of exploiting grazers (Scaridae) on the dynamics of caribbean coral reefs. *Ecological Applications* 2006; 16(2):747-69.
- Cheal AJ, Emslie M, MacNeil MA, Miller I, Sweatman H. Spatial variation in the functional characteristics of herbivorous fish communities and the resilience of coral reefs. *Ecological Applications* 2013; 23(1):174-88.
- Valle, H. Lecture presented at Bellairs Research Institute. May 2014.
- Protected Marine Areas [internet]. [Place unknown]: Coastal Zone Management Unit of Barbados; 2014. Available from: <http://www.coastal.gov.bb/pag-eselect.cfm?page=17>
- Williams ID, Polunin NVC. Large-scale associations between macroalgal cover and grazer biomass on mid-depth reefs in the caribbean. *Coral reefs: journal of the International Society for Reef Studies* 2000; 19(4):358.
- Myhre S, Acevedo-Gutiérrez A. Recovery of sea urchin *Diadema Antillarum* populations is correlated to increased coral and reduced macroalgal cover. *Marine Ecology Progress Series* 2007; 329:205-10.
- Booth DJ. In: Greenwood JG and Hall NJ, editors. Grazing pressure of roving and territorial fishes on patch reef in one tree lagoon. *Proceedings of the Australian Coral Reef Society 75th Anniversary Conference*; 1998 Oct 15-27 ; Brisbane, Australia; Australia School of Marine Science, University of Queensland; 1998. p. 29-42.
- Ménard A, Turgeon K, Roche DG, Binning SA, Kramer DL. Shelters and their use by fishes on fringing coral reefs. *PLoS ONE* 2012; 7(6): e38450. DOI: 10.1371/journal.pone.0038450.
- Bonaldo RM, Bellwood DR. Size-dependent variation in the functional role of the parrotfish *Scarus rivulatus* on the Great Barrier Reef, Australia. *Marine Ecology Progress Series* 2008; 360:237-244.
- Costa Jr OS, Leao ZMAN, Nimmo M, Attrill MJ. Nutrifcation impacts on coral reefs from northern Bahia, Brazil. *Hydrobiologia* 2000; 440: 307-315.
- Lapointe BE. Nutrient thresholds for bottom-up control of macroalgal blooms on coral reefs in Jamaica and southeast Florida. *Limnology and Oceanography* 1997; 42(5): 1119-131.
- Xun Z, Chuanxia R, Yanyan Y, Bin F, Yecheng O. Tidal effects of groundwater levels in the coastal aquifers near Beihai, China. *Environmental Geology* 2006; 51(4): 517-25.
- Lewis SM, and Wainwright PC. Herbivore abundance and grazing intensity on a caribbean coral reef. *Journal of Experimental Marine Biology and Ecology* 1985; 87(3):215-28.

Research Article

<sup>1</sup>Department of Physiology,  
McGill University, Montreal,  
QC, Canada

Keywords

Sensory adaptation, ambiguity,  
envelope, power law adaptation,  
LS: Lateral segment of the electro-  
sensory lateral line lobe (ELL), CLS:  
Centro-lateral segment of the ELL,  
CMS: Centro-medial segment of  
the ELL

Email Correspondence

zhubo.zhang@mail.mcgill.ca

Zhubo Zhang<sup>1</sup>, Maurice J. Chacron

# Scale-Invariant Adaptation in Response to Second-Order Electro-Sensory Stimuli in Weakly Electric Fish

## Abstract

**Background:** Natural stimuli can range orders of magnitude, and their encoding by the brain remains a central issue in neuroscience. An efficient way of encoding a natural stimulus is by changing a neuron's coding rule in tandem with changes in the stimulus. This phenomenon is called sensory adaptation. However, sensory adaptation creates ambiguity in the neural code, as different stimuli can produce the same neural response.

**Methods:** One way to resolve this ambiguity is to encode additional stimulus information through parallel channels. We performed in vivo extracellular recordings from pyramidal cells in two parallel maps, the lateral segment (LS) and the centro-medial segment (CMS), within the hindbrain of the weakly electric fish *Apteronotus leptorhynchus*, in response to stimuli that resemble the presence of another conspecific.

**Results:** We found that CMS pyramidal cells generally adapted less strongly than LS cells ( $p < 0.05$ ). Signal detection theory confirms that the lesser degree of adaptation leads to a stronger ability to disambiguate between two input stimuli ( $p < 0.05$ ). In addition, the time course of adaptation in LS strictly followed a power law while that of CMS followed a power law only for a certain set of stimuli.

**Limitations:** The design of our study allowed for a stimulus that oscillated only between two distributions. Further studies into the hindbrain's ability to disambiguate the adaptive code will require confusion analysis of a stimulus that changes between more distributions. For confusion studies, cells in different areas can be compared as long as they have receptive fields in similar areas.

**Conclusions:** Through recording from two parallel segments of the electro-sensory system in the hindbrain, we observed that different segments adapted with different strengths to similar stimuli. Different amounts of adaptation allude to a balance between the need to preserve absolute stimulus information while simultaneously encoding a stimulus efficiently through adaptation.

## Introduction

Our senses enable us to experience our surroundings through a multitude of sensations, which are then encoded by the nervous system. One of the most basic ways in which neurons encode information is in their firing rate (1), but a sensory stimulus often contains characteristics that vary over more orders of magnitude than the firing rate can encode. (2) For example, the light intensity outside on a clear winter day is much greater than it is indoors, and our eyes need some time to adjust when moving from one to the other. This adjustment highlights an efficient mechanism for the encoding of light intensity—adaptation. A neuron adapts to a certain stimulus by changing its coding strategy to match the current distribution of the stimulus. (2) In the human visual system, adaptation is more complex than the adaptation of individual neurons, but this process allows individual neurons to encode light intensities over a wide range of magnitudes. Nevertheless, a problem arises with adaptability – ambiguity. Given a certain firing rate, the absolute value of the stimulus it encodes cannot be determined without additional contextual information.

There is much discussion on how the nervous system resolves this problem of ambiguity. In experiments on the fly visual system, Fairhall and colleagues (3) demonstrate that ambiguity can be fully resolved at the level of the individual cell. Other researchers such as Hildebrandt and colleagues (4) describe a circuit-level approach, where the neural circuitry establishes context at the beginning of a stimulus, encoding the remainder of the stimulus relative to it.

Our group has previously suggested a neural computation called parallel

coding, where distinct populations of cells encode different features of a stimulus. (5) We believe that parallel coding is another mechanism which can resolve ambiguity—while one population of neurons may adapt to a stimulus, another may not, thus preserving the context of a stimulus. Our model organism is the weakly electric fish *Apteronotus leptorhynchus*. These fish emit an electric organ discharge (EOD) that can interfere with the EODs of their peers, creating amplitude modulations (AMs). (6) These AMs can indicate the presence of their peers, and are sensed by peripheral electroreceptors located on the surface of the fish. Afferent fibres from the peripheral electroreceptors trifurcate onto three parallel topographical maps in the hindbrain electrosensory lateral line lobe (ELL): the centro-medial (CMS), centro-lateral (CLS), and lateral (LS) segments. (7)

Previous studies have shown that pyramidal cells in these three segments process first- and second-order properties of AMs, such as mean and variance, respectively, relaying them to higher order areas. (5,7) Although adaptation to first-order properties of electrosensory stimuli has been described (5), adaptation to second-order properties has not been characterized. Second-order properties of AMs are defined as the depth of modulation of interference signals, and relate to the distance between the fish and its peer. We will refer to the depth of modulation of an EOD signal as its envelope.

In this paper we compare the responses of LS and CMS cells to step changes in the envelope of the AMs. We chose these areas because of their contrasting frequency tuning properties, acknowledging that the frequency response of CLS cells is intermediate of the two. (7) The frequency tuning of LS and CMS is due in part to the differential expression of small conduc-

tance  $\text{Ca}^{2+}$  activated  $\text{K}^+$  (SK) channels in pyramidal cells (6), where high expression of these channels in LS cells corresponds with its high-pass tuning, and low expression in CMS cells corresponds with its low-pass tuning. Since the spike-triggered SK current is hyperpolarizing, we hypothesized that the amount of adaptation of LS and CMS cells to the AM envelope would also follow the frequency tuning of these areas, where pyramidal cells in LS should adapt more than CMS pyramidal cells. Through peri-stimulus time histogram and signal detection analyses, we found that our results were consistent with this hypothesis. We also characterized the time courses of adaptation between these two areas and found that they could be modelled by a power-law decay for all frequencies in LS, and for frequencies up to 1 Hz in CMS.

## Materials & Methods

### Surgery & Recording Procedures

All procedures were approved by the McGill University Animal Care Committee. We paralysed the fish with an intramuscular injection of Tubocurarine chloride pentahydrate (Sigma,  $1 \mu\text{g/g}$  body weight), and respiration of the fish at a flow rate of 10 mL/min. The fish was kept partially submerged in water, with the top of its head exposed. We then locally anesthetized the site of surgery with 2% lidocaine, removed 6 mm<sup>2</sup> of the skin above the skull, and glued the skull to a metal post to stabilize it. To access the ELL, we first located a major vein known as T0. We then drilled a 2 mm<sup>2</sup> hole through the skull, above the eminentia granularis posterior that lies caudal to T0. (10)

We performed differential extracellular recordings from pyramidal cells in areas LS and CMS with Woods metal electrodes. (11) For area LS, we placed electrodes laterally, halfway from the junction between the cerebellum and eminentia granularis posterior, and rostrally, a third of the way from T0 to the back of the brain, no more than 900  $\mu\text{m}$  from the brain surface. For area CMS, we placed electrodes medially and caudally, halfway from T0 to the back of the brain. These recordings were done at a depth of at least 1200  $\mu\text{m}$ . We identified pyramidal cells based on their responses to a 4 Hz sinusoidal search stimulus—well-isolated cells responded preferentially to a single phase of the stimulus. (7) The signal recorded from the electrodes was amplified (Model 1000 amplifier, A-M systems) and digitized at 16 bits and 10 kHz using a CED Power1401 and Spike2 software. (7)

### Stimulus

We stimulated with a sinusoidal electric signal that superimposes with, and creates amplitude modulations (AMs), of the animal's EOD. To phase-lock our output signal with the animal's EOD, we first recorded the EOD with chloridized silver electrodes placed at the head and tail. The zero crossings of the amplified EOD (DAM50, World Precision Instruments) triggered a function generator to create a sine wave at a frequency 40-50 Hz higher than the EOD frequency (Agilent 33220A). The sine waves were multiplied by a waveform, described below as our "stimulus" (MT3 multiplier, Tucker Davis Technologies). The output was then attenuated (LAT45 attenuator, Leader Electronics), and sent to the tank by a stimulus isolator (A395 linear stimulus isolator, World Precision Instruments). These sine waves changed the amplitude of the EOD depending on the polarity of the waveform. The signal was delivered via two electrodes placed 20 cm from the sides of the fish. A dipole was placed approximately 2 mm from the surface of the fish to record the signal sensed by the fish, in order to adjust the attenuation so that the high-low contrast of the AMs was about 10-15%.

Although our stimuli were the EOD-triggered sine waves described above, we will refer to the "stimulus" as the amplitude modulations of the EOD resulting from the sine waves. We used three types of stimuli in our experiments (see below): a 4 Hz AM, randomly modulated 5-15 Hz AMs, and randomly modulated 60-80 Hz AMs. We used the 4 Hz stimulus to test whether our cell in question responded to the stimulus, as described above. The randomly modulated stimuli were designed based on the frequency responses of the segments of the ELL. Areas LS and CLS preferred higher AM frequencies between 40 and 80 Hz, while CMS responded maximally to frequencies below 40 Hz. (8)

All of the stimuli were generated through MATLAB (Mathworks). The 5-15 Hz and 60-80 Hz stimuli were composed of band-pass filtered (fourth-order Butterworth), normally distributed white noise. For these, we modulated the envelope, a second-order property of the AMs, by multiplying the signal with a square wave function that switched between high and low amplitude with frequencies that spanned over three orders of magnitude: 0.05, 0.1, 0.25, 0.5, 1, 2, and 4 Hz for the 5-15 Hz and 60-80 Hz stimuli, and an additional 8 and 16 Hz for the 60-80 Hz stimulus. Each stimulus contained 15-180 cycles of the switch where, between cycles, amplitude modulations came from the same distribution but were uncorrelated. For analysis, we pooled data from both the 5-15 Hz and 60-80 Hz stimuli since the results were identical between the frequency ranges.

### Spike Time Extraction

Data analysis was also performed in MATLAB. We first filtered the digital extracellular recording with a high-pass eighth-order Butterworth filter with a cut-off frequency of 0.02 Hz in order to remove low-frequency noise and isolate our spikes for extraction. We selected a time range that corresponded to a single stimulus trial and applied an appropriate threshold above the noise to capture the spike times. We then applied a spike selection algorithm for further isolation from noise. For each time the spike crossed the threshold, we took a window of 0.8 ms centered at the time of crossing and plotted the maximum against the minimum of the signal in the window. From the plot, a neuron's action potentials were seen as a cluster distinctly separate from the noise, and could be selected and isolated. We stored the spike times as a binary sequence with each element corresponding to a bin of width equal to the sampling period of the digitized signal, containing 1 if there was a spike, and 0 if there was none.

### Peri-Stimulus Time Histograms

We constructed peri-stimulus time histograms (PSTHs) by averaging each cycle of the switch from low to high variance, for each switch frequency. First, we divided the cycle period into a predetermined number of bins between 40 and 60. For each bin, we summed the number of spikes in time, within a single repeat and also across all repeats, divided by the number of repeats as well as the binwidth. The result was an averaged firing rate over time, centered on the middle of each bin. We spaced the binwidths logarithmically with time, to capture the fast changes in firing rate at the beginning of the switch in variance, and linearly with time for the creation of figures. The results were identical in both binning methods. To prepare the PSTH for fitting, we separated the PSTH into two halves, the first being the neuron's response during low variance, and the second being its response to high variance. Since the stimulus switched between high and low variances periodically, the rapid increase in firing rate followed by a decay due to adaptation when the stimulus switched to high variance was captured entirely within the PSTH corresponding to high variance, and the rapid drop in firing rate followed by an increase when the stimulus switched to low variance was captured within the PSTH corresponding to low variance.

### Adaptation Strength

We quantified a cell's adaptation strength by its change in mean firing rate during high envelope for the 0.1 Hz step. We pooled data for both 5-15 Hz and 60-80 Hz carrier frequencies as there was no significant difference between them. To compute the firing rates, we took the difference between the peak firing rate during the first quarter of high envelope, and the firing rate just before the step down to low envelope.

### Adaptation Time Course Estimation

We isolated the decay in firing rate during high envelope by discarding the first few bins of the PSTH, if any, that preceded the bin containing the maximum firing rate. If the maximum was attained on more than one bin, we discarded the data up to the last maximum. We then re-centered the PSTH in time so that the first bin corresponded to the bin with the highest firing rate. We fitted the time course of decay in firing rate at high envelope with both exponential (Eq. 3) and power law (Eq. 4) models. Before doing so, we first obtained two estimates of the steady-state firing rate at high

stimulus envelope by fitting the decay with the following models using MATLAB's nlinfit function, using evenly spaced bins in the PSTH:

$$r_{\text{exp}}(t) = Ae^{-t/\tau} + C, \quad [1]$$

$$r_{\text{pow}}(t) = Bt^{-\alpha} + D, \quad [2]$$

where  $r_{\text{exp}}(t)$  and  $r_{\text{pow}}(t)$  are the respective firing rates for the exponential and power law fits,  $A$  is a normalizing constant for the exponential model,  $t$  is time,  $\tau$  is the exponential time constant in seconds,  $B$  is a normalizing constant for the power law model,  $\alpha$  is the power law constant, and  $C$  and  $D$  are the respective estimated steady-state firing rates for the exponential and power law models.

After obtaining estimates of the steady-state firing rate, we created duplicate PSTHs with logarithmically spaced bins, and subtracted the steady-state estimates obtained from both the above models separately. We then normalized each PSTH with respect to the maximum firing rate, and again fitted the normalized data with the following corresponding models:

$$r_{\text{exp}}(t) = Ae^{-t/\tau}, \quad [3]$$

$$r_{\text{pow}}(t) = Bt^{-\alpha}, \quad [4]$$

where  $r_{\text{exp}}(t)$  and  $r_{\text{pow}}(t)$  are now the normalized respective firing rates for the exponential and power law fits,  $A$  is the new normalizing constant for the exponential model,  $\tau$  is the normalized time constant in seconds,  $B$  is the new power law normalizing constant, and  $\alpha$  is the normalized power law constant.

### Receiver-Operator Characteristic Curves

We quantified the ability of a neuron to distinguish between high and low variance through receiver-operating characteristic (ROC) analysis of a neuron's firing rate. We computed the probability distributions of firing rate for a single cell over the course of a 0.1 Hz switch by separating the time course into 500 ms bins, computing the firing rate during each bin over each repetition, and creating a histogram of those rates. To compute the ability to discriminate an input envelope, we set the distribution of firing rates just before the step up to high envelope as the "false" detection and the distribution at another point in time as the "correct" detection. Using a moving threshold, we computed the probability of correct detection and of false alarm as the area under their respective distributions above the threshold during high envelope, and below the threshold during low envelope. We created ROC curves from these probabilities and quantified discriminability as the area under this curve, where a value of 1 means the cell can discriminate perfectly and 0.5 means that the cell cannot discriminate at all.

To compute the average discriminability of LS cells and CMS cells, we normalized the firing rate probability distributions for each cell with respect to the reference distribution taken from just before the onset of high variance, setting the mean of that distribution to zero and scaling all other values by the standard deviation of the reference. This normalization allowed us to compare firing rate histograms between cells. We computed the ROC curve of each cell separately from these distributions. To compute the average ROC curve, we first rotated all points of the curve clockwise by  $\pi/4$  radians. We binned the interval  $[0, \sqrt{2}]$  into 7 bins, set the "centre" of each bin as the average abscissa value of the points contained in the bin, the mean of the ROC curve as the mean of the ordinate values in that bin, and the 95% confidence intervals of the ROC curve as the 95% confidence intervals of those same ordinate values. These points were then rotated counter-clockwise  $\pi/4$  radians back to the ROC-style orientation.

## Results

We obtained extracellular recordings from 45 pyramidal cells in LS and 32 cells in CMS of the ELL of *A. leptorhynchus* while we played electrosensory stimuli that mimicked interference signals, or AMs, that are present in the presence of another peer (Fig. 1A, blue and green). We periodically

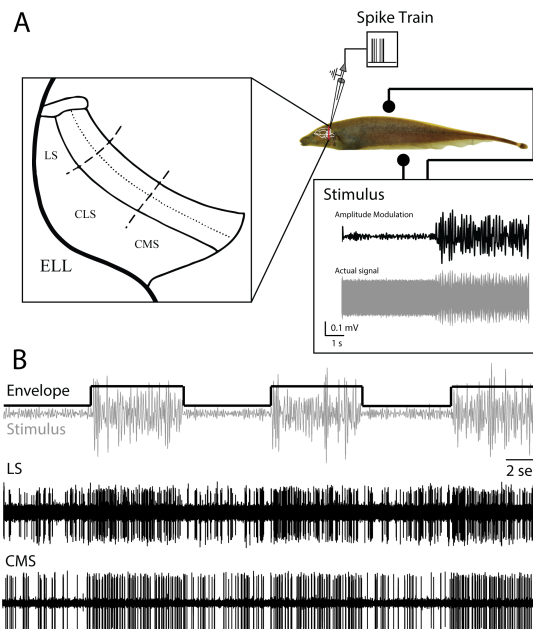


Fig. 1. (A) Schematic of experiment. Electrodes to the side of the fish send sinusoidal stimuli, superimposing with the fish's electric field (bottom right, grey) to create amplitude modulations (bottom right, black). The envelope of the stimulus's amplitude modulations change periodically with time. Extracellular recordings were taken from two areas of the hindbrain known to respond to these modulations, LS and CMS (left). (B) Sample responses of LS and CMS neurons to a stimulus whose envelope (top) steps from low to high with a period of 10 seconds.

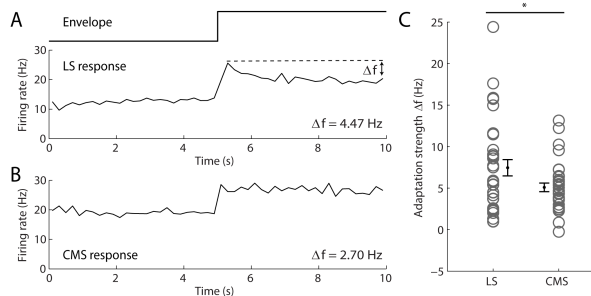


Fig. 2. (A) Averaged PSTH from an LS neuron in response to the stimulus described in Figure 1B. The binwidth used is 500 milliseconds. We define the adaptation strength for each neuron as the difference between the firing rates at the beginning and end of high envelope. (B) Sample response from a CMS neuron (binwidth 500 ms). (C) Changes in firing rates from sample populations in CMS ( $n=32$ ) are significantly lower than those from LS ( $n=32$ ,  $p=0.0377$ , one-way ANOVA). Black indicates the means and standard error of the means.

switched the depth of modulation, or envelope, of these AMs to simulate different distances between our fish and the mimicked conspecific. Since electromagnetic effects are stronger at closer distances, two fish in close proximity would create AMs with high envelope, and two fish further away lead to AMs with lower envelope. Fig. 1B shows sample responses from LS and CMS cells in response to three repeats for a switching frequency of 0.1 Hz.

Since pyramidal cells in the ELL preferentially respond to specific phases of AMs (8), by averaging over multiple repeats of a high-low modulation cycle we can obtain an averaged PSTH of a cell in response to envelope even when the underlying AMs are uncorrelated. The phase preference of

ELL cells can be grouped into two categories: I-cells that prefer the falling phase of a cycle and E-cells that prefer the rising phase. Since we found no significant difference between the responses of the two types of cells ( $p > 0.15$  for cells in either segment, in terms of adaptation strength and area under ROC curve), we grouped them together in the presentation of these results. Figs. 2A and 2B show two sample responses from neurons in LS and CMS, respectively. In response to an increase in envelope, both neurons increase their firing rates. However, the LS neuron depicted in Fig. 2A decreases its firing rate over the course of high envelope, suggesting that that neuron adapts. The CMS neuron in Fig. 2B does not noticeably adapt in the same manner. We computed the change in firing rate from the peak to the last bin of the PSTH at high envelope to create a measure of adaptation. Fig. 2C shows aggregate adaptation strengths obtained in this manner. Overall, CMS cells on average maintained their firing rate during high envelope more so than LS cells ( $p < 0.05$ , one-way ANOVA). However, we note that there is a large degree of heterogeneity in adaptation responses, with a smaller number of LS cells and a larger number of CMS cells that do not adapt a considerable amount.

In terms of adaptation, previous experimenters (3, 9-11) have reported that the time course of adaptation resembles a power-law relation rather than an exponential relation with time. We hypothesized that a power-law relation could also describe the time course of ELL pyramidal cell firing rate adaptation in response to changes in envelope. One of the hallmarks of power-law spike frequency adaptation is that the decay is self-similar over different timescales (12), whereas the exponential model of adaptation has a single characteristic timescale and is not

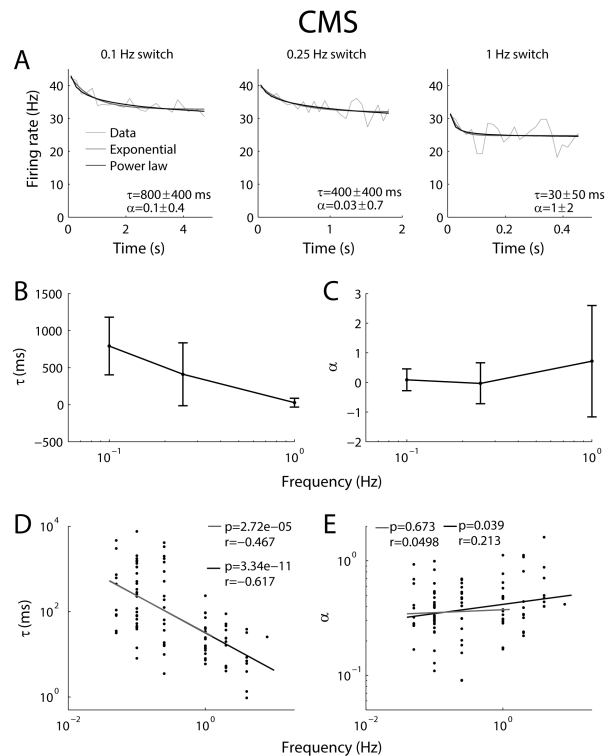


Fig. 4. (A-C) Same format as Figure 3 for CMS. CMS neurons respond weaker than LS neurons to envelope, and adapt less, hence the large error bars that overlap across zero in panels B and C. (D) Time constants for CMS sample population ( $n=32$ ) with regression fits for frequencies from 0.05 Hz to 1 Hz (grey) and 0.05 Hz to 8 Hz (black). For both frequency ranges, the slopes are significant ( $p < 10^{-4}$ ). (E) Power law constants with linear fits for frequencies up to 1 Hz (grey) and up to 8 Hz (black). The slope for the fit incorporating frequencies from 0.05 Hz to 1 Hz is not significant ( $p > 0.5$ ).

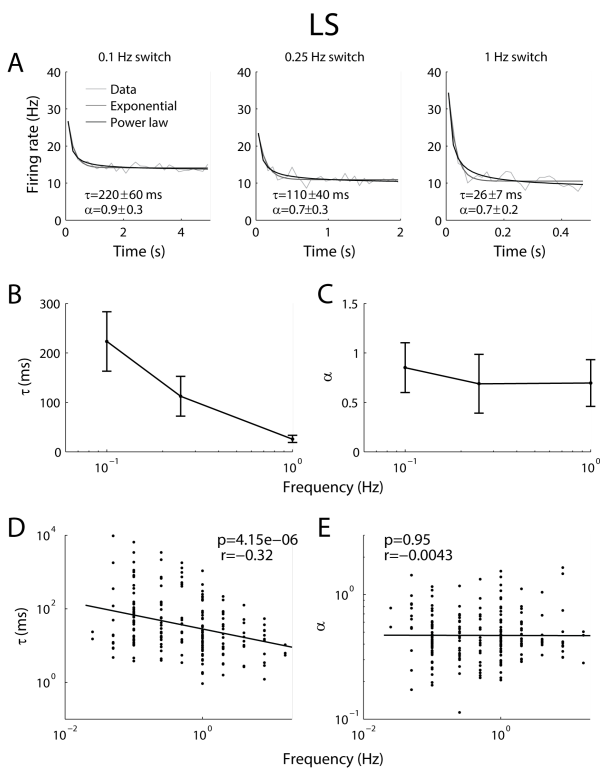


Fig. 3. Exponential and power law fits for LS. (A) Comparison of the decay in firing rate a sample LS cell for three different frequencies of the switch from low to high envelope. We fitted each response with exponential (dark grey) and power-law (black) functions. (B) Exponential time constants for the fits in A, with error bars as 95% confidence intervals. (C) Power-law exponents for the fits in A, with 95% confidence intervals. (D) Time constants of the LS sample population ( $n=45$ ) as a function of frequency. The axes are logarithmic scale. The solid line is a linear regression fit of the data, the slope of which is significantly different from zero ( $p < 10^{-5}$ ). (E) Power law coefficients of the LS sample population, with a line indicating a linear regression fit. The slope here is not different from zero ( $p > 0.9$ ).

self-similar over different timescales. We fitted both exponential and power-law models to the decay in the PSTH in response to changes in envelope over frequencies spanning from 0.05 Hz to 16 Hz. In LS, we found that both models fit very well over a wide range of frequencies (Fig. 3A). However, the time constants of our exponential fits ( $\tau$  in  $e^{-t/\tau}$ ) were dependent on frequency of switch presented, whereas the power law constants ( $\alpha$  in  $t^{-\alpha}$ ) were independent. This held for both single cells (Fig. 3A-C) and the LS sample population (Fig. 3D and 3E), there was a correlation between frequency and time constant of adaptation ( $r = -0.317$ ,  $p < 10^{-5}$ ) whereas no correlation was found between frequency and power law constant ( $r = -0.004$ ,  $p > 0.95$ ).

Compared with the LS pyramidal cells, the CMS pyramidal cells adapt less to changes in envelope. Therefore, the exponential and power law fits have much more error (Fig. 4A-C). However, the exponential time constant of decay still depends on the frequency of envelope steps both at the individual cell level (Fig. 4B) and across the CMS sample population (Fig. 4D). Estimates for the power law constant of decay is independent of envelope step frequencies up to 1 Hz ( $r = 0.0498$ ,  $p > 0.5$ ). However, there is a slight positive correlation when considering envelope frequencies above 1 Hz (Fig. 4E,  $r = 0.213$ ,  $p < 0.05$ ).

Due to the long duration of some of our stimuli, we considered habituation affecting adaptation during and between trials. However, comparisons of the first 30 to the last 30 repeats of the 0.1 Hz stimulus, our longest stimulus at thirty minutes, revealed no significant differences in the time course response. Additionally, the order of stimuli presented were shuffled randomly for each cell that we recorded from a single fish.

To quantify changes in ambiguity as a result of adaptation, we constructed

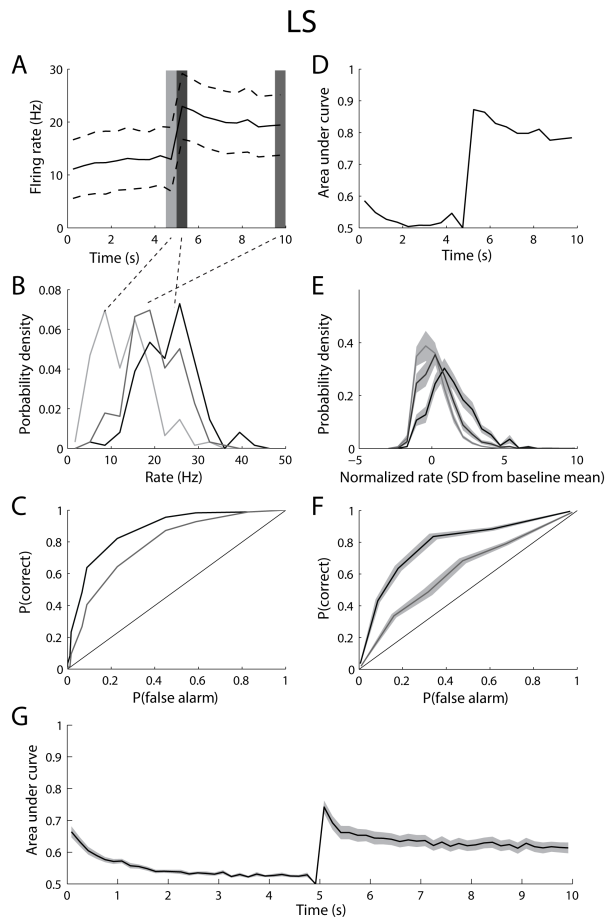


Fig. 5. (A) PSTH for the neuron in Figure 2A displaying the variability of firing rates over each repetition. Dashed lines indicate one standard deviation from the mean. (B) Distribution of firing rates for three sections of the PSTH highlighted in A. (C) ROC curves for the distributions at the beginning (black) and end (grey) of high envelope in comparison to end of low envelope. (D) Areas under the ROC curve across the PSTH in comparison to the end of low envelope. (E) Averaged distributions for the bins highlighted in A across LS sample population ( $n=32$ ). (F) Averaged ROC curves corresponding to those in C. (G) Averaged area under the ROC curve throughout the entire high-low envelope cycle for LS population. The grey shading in E-G indicate the standard errors of the means.

ROC curves based on the trial-by-trial firing rates of each cell and computed the area under the curves during the course of the 0.1 Hz low-high step in envelope. We took a reference distribution from the distribution of firing rates just before the step up to high envelope, and compared that distribution with the firing rate distributions just after the step up to high envelope and again five seconds later (Figs. 5A,B and 6A,B). We calculated the amount of ambiguity of a cell as the area under the ROC curve at those times (Figs. 5C,D and 6C,D). In both LS and CMS cells, the area under the ROC curve is highest at the onset of high envelope, and decreases as a result of adaptation (Figs. 5E-G, 6E-G). While the steady-state ambiguity at 5 seconds is not significantly different between LS and CMS ( $p>0.8$ ), the drop in the area under the curve across 5 seconds is significantly greater in LS than CMS (Fig. 6G, inset).

## Discussion

We investigated the responses of neurons in two segments of the electro-sensory hindbrain to changes in second-order properties of naturalistic stimuli and found that generally, these neurons adapted to second-order properties, and the degree of adaptation varied between different areas of the hindbrain. Additionally, our results suggest that the time course of adaptation does not follow a single-timescale exponential decay in the seg-

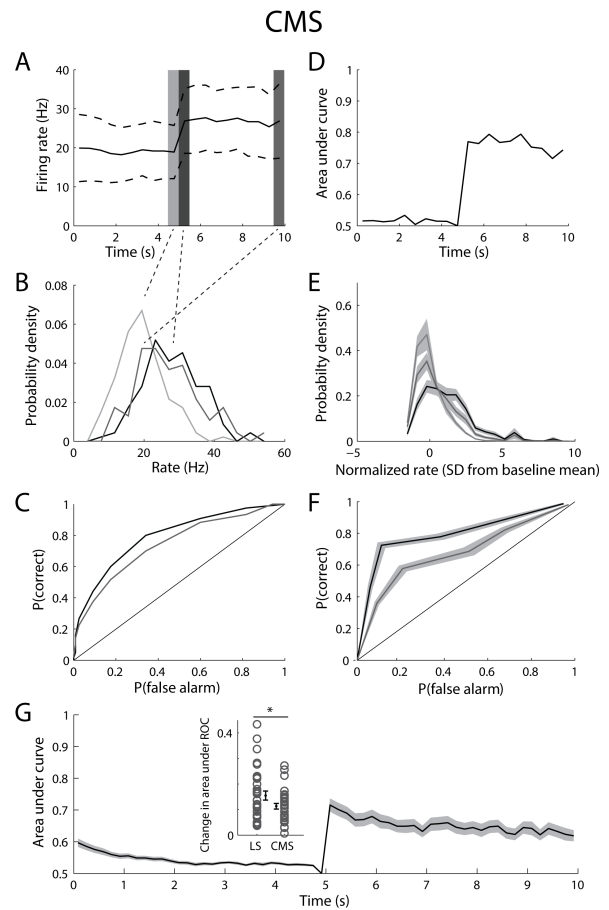


Fig. 6. (A-G) Same format as Figure 5 for CMS population ( $n=32$ ). (G, inset) Change in area under ROC for LS is significantly greater than that of CMS ( $p<0.05$ , one-way ANOVA).

ments sampled. Instead, the two segments adapted differently: one whose time course follows a power law, and another that only resembles a power law for lower frequencies.

The differential expression of SK channels between the segments of the ELL can in part explain the differences in adaptation between the segments. A combination of adapting and non-adapting cells could be a solution to the issue of ambiguity—while non-adapting cells encode the context of a stimulus, adapting cells could code for information relative to that context. Higher expression of SK channels in area LS could also contribute to power law adaptation to changes in envelope. Since increases in  $Ca^{2+}$  are associated with increases in synaptic activity, frequent high envelopes during fast high-low cycle lengths increase the build-up of  $Ca^{2+}$ , SK channel activation, and, consequently, adaptation. At longer cycle lengths, the long duration of low envelopes decreases pyramidal cell firing, decreasing the build-up of  $Ca^{2+}$  and leading to slower adaptive processes during high envelope. This scaling of the adaptation time course with the cycle length of the switch could lead to the scale-invariant characteristic of a power-law decay.

One of the advantages of power law adaptation is that it has the potential to whiten the frequency content of a stimulus. (11) A major theme of neural coding is the decorrelation of input signals between cells, eliminating redundant coding of information and increasing the efficiency of a neural network. (13) Given an input with a non-white frequency content, power law adaptation has the potential to tune an individual neural response to equally represent all input frequencies of the stimulus, maximizing information transfer. (2)

Although the time constants of adaptation in areas CMS and LS vary with the frequency of changes in envelope, the power law constants vary in CMS neurons as well, at least over the range of envelope frequencies

presented. This dependence of the power law constant with frequency in CMS neurons is not present for frequencies up to 1 Hz, suggesting two different mechanisms for envelope processing in the CMS. The low-pass frequency tuning of CMS to envelopes, as suggested by its low amount of adaptation, could render high envelope frequencies (>1 Hz) irrelevant, since these higher envelope frequencies begin to overlap with possible AMs from other fish. We reason that CMS neurons preferentially respond to envelopes of low frequencies indicative of the presence and movement of another fish. In comparison, the frequency tuning of LS to first-order AMs is high-pass (8), allowing more second-order envelope frequencies to be represented in that area.

In our framework of parallel coding, the slowly-adapting CMS cells could serve as a channel to keep track of absolute stimulus features, while the faster-adapting LS cells could allow for encoding of relative stimulus features. One limitation of this model was that there was still a heterogeneity in adaptation in the CMS, where some cells adapted more than others. However, some CMS and even LS cells did not adapt at all, and it could be that these non-adapting cells are the true channels for absolute stimulus information. Further studies investigating adaptation among the different populations of LS and CMS pyramidal cells may reveal the different channels available to disambiguate information provided by spike frequency adaptation.

## Acknowledgements

We would like to thank Gary Huang for help with the experiments, and the Natural Sciences and Engineering Research Council of Canada as well as the Fond du Québec: Nature et Technologies, for funding for this project.

## References

1. Panzeri S, Brunel N, Logothetis NK, Kayser C. Sensory neural codes using multiplexed temporal scales. *Trends Neurosci.* 2010;33(3):111-20.
2. Wark B, Lundstrom BN, Fairhall A. Sensory adaptation. *Curr Opin Neurobiol.* 2007;17(4):423-9.
3. Fairhall AL, Lewen GD, Bialek W, de Ruyter van Steveninck RR. Efficiency and ambiguity in an adaptive neural code. *Nature.* 2001;412:787-92.
4. Hildebrandt KJ, Ronacher B, Hennig RM, Benda J. A neural mechanism for time-window separation resolves ambiguity of adaptive coding. *PLoS Biol.* 2015;13(3):e1002096-e.
5. Krahe R, Bastian J, Chacron MJ. Temporal processing across multiple topographic maps in the electrosensory system. *J Neurophysiol.* 2008;100(2):852-67.
6. Ellis LD, Mehaffey WH, Harvey-Girard E, Turner RW, Maler L, Dunn RJ. SK channels provide a novel mechanism for the control of frequency tuning in electrosensory neurons. *J Neurosci.* 2007;27(35):9491-502.
7. McGillivray P, Vonderschen K, Fortune ES, Chacron MJ. Parallel coding of first- and second-order stimulus attributes by midbrain electrosensory neurons. *J Neurosci.* 2012;32(16):5510-24.
8. Chacron MJ, Longtin A, Maler L. Efficient computation via sparse coding in electrosensory neural networks. *Curr Opin Neurobiol.* 2011;21:752-60.
9. Lundstrom BN, Higgs MH, Spain WJ, Fairhall AL. Fractional differentiation by neocortical pyramidal neurons. *Nat Neurosci.* 2008;11(11):1335-42.
10. Clarke SE, Naud R, Longtin A, Maler L. Speed-invariant encoding of looming object distance requires power law spike rate adaptation. *PNAS.* 2013;110(33):13624-9.
11. Pozzorini C, Naud R, Mensi S, Gerstner W. Temporal whitening by power-law adaptation in neocortical neurons. *Nat Neurosci.* 2013;16(7):942-8.
12. Drew PJ, Abbott LF. Models and properties of power-law adaptation in neural systems. *J Neurophysiol.* 2006;96(2):826-33.
13. Rieke F. *Spikes: exploring the neural code*. MIT press; 1999.

Research Article

<sup>1</sup>Department of Biology, McGill University, Montreal, QC, Canada

<sup>2</sup>Department of Physiology, McGill University, Montreal, QC, Canada

<sup>3</sup>Department of Psychology, McGill University, Montreal, QC, Canada

<sup>4</sup>Department of Physics, McGill University, Montreal, QC, Canada

<sup>5</sup>Vestibular Gaze Control Lab, McGill University, Montreal, QC, Canada

<sup>6</sup>Authors contributed equally to the work

Keywords

$\alpha$ -9; mice; nAChR; vestibulo-ocular reflex; efferent

Email Correspondence

jesse.mendoza@mail.mcgill.ca

Jesse Mendoza<sup>1,2,3,5,6</sup>, Francis Grafton<sup>2,4,5,6</sup>, Amy Shan Wong<sup>2</sup>, Kathleen Cullen<sup>5</sup>

# Preserved Vestibular Function in Mice with Loss of $\alpha$ -9 Subunit of the $\alpha$ -9/10 Nicotinic Acetylcholine Receptor ( $\alpha$ -9/10 nAChR)

## Abstract

**Background:** The  $\alpha$ -9/10 nicotinic acetylcholine receptor is known to be the primary channel through which both vestibular and auditory efferents mediate the inhibition of their respective peripheral hair cells and afferents. With respect to the auditory system, the deletion of the  $\alpha$ -9 subunit results in abnormalities in the development of properly functioning cochlear hair cells. Given the high degree of similarity between the auditory and the vestibular systems, we hypothesize that  $\alpha$ -9 knockout mice should have impaired vestibular hair cell development and consequently compromised vestibular-mediated functions.

**Methods:** In order to characterize vestibular function in  $\alpha$ -9 knockout alert mice, we quantified the vestibulo-ocular reflex (VOR) through both gain and phase. Additionally, the optokinetic nystagmus (OKN) was similarly assessed as a control. VOR in light (VORI) was also quantified to further evaluate VOR and OKN efficacy. Furthermore, as information from the vestibular system mediates postural regulation and head stabilization, we assessed these properties through rotor rod and balance beam paradigms.

**Results:** Surprisingly, the loss of the  $\alpha$ -9 subunit in knockout mice did not result in any attenuation in VOR gain nor deviations in phase compared to wild type. OKN and VORI's gain and phase values remain similarly unchanged, confirming preserved function within the vestibular nucleus. Descending vestibulospinal information seems to be unaltered as well, as no significant difference was observed in postural testing.

**Limitations:** The  $\alpha$ -9 knockout mice used specifically had exon 1 and exon 2 of the  $\alpha$ -9 gene targeted, which could potentially limit generalizability. Also, frequencies greater than 3Hz were not tested.

**Conclusions:** Our findings demonstrate that  $\alpha$ -9 knockout mice still maintain normal vestibular function.

## Introduction

The vestibular system plays a fundamental role in the maintenance of posture, the stabilization of gaze, and our innate ability to sense self-motion. The physiological basis of this system is two distinct categories of sensory organs within the inner ear: the semicircular canals, which detect angular acceleration of the head, and the otoliths, which detect linear acceleration of the head. (1) Within these sensors, there are two types of vestibular hair cells: Type I and Type II. While the two types vary by morphology and afferent innervation, they both synapse onto primary vestibular afferents which project to neurons within the vestibular nuclei. The vestibular neurons innervate the abducens nucleus which then project onto oculomotor neurons, prompting eye movements that are involved in the vestibulo-ocular reflex. (2) The vestibulo-ocular reflex (VOR) stabilizes gaze in the presence of head movement by producing equal and opposite eye rotations to that of the head rotation, preserving image location in the center of the visual receptive field. Due to its simplicity and response properties, the VOR is often used as a method to test the functionality of the vestibular system in various species. Additionally, the vestibular nuclei project onto the spinal cord, where they mediate postural stabilization and higher order centers. (3)

The efferent vestibular system (EVS) is composed of neurons that synapse directly onto multiple hair cells and/or primary vestibular afferents in the vestibular end organs. (4-5) While many neuromodulators regulate the vestibular efferent system, acetylcholine is the primary neurotransmitter of this system. (3) Activation of the  $\alpha$ -9/10 nicotinic acetylcholine receptor (nAChR) in both the auditory and vestibular systems provides a means of efferent mediated inhibition. When activated, the  $\alpha$ -9/10 nAChR allows a transient influx of calcium followed by a coupling to the SK channel, causing

an efflux of potassium which then hyperpolarizes the cell. This hyperpolarization reduces further calcium influx and thus inhibits the release of glutamate onto afferents, causing overall cellular inhibition. (6-8) Many parallels are often drawn between the vestibular and auditory systems; it has been postulated that the auditory system evolved from the vestibular system. (9) As such, cross-system inferences can act as initial directives for determining potentially functional components in either system. To understand the role of the  $\alpha$ -9/10 nAChR subunits in the auditory system, Johnson (10) tested transgenic mice which lacked the  $\alpha$ -9 nAChR subunit gene in inner hair cells (IHCs). Evaluating the sensitivity of calcium influx through whole cell voltage-clamp recordings, measuring calcium current, and determining changes in cellular membrane capacitance showed that the IHCs of  $\alpha$ -9 knockout mice exhibited dependence similar to that of immature IHCs. This is indicative of a lack of normal maturation of the synaptic machinery. Inner hair cells were unable to respond to the inhibitory efferent input in the absence of the  $\alpha$ -9 subunit, a direct result of the failure in development of the auditory efferent system. While the  $\alpha$ -9/10 nAChR is known to play an important role in the auditory and vestibular efferent system, specifically in the IHCs, little is known about whether or how the loss of the  $\alpha$ -9 subunit influences overall vestibular function.

To that end, we assess the functional role of the  $\alpha$ -9 subunit of the  $\alpha$ -9/10 nAChR using the  $\alpha$ -9 null mouse strain. We first characterized the VOR and found no significant attenuation of VOR gain or phase in the  $\alpha$ -9 knockouts relative to wild type. Behavioral assays further demonstrated no significant difference in postural regulation between the  $\alpha$ -9 knockout and the  $\alpha$ -9 wild type mice. To assess the functionality of downstream innervations within the vestibular nuclei, we characterized the optokinetic nystagmus (OKN) response – a visually driven eye movement which works in conjunction with the VOR to stabilize gaze by producing eye motion in the same direction as visual motion. No significant deficit was found. Our

results suggest that vestibular efficacy is maintained even after removal of the  $\alpha$ -9 subunit of the  $\alpha$ -9/10 nAChR.

## Methods

### Animals

The  $\alpha$ -9 wild-type (+/+) and knockout (-/-) transgenic mice used in this study were generously provided by the laboratory of Dr. Barbara Morley of Boys Town National Research Hospital. These mice were created by targeting exon 1 and 2 of the  $\alpha$ -9 gene. The mice were then shipped to McGill University for eye movement and vestibular testing. A total of 16 mice were used, aged 5-6 months: 9  $\alpha$ -9 knockouts (5 female, 4 male) and 7  $\alpha$ -9 wild type (4 female, 3 male). The McGill University Animal Care Committee approved the use and care of the animals in accordance with the Canadian Council on Animal Care.

### Head Post Surgery

An aluminum head post was constructed to accommodate head restraint during eye recordings. Mice were anesthetized with an intraperitoneal injection of ketamine (100 mg/mL), xylazine (20 mg/mL), and acepromazine (10 mg/mL) in sterile isotonic saline. Once anesthetized, mice were given an analgesic subcutaneous injection of carprofen (concentration: 4 mg/ml; dosage: 5  $\mu$ L/g) prior to surgery. An incision was made and the skin was held back to expose the skull. An aluminum head post was secured to the skull using methods described by Muniak et al. (11) The incision was then sutured closed and Polysporin was applied to prevent infection. To prevent hypothermia and dehydration throughout surgery, a heating pad was placed underneath the mice and subcutaneous injections of isotonic saline (dosage: 0.2-0.5mL/10g body weight) were given when necessary. Analgesic injections of carprofen (concentration: 4 mg/mL; dosage: 5  $\mu$ L/g) were given every 24 hours during the next 24-48 hours of recovery.

### Eye Movement Data Acquisition

Mice were briefly anesthetized using gas isoflourane in order to restrain them in a plexiglass tube. Their heads were secured by screws in the surgically attached head post and pitched at  $\sim 30^\circ$  to align the semicircular canals with the horizontal plane. Once alert, each animal was then placed onto the center of the turntable, concentric with the drum, and secured (Fig.1). Eye movement data was recorded using an infrared video system (ISCAN). Head velocity was recorded using an angular velocity sensor. All signals were combined in REX (Real-Time Executive), a QNX-based (Unix-like operating system) real-time data acquisition system. (12) OKN eye movement responses were evoked by sinusoidal rotations of a drum placed around the turntable at frequencies 0.1, 0.2, 0.4, 0.8, 1, 2, and 3 Hz with peak velocities of both  $\pm 8^\circ/s$  and  $\pm 16^\circ/s$ . High contrast stripes ( $5^\circ$ ) were placed on the inside of the drum to ensure a response. To record VOR, the turntable was rotated at sinusoidal frequencies 0.1, 0.2, 0.4, 0.8, 1, 2, and 3 Hz with peak velocities of both  $\pm 8^\circ/s$  and  $\pm 16^\circ/s$  in both the light and dark. In the light condition, the drum remained stationary, while in the dark condition both the drum and turntable rotated in phase.

### Postural Data Acquisition

For the rotor rod task, mice were trained with trials of 5, 10, and 20 rpm for 120 seconds each, with 15 minutes rest periods between trials and a 1 minute acclimation period. Mice were allowed to acclimate for 5 minutes on the rotor rod during training and test trials. For each test trial, the rotor rod was programmed to accelerate from 4 rpm to 40 rpm with a ramp of 300 seconds, the maximum duration of the test. 3 trials were performed each day for 3 consecutive days.

For the balance beam task, a beam one meter in length and 14 mm in diameter, inclined 52.5-88.3 cm above the ground, was used. The mouse was held in a cardboard box at the end of the beam to acclimate to the goal location. During training, the mouse was placed directly outside of the box on the beam and allowed to walk in. A reward period of 1 minute was given after the mouse had reached the box. Once the mouse was trained, it was placed 60 cm away from the box and allowed to move across to

the goal position. This was repeated 5 times with 1 minute rest periods in between.

### Analysis

MATLAB by Mathworks was used to analyze all data. Least-square optimization (13) determined the VOR and OKN gains and phases, plotted as mean  $\pm$  standard deviation (SD) against all frequencies for all mice. For each rotor rod trial, the time at which the mouse fell from the rod was recorded. If the mouse resisted falling by grasping onto the rod, this was considered a failure and time was noted. The mean times  $\pm$  SD were then plotted. Traversal time of the balance beam was recorded for each trial and mean times  $\pm$  SD were plotted. To determine the statistical significance between the wild type and null knockout mouse a two-way ANOVA test with Bonferroni post hoc tests was used.

## Results

### $\alpha$ -9 Knockouts Demonstrate Unaltered VORd, OKN, and VOR1 Response Dynamics

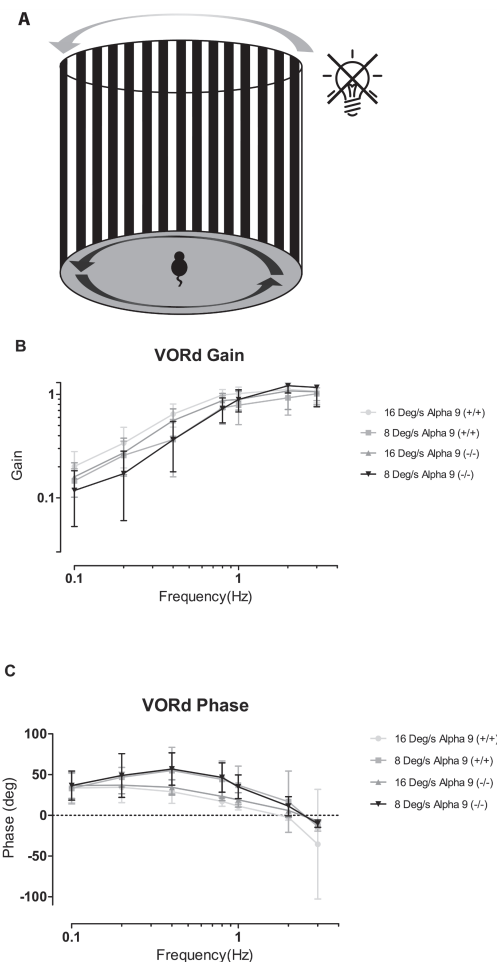


Fig. 1. Characterization of VORd.  $\alpha$ -9 (-/-) mice demonstrate normal VORd at peak velocities of 16 deg/s and 8 deg/s. (A) Schematic of recording set-up for VORd stimulation; movement of turntable and drum. (B, C) VORd gain and phase (mean  $\pm$  SD) plotted as a function of frequency for  $\alpha$ -9 (+/+) (n=7) and  $\alpha$ -9 (-/-) (n=8).

In our study, we subjected both  $\alpha$ -9 control and  $\alpha$ -9 knockout mice to three conditions: VORd (whole body rotation in darkness (Fig. 1A)), OKN (rotation of optokinetic drum with stationary mouse (Fig. 2A)), and VORl (whole body rotation in a lit environment with the optokinetic drum held stationary (Fig. 3A)). As the majority of head movements of mice during

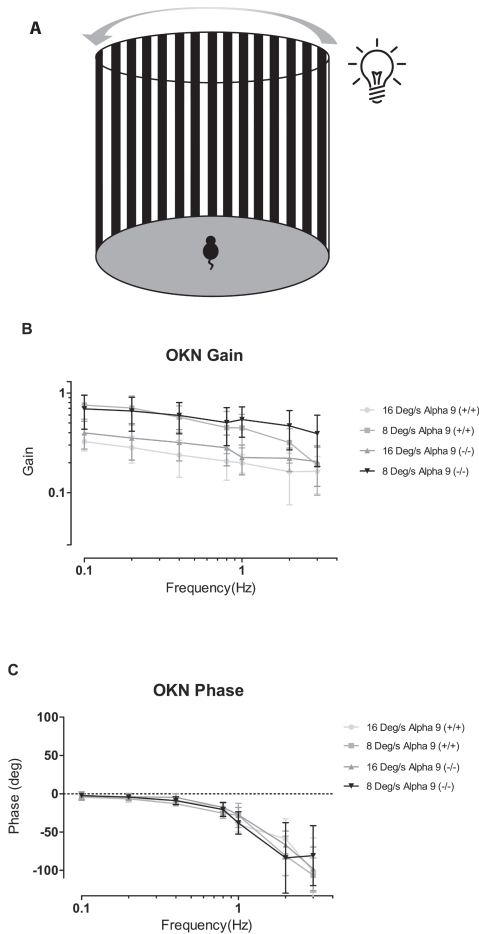


Fig. 2. Characterization of OKN.  $\alpha$ -9 (-/-) mice demonstrate normal OKN at peak velocities of 16 deg/s and 8 deg/s. (A) Schematic of recording set-up for VORd stimulation; movement of drum only. (B, C) OKN gain and phase (mean $\pm$ SD) plotted as a function of frequency for  $\alpha$ -9 (+/+) (n=7) and  $\alpha$ -9 (-/-) (n=8).

exploration have component frequencies less than 4 Hz, (13) all sinusoidal rotations were done at frequencies within this physiologically relevant range (0.1 Hz to 3 Hz). Furthermore, each condition was tested using peak angular velocities of 8°/s and 16°/s in order to evaluate any potential non-linearity in response differences between the strains.

Figures 1B, C depict the Bode plots for gain and phase respectively during the VORd condition. In accordance with previous characterizations, wild-type mice experience an increase in VOR gain with an increase in rotation frequency (Fig. 1B). For stimuli with peak velocity of 8°/s, the recorded gains ranged from  $0.146\pm 0.045$  at 0.1 Hz to  $1.014\pm 0.143$  at 3 Hz, and for 16°/s, gains ranged from  $0.201\pm 0.079$  at 0.1 Hz to  $1.069\pm 0.243$  at 3 Hz. Additionally, phase decreases as a function of frequency (Fig. 1C), such that the VORd initially leads with respect to the head velocity at lower frequencies and has a higher degree of compensation for higher frequencies. Surprisingly, knockout mice experience no attenuation in VORd gain compared to controls under the same peak velocity condition, as their gain values did not significantly differ across any frequencies (Fig. 1B;  $p > 0.05$ ). Furthermore, knockout mice did not significantly differ from controls with respect to phase at all frequencies tested (Fig. 1C;  $p > 0.05$ ).

In order to control for the possibility of the genetic mutation disrupting neural function elsewhere in the processing stream from the vestibular afferents within the VOR pathway, the dynamics of the optokinetic nystagmus (OKN) were assessed. The OKN pathway converges with the VOR pathway at the level of the vestibular nuclei; it is important to discount any

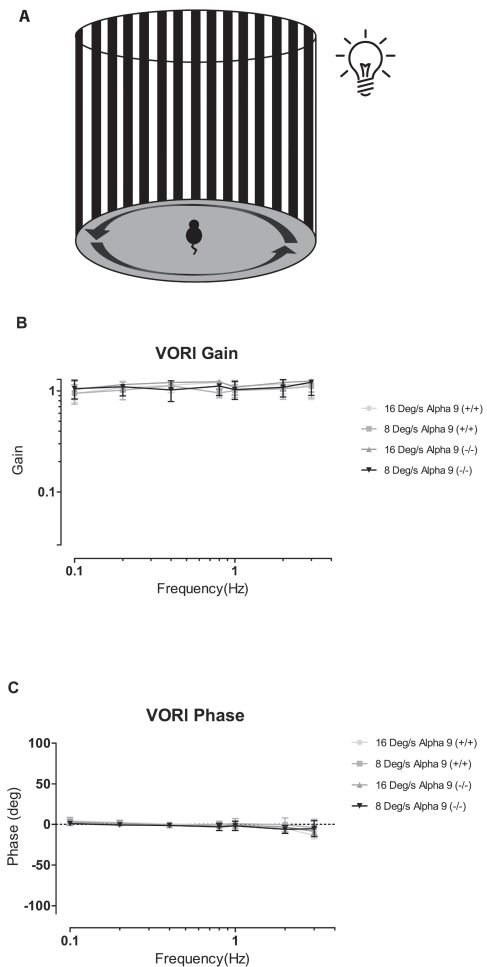


Fig. 3. Characterization of VORl.  $\alpha$ -9 (-/-) mice demonstrate normal VORd at peak velocities of 16 deg/s and 8 deg/s. (A) Schematic of recording set-up for VORl stimulation; movement of turntable only. (B, C) VORI gain and phase (mean $\pm$ SD) plotted as a function of frequency for  $\alpha$ -9 (+/+) (n=7) and  $\alpha$ -9 (-/-) (n=8).

alterations in OKN efficacy. Figures 2B, C represent the Bode plots for gain and phase respectively during the OKN condition. Comparing knockout mice to wild-type mice, differences in values for gain and phase across all frequencies in a given peak velocity condition were non-significant (Fig. 2B, c;  $p > 0.05$ ). Both knockout mice and wild-type mice demonstrate the general OKN trend in which gain decreases with increased frequency of the stimulus (Fig. 2B) and initial compensatory eye movement at low frequencies begins to lag with respect to the velocity stimulus at higher frequencies (Fig. 2C).

To further evaluate VOR and OKN efficacy, VOR was quantified in a lit environment (VORl). VORl represents a compound response of both OKN and VOR, where at lower frequencies OKN compensation dominates and at higher frequencies VOR compensates for the head motion. As VORd and OKN were not significantly altered between the two strains, we predicted that there should be no attenuation in VORl response. Figures 3B, C are the Bode plots for gain and phase respectively during the VORl condition. In accordance with our hypothesis, both knockout and wild-type mice show a general trend of near-perfect gain regardless of frequency and no significant difference in gain values across all frequencies in a given peak velocity condition (Fig. 3B;  $p > 0.05$ ). In addition, phase values were non-significant between both mice strains across all frequencies in a given peak velocity condition (Fig. 3C;  $p > 0.05$ ), where the eye movement remained compensatory throughout all frequencies.

## Postural Regulation and Balancing Capabilities Preserved in $\alpha$ -9 Knockout Mutants

The vestibular system's projections from the vestibular nuclei to the spinal cord, descending via the vestibulospinal tracts, provide necessary information for both head stabilization (14-16) and balancing through reflexive control of the limbs. (17) Should the  $\alpha$ -9 knockout impair normal development of vestibular hair cells, the neurons of the vestibular nuclei would receive distorted signals from the primary vestibular afferents and we would consequently anticipate abnormal motor behaviours when the subject attempts to balance or stabilize their head position. In order to assess the presence of such impairments, we chose to use two paradigms: the balance beam and accelerating rotor rod, both of which are common in evaluating balance and defective motor skill in mice. (18-19)

Both the control wild-type mice and  $\alpha$ -9 knockout mutant mice were subject to an initial training period of rotor rod testing, in which the angular velocity remained constant for a given trial but increased with subsequent trials, and a 3-day testing period with accelerating rotations (Fig. 4A). Comparing time to fall averaged across trials conducted on a given day (Fig. 4B),  $\alpha$ -9 knockout and control wild-type mice did not significantly differ on any given day (Fig. 4b;  $p > 0.05$ ). The balance beam test was performed on both wild-type and knockout mice, where the time taken to traverse the beam in order to reach a goal platform was measured. The knockout mice did not differ significantly from the wild-type controls in any of the trials (Fig. 4C).

## Discussion

In this study, we demonstrated that mice with a deletion of the  $\alpha$ -9 gene display normal vestibular function. We hypothesized that the loss of the  $\alpha$ -9 subunit used in vestibular efferent signaling would result in deficits in the development of vestibular hair cells and consequently alter the information transmitted by vestibular afferents, disrupting normal vestibular functions. However, characteristic features of the VOR, such as gain and phase, did not significantly differ between  $\alpha$ -9 knockout null mutants and  $\alpha$ -9 wild type specimens. Additionally, the lack of significant differences in OKN response dynamics confirmed that loss of the  $\alpha$ -9 gene has no effect downstream of the afferents within the VOR pathway, specifically on neurons in the vestibular nuclei. Furthermore, the rotor rod and balance beam paradigms suggest that vestibular postural control pathways remain functional despite the absence of the  $\alpha$ -9 gene.

### The $\alpha$ -9 subunit and EVS function

It is well established that acetylcholine is the main neurotransmitter released by the efferent vestibular system (EVS) onto peripheral vestibular targets. (3, 20-21) Though EVS's pattern of innervation is species-dependent, (3, 22) birds, reptiles, and mammals exhibit efferent innervation onto bouton and calyx vestibular afferents, type II hair cells, and transient interactions with type I hair cells. The  $\alpha$ -9 subunit investigated in this study plays a functional role within the  $\alpha$ -9/10 nicotinic acetylcholine receptor, which mediates efferent inhibition. (22-23) Despite detailed knowledge of the circuitry, the function of the EVS is still the object of contention. Often, the auditory efferent system is used as a means of comparison when considering the function of the EVS due to the similarities between the systems and the known functional role of the auditory efferent system.

A recent demonstration of such a parallel between these systems is their mutual reliance on the neurotransmitter calcitonin gene-related peptide (CGRP) for efferent signaling. The lateral olivocochlear (LOC) subdivision of the auditory efferent system innervates cochlear afferents and signals using CGRP, ACh, and gamma-aminobutyric acid (GABA). (24) While the loss of the  $\alpha$  isoform of the CGRP gene does not affect the function of the medial olivocochlear (MOC) efferent subdivision, which is involved in preventing acoustic trauma from injuring the cochlea, (25) it does result in a large attenuation of nerve activity in the auditory system. Similarly, CGRP is also involved in efferent signaling in the vestibular system. It has been shown that the loss of  $\alpha$ CGRP results in a 50% reduction in the gain, but not phase, of VOR. (26)

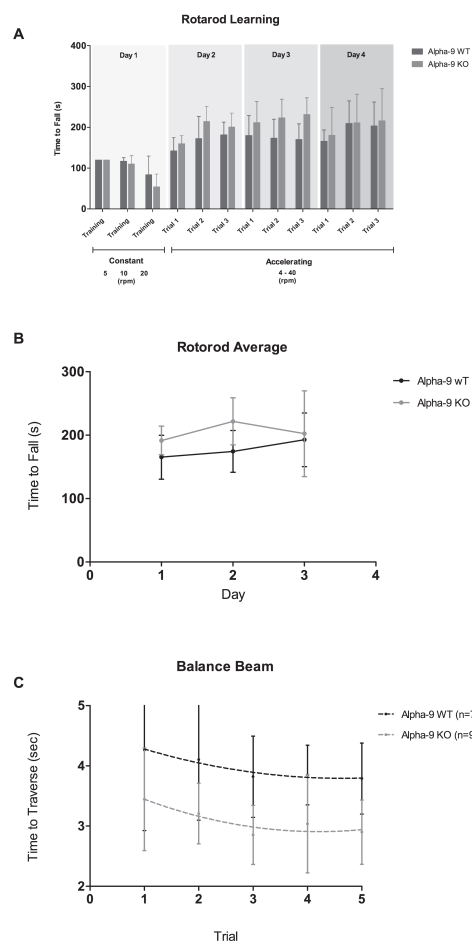


Fig. 4. Balance and postural regulation remain unaffected between strains for rotorod (A, B) and balance beam (C) paradigms. (A) Time to fall measured per trial (mean $\pm$ SD) for  $\alpha$ -9 (+/+) (n=7) and  $\alpha$ -9 (-/-) (n=9). (B) Time to fall averaged across trials per day demonstrate non-significant difference between strains. (C) Time to traverse the beam unaffected by  $\alpha$ -9 knockout.

Within the auditory system,  $\alpha$ -9/10 nAChRs have been shown to potentially influence synaptic strength through transient synapses and prevent deterioration of auditory hair cells by mediating auditory efferent signaling. (23, 27) Specifically, the  $\alpha$ -9 subunit appears to play a functional role in auditory hair cell maturation by influencing gene expression during development. (10, 28) These findings suggest a potential role for the  $\alpha$ -9 subunit in vestibular end organ development through vestibular efferent signaling. (29-32) Further supporting this proposition, the vestibular efferent system briefly synapses with Type I hair cells, similar to the transient synapses in the auditory system. These transient vestibular synapses are seen in early stages of development in mammals before calyces have formed and thus make direct contact with Type I hair cells. (33) However, our study suggests that the  $\alpha$ -9 subunit is not necessary for normal vestibular function, since  $\alpha$ -9 knockout mice and  $\alpha$ -9 wild-type control mice did not significantly differ in VOR gain or postural regulation.

The result of this study is surprising given that the  $\alpha$ -9 subunit acts in cells that are the initial step in the processing of vestibular information and yet the system is unchanged in its absence. It can therefore be asked whether the  $\alpha$ -9 subunit has any fundamental relevance to vestibular end organ development. We first consider that stimulation of the vestibular efferents in mammals produce almost exclusively excitation within the semicircular canal afferents. (22, 34-35) This suggests that a majority of the action from efferents is excitatory within mammals. Efferent-mediated excitation occurs through signaling of  $\alpha$ 4/ $\beta$ 2 nAChR for the fast component of the excitation, (34-37) and potentially through muscarinic acetylcholine receptors for the slow component of the excitation. (38-39) As noted,  $\alpha$ -9/10 nAChR

signaling mediates the inhibitory effects of efferent stimulation. Given that this study was performed with mice, it is possible that  $\alpha$ -9/10 nAChRs play a negligible role within the EVS of this animal model.

Here we found no significant changes in vestibular function, with respect to both the VOR and postural responses in  $\alpha$ -9 knockout mice. However, studies in a different  $\alpha$ -9 knockout mouse strain have described some changes in the VOR. Notably, a preliminary report has described changes in the VOR time constant and quick phase generation. (40) Further, a second study has recently reported changes in vestibular compensation after unilateral labyrinthectomy in this same strain. (41) One possible explanation for the discrepancy with our results is the different transgenic model used: we used  $\alpha$ -9 knockout mice for which a different location on the  $\alpha$ -9 gene (exons 1 and 2) was targeted. Additionally, Hübner and colleagues (41) tested VOR at higher frequencies and peak velocities than were tested in our study. Further experiments will be needed to examine this possibility.

Finally, the lack of vestibular impairment demonstrated in this study may also be the result of compensatory mechanisms that occur during development. It has been demonstrated that transgenic mice with a removal of the  $\alpha$ -9 subunit experience no difference in auditory behaviors, in both intensity discrimination and the psychophysical threshold for the detection of tone, when compared to a control strain. (42-43) The possibility arises that similar central and/or peripheral systems could potentially be compensating for such a mutation in the vestibular system as in the auditory system. Thus, any conclusions made on lack of deficits in the vestibular system due to the removal of the  $\alpha$ -9 subunit must take such compensation into consideration. If future studies demonstrate a lack of abnormalities in the circuitry connecting efferents with vestibular hair cells, it is still possible that compensatory mechanisms are negating developmental effects due to the deletion of the  $\alpha$ -9 subunit. The existence of other neurotrophic factors that may be acting as functional mediators in proper efferent targeting could potentially account for such compensation. To further determine whether the  $\alpha$ -9/10 nAChR has a functional role in vestibular end organ development, characterizations of possible compensatory mechanisms as well as any morphological and physiological consequences of a deletion of the  $\alpha$ -9 subunit on vestibular hair are required.

## Acknowledgements

The authors acknowledge support from the McGill University Dawson Chair program, the Natural Sciences and Engineering Research Council of Canada, and the Canadian Institutes of Health Research to K.E.C. Jesse Mendoza thanks the Natural Sciences and Engineering Research Council of Canada for the summer fellowship through the Undergraduate Research Award. We also thank Vanessa Chang and Dawoon Park for help with data acquisition.

## References

- Cullen, KE. The vestibular system: multimodal integration and encoding of self-motion for motor control. *Trends Neurosci.* 2012 Mar;35(3), 185-196.
- Scudder CA and Fuchs AF. Physiological and behavioural identification of vestibular nucleus neurons mediating the horizontal vestibulo-ocular reflex in trained rhesus monkeys. *J Neurophysiol.* 1992 Jul;68(1): 244-264.
- Holt JC, Lysakowski A, and Goldberg JM. Vestibular Efferents. The efferent vestibular system. In: *Auditory and Vestibular Efferents*. In: DKRe, editor. Springer Handbook of Auditory Research. Springer; 2011.
- Sienknecht UJ, Koppl C and Fritzsche B. Evolution and Development of Hair Cell Polarity and Efferent Function in the Inner Ear. *Brain Behav Evol.* 2014;83: 150-161
- Lysakowski A. Anatomy of Vestibular End Organs and Neural Pathways. 4th Edition In: *Otolaryngology: Vol. 4, Ear and Cranial Base* (Cummings CW). St. Louis: Mosby-Year Book Inc; 2010. pp. 3089-3111.
- Im GJ. Role of Nicotinic Acetylcholine Receptor on Efferent Inhibition in Cochlear Hair Cell. *Korean J Audiol.* 2012 Dec;16(3), 108-113.
- Kong J, Adelman JB, and Fuchs PA. Expression of the SK2 calcium-activated potassium channel is required for cholinergic function in mouse cochlear hair cells. *J Physiol.* 2008 Nov 15;586(22), 5471-5485.
- Turcan S, Slonim DK, Vetter DE, and Mansvelder HD. Lack of nAChR Activity Depresses Cochlear Maturation and Up-Regulates GABA System Components: Temporal Profiling of Gene Expression in  $\alpha$ 9 Null Mice. *PLoS ONE.* 2010;5(2): e9058.
- Duncan JS and Fritzsche B. Transforming the vestibular system one molecule at a time: the molecular and developmental basis of vertebrate auditory evolution. *Adv Exp Med Biol.* 2012;739 pp. 173-186.
- Johnson SL, Wedemeyer C, Vetter DE, Adachi R, Holley MC, Elgoyhen AB, and Marcotti W. Cholinergic efferent synaptic transmission regulates the maturation of auditory hair cell ribbon synapses. *Open Biol.* 2013 Nov;3(11), 130163-130163.
- Muniak MA, Mayko ZM, Ryugo DK, Portfors CV. Preparation of an awake mouse for recording neural responses and injecting tracers. *J Vis Exp.* 2012 Jun 26;(64). pii: 3755.
- Hayes AV, Richmond BJ, and Optican LM. A UNIX-based multiple process system for real-time data acquisition and control. In: *WESCON Conf Proc.*, vol. 2, 1-10, 1982.
- Beraneck M, McKee JL, Aleisa M and Cullen KE Asymmetric Recovery in Cerebellar-Deficient Mice Following Unilateral Labyrinthectomy. *J Neurophysiol.* 2008 Aug;100(2), 945-58.
- Grande G, Bui TV, and Rose PK. Distribution of vestibulospinal contacts on the dendrites of ipsilateral splenius motoneurons: An anatomical substrate for push-pull interactions during vestibulocollic reflexes. *Brain Res.* 2010 May 28;1333, 9-27.
- Mitchell DE, Dai C, Rahman MA, Ahn JH, Santana CC, and Cullen KE. Head Movements Evoked in Alert Rhesus Monkey by Vestibular Prosthesis Stimulation: Implications for Postural and Gaze Stabilization. *PLoS ONE.* 2013; 8(10): e78767.
- Goldberg JM and Cullen KE. Vestibular control of the head: Possible functions of the vestibulocollic reflex. *Exp Brain Res Exp Brain Res.* 2011 May;210(3-4), 331-345.
- Kasumacic N, Glover JC, and Perreault M. Segmental patterns of vestibular-mediated synaptic inputs to axial and limb motoneurons in the neonatal mouse assessed by optical recording. *J Physiol.* 2010 Dec 15; 588(24), 4905-4925.
- Luong TN, Carlisle HJ, Southwell A, and Patterson PH. Assessment of Motor Balance and Coordination in Mice using the Balance Beam. *J Vis Exp.* 2011 Mar 10; (49), 2376.
- Deacon RM. Measuring Motor Coordination in Mice. *J Vis Exp.* 2013 May 29;(75): e2609
- Soto E and Vega R. Neuropharmacology of Vestibular System Disorders. *Curr Neuropharmacol.* 2010 Mar;8(1), 26-40
- Yamashita T, Ohnishi S, Ohtani M, and Kumazawa T. Effects of Efferent Neurotransmitters on Intracellular Ca<sup>+</sup> in Vestibular Hair Cells of the Guinea Pig. *Acta Otolaryngol Suppl.* 1993;500, 26-30.
- Jordan PM, Parks XX, Contini D and Holt JC. A review of synaptic mechanisms of vestibular efferent signaling in turtles: Extrapolation to efferent actions in mammals. *J Vestib Res.* 2013;23: 161-175.
- Kong J, Zachary S, Rohmann KN, and Fuchs PA. Retrograde Facilitation of Efferent Synapses on Cochlear Hair Cells. *J Assoc Res Otolaryngol.* 2013 Feb;14(1), 17-27
- Maison SF, Adams JC, Liberman MC. Olivocochlear innervation in the mouse: immunocytochemical maps, crossed versus uncrossed contributions, and transmitter colocalization. *J Comp Neurol.* 2003a Jan 13;455:406-416.
- Maison SF, Luebke AE, Liberman MC, Zuo J. Efferent protection from acoustic injury is mediated via alpha9 nicotinic acetylcholine receptors on outer hair cells. *J Neurosci.* 2002 Dec 15;22(24):10838 -10846 .
- Luebke AE, Holt JC, Jordan PM, Wong YS, Caldwell JS, and Cullen KE. Loss of  $\alpha$ -Calcitonin Gene Related Peptide ( $\alpha$ CGRP) Reduces the Efficacy of the Vestibulo-ocular Reflex (VOR). *J Neurosci.* 2014 Jul 20; 34(31), 10453-10458.
- Liberman MC, Liberman LD, and Maison SF. Efferent Feedback Slows Cochlear Aging. *J Neurosci.* 2014 March 26;34(13), 4599-4607.
- Turcan S, Slonim DK, Vetter DE, and Mansvelder HD. Lack of nAChR Activity Depresses Cochlear Maturation and Up-Regulates GABA System Components: Temporal Profiling of Gene Expression in  $\alpha$ 9 Null Mice. *PLoS ONE.* 2010;5(2): e9058.
- Elgoyhen AB, Johnson DS, Boulter J, Vetter, DE, and Heinemann S.  $\alpha$ 9: An acetylcholine receptor with novel pharmacological properties expressed in rat cochlear hair cells. *Cell.* 1994 Nov;79(4), 705-715.
- Hiel H, Elgoyhen AB, Drescher DG, and Morley BJ. Expression of nicotinic acetylcholine receptor mRNA in the adult rat peripheral vestibular system. *Brain Res.* 1996 Nov 4;738(2): 347-35.
- Lustig LR, Peng H, Hiel H, Yamamoto T, and Fuchs PA. Molecular Cloning and Mapping of the Human Nicotinic Acetylcholine Receptor  $\alpha$ 10 (CHRNA10). *Genomics.* 2001 May 1;73(3), 272-283
- Anderson AD, Troyanovskaya M, and Wackym PA. Differential expression of alpha2-7, alpha9 and beta2-4 nicotinic acetylcholine receptor subunit in the vestibular end-organs and Scarpa's ganglia of the rat. *Brain Res.* 1997;778(2): 409-413
- Favre D and Sans A. The development of vestibular efferent nerve endings during cat maturation: ultrastructural study. *Brain Res.* 1978 Feb 24;142(2),

- 333-337.
34. Goldberg JM and Fernández C. Efferent vestibular system in the squirrel monkey: anatomical location and influence on afferent activity. *J Neurophysiol.* 1980 Apr; 43(4), 986-1025.
  35. Marlinski V, Plotnik M, and Goldberg J. Efferent Actions in the Chinchilla Vestibular Labyrinth. *J Assoc Res Otolaryngol.* 2004 Jun;5(2), 126-143.
  36. Brichta AM and Goldberg JM. Responses to efferent activation and excitatory response-intensity relations of turtles posterior-crista afferents. *J Neurophysiol.* 2000 Mar;83: 1224-1242.
  37. Holt JC, Lysakowski A, and Goldberg JM. Mechanisms of efferent-mediated responses in the turtle posterior crista. *J Neurosci.* 2006 Dec 20;26:13180-13193.
  38. Jordan PM, Shah A, Barsz K and Holt JC. Activation of muscarinic Ach receptors underlies efferent-mediated slow excitation in calyx-bearing afferents of the turtle posterior semicircular canal. *Association for Research in Otolaryngology Midwinter Meeting Abstracts.* 2010 Feb 6-10;33: 555
  39. Li GQ, Kevetter GA, Leonard RB, Prusak DJ, Wood TG and Correia MJ. Muscarinic acetylcholine receptor subtype expression in avian vestibular hair cells, nerve terminals and ganglion cell. *Neuroscience.* 2007 Apr 25;146: 384-402.
  40. Enron JN, Davidovics N, and Della Santina CC. Contribution of vestibular efferent system alpha-9 nicotinic receptors to vestibulo-oculomotor interaction and short-term vestibular compensation after unilateral labyrinthectomy in mice. *Neurosci Lett.* 2015 Aug 18;602, 156-161.
  41. Hübner PP, Khan SI, and Migliaccio AA. The mammalian efferent vestibular system plays a crucial role in the high-frequency response and short-term adaptation of the vestibulo-ocular reflex. *J Neurophysiol.* 2015 Dec 1;114(6):3154-65.
  42. May BJ, Prosen CA, Weiss D, Vetter D. Behavioral investigation of some possible effects of the central olivocochlear pathways in transgenic mice. *Hear. Res.* 2002 Sep;171(1-2):142-157.
  43. Prosen CA, Bath KG, Vetter DE, May BJ. Behavioral assessments of auditory sensitivity in transgenic mice. *J. Neurosci Methods.* 2000 Apr 1; 97(1):59-67.

Research Article

<sup>1</sup>Department of Neuroscience,  
McGill University, Montreal,  
QC, Canada

<sup>2</sup>Department of Pharmacology  
& Therapeutics, McGill University,  
Montreal, QC, Canada

Keywords

Noise correlation, neuronal spikes,  
motion coherence, visual perception

Email Correspondence

moushumi.nath@mail.mcgill.ca

Moushumi Nath<sup>1</sup>, Xinwen Zhu<sup>2</sup>

# Reduction in Noise Correlation is Associated with Improved Behavioural Performance

## Abstract

**Background:** Visual perception constitutes the dominant method by which we process our environment, yet the neuronal substrates that underlie visual perception in the brain are not well understood. Noise correlation, defined as the correlation in non-stimulus evoked activity between neurons, has been shown to impact both encoding and decoding processes of visual stimuli. We wanted to determine whether changes in noise correlation can predict behavioural performance in a coherent motion-detection task.

**Methods:** Two macaque monkeys (*Macaca mulatta*) were trained in a coherent motion-detection task, where they learned to fixate on a screen and anticipate the onset of a motion coherence stimulus. During this task, spike activity from pairs of neurons of the middle temporal area (area MT) were recorded and data was analyzed using MATLAB. Specifically, we examined noise correlation as a function of time and success rate in the task.

**Results:** We found a decrease in the correlation in activity between neurons in area MT prior to the onset of the motion coherence stimulus. This decrease was accompanied by improved behavioural performance in the motion coherence-detection task.

**Limitations:** The activity in pairs of neurons may not accurately represent overall activity in a population of neurons. In addition, control experiments to better assess the nature of the common input that leads to a reduction in noise correlation were not conducted.

**Conclusions:** Despite these limitations, we have shown that a reduction in noise correlation prior to stimulus onset is accompanied by improved behavioural performance, suggesting that noise correlation may be a critical parameter that can aid in our understanding of how visual perception occurs in the brain.

## Introduction

“Sensation is an abstraction, not a replication, of the real world”, stated the neuroscientist, Vernon Mountcastle. (1) This statement is particularly relevant to visual perception, the dominant method by which we process our surrounding environment. Yet it is not well understood how this abstraction of stimuli into visual perception occurs in the brain.

Multiple levels of analysis can be employed to understand this question. One can either look at how information is encoded in individual neuronal activity, or in the correlated activity between neurons. (2) There are several reasons why examining correlated activity between neurons is of interest. Noise correlation, defined as the correlation in activity between neurons that is non-stimulus evoked, is thought to limit the amount of information that can be encoded by a neuronal population. (3) This limitation can occur even with weak Pearson's correlation coefficients of  $r = 0.1$ , as noise correlations can impede stimulus-relevant signal decoding in systems that average neuronal activity. (4) Averaging neuronal activity facilitates signal detection by minimizing noise best when the noise between neurons is independent (noise correlation is equal to 0). In cases where the noise is correlated, averaging fails to remove it.

However, averaging is not the only possible mechanism by which signals can be decoded. For certain noise models, correlations may in fact improve coding accuracy. (5) It has also been found that only correlations proportional to the derivatives of the tuning curves of the neurons in question are information-limiting, so the overall pairwise correlation may not be a meaningful indication of information-coding capacity. (6)

Finally, reductions in noise correlation have been proposed to be the main

mechanism by which attention improves performance on tasks that involve responses to visual stimuli. (7, 8) Combined, this information suggests that noise correlation is a functionally relevant parameter that may impact both encoding and decoding processes in the brain.

The goal of the present study was to determine whether changes in noise correlation over time would be observed in the middle temporal area (area MT) of macaque monkeys performing a coherent motion-detection task, where motion coherence is defined as the degree to which all particles within a patch are moving in the same direction, and whether this change would be associated with changes in behavioural performance.

## Methods

### Experimental Setup

Activity from pairs of neurons in area MT were recorded from two macaque monkeys performing a coherent motion-detection task that they were previously trained in. Monkeys visually fixated within a 2° square fixation window and the time of fixation was designated  $t=0$  or  $t_0$ . Following fixation, particles within either one or both of two patches presented onscreen that were initially moving in random direction began moving in a coherent manner (of varying degree) towards a specific direction (Fig.1). The onset of this coherence varied per trial between 200 ms to 1000 ms from the time of fixation, and the motion coherence pulse lasted for 50 ms. Once the monkey detected the onset of coherence, it had to release a lever within 200 ms to 800 ms from the pulse onset to receive a reward. Trials where the lever was released within this time window from the onset of coherence were deemed successful.

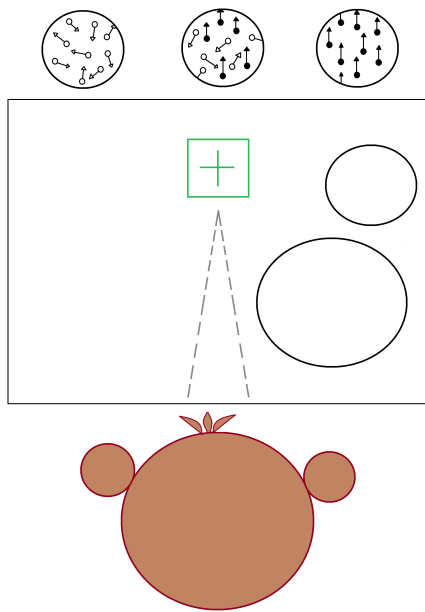


Fig. 1. Top panel presents motion coherence stimulus, with increasing degree of coherence in particle movement from left to right (0%, 50%, 100%). Bottom panel presents experimental setup. Monkey fixates (represented by dotted lines) within square window marked by cross. After a certain period of time, particles in either or both patches presented onscreen begin moving in a coherent manner.

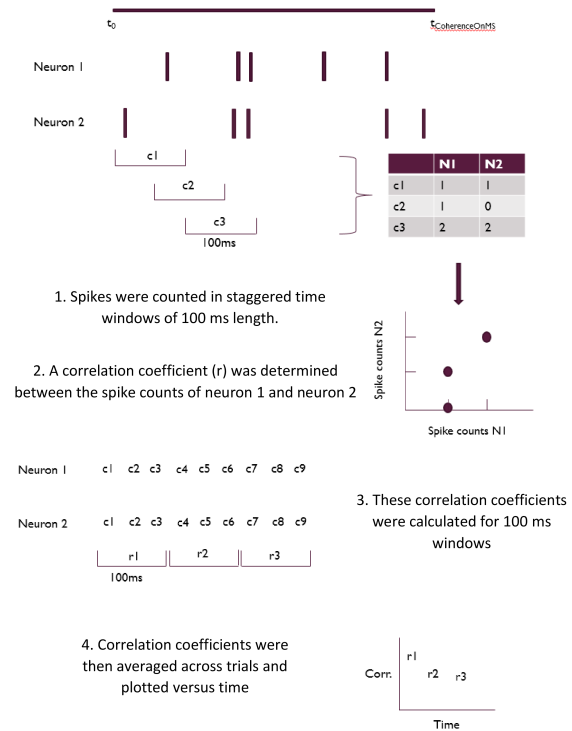


Fig. 2. Schematic of MATLAB analysis. For each trial, the number of spikes in staggered 100 ms windows was counted, generating the values  $c_1, c_2, \dots$  for each neuron. Correlations were calculated between the values  $c_1, c_2, \dots$  in 100 ms intervals (correlation windows). These correlations were averaged across trials and plotted versus time.

### Extracted Data from Experimental Structures

Extracted data from each experiment used in our MATLAB analysis included the spike times of two recorded neurons, neuron 1 and neuron 2, the time of coherence onset, and whether the lever was released. These data were extracted per trial, from all conditions (coherence in either one or both patches), from each experiment. Since our aim was to detect changes in noise correlation between pairs of neurons before the onset of a motion stimulus in monkeys trained to expect a stimulus, we did not differentiate between the different conditions, as the exact nature of the eventual stimulus was not expected to change the prior activity of the neurons. We analyzed 49 experiments for a total of 22,486 trials.

### Noise Correlation as a Function of Time

To evaluate how noise correlation changes as a function of time within a single trial, we first generated a list of spike counts, one for each neuron. The number of spikes was counted in staggered 100 ms windows, in a “moving boxcar” manner, from the fixation time  $t_0$  (included), to the time of motion coherence onset, coherenceOnMS (excluded). Once these lists were generated, we calculated the Pearson’s correlation coefficient for the spike counts between neurons within 100 ms windows, termed correlation windows (Fig. 2), restricted to the same time frame as the list of spike counts ( $t_0$  to coherenceOnMS). These calculations were made for each trial. Correlation windows in which a correlation coefficient could not be calculated because there were no changes in spike count in either neuron were excluded from further analysis. These correlation coefficients were then averaged across all trials in all conditions and all experiments. The average correlation coefficient for each correlation window was then plotted as a function of time. Standard error means (SEM) were determined for each correlation window.

### Task Performance

To assess whether changes in noise correlation are associated with behavioural performance, we measured behavioural performance as the fraction of successful trials over total trials, and plotted these measures as

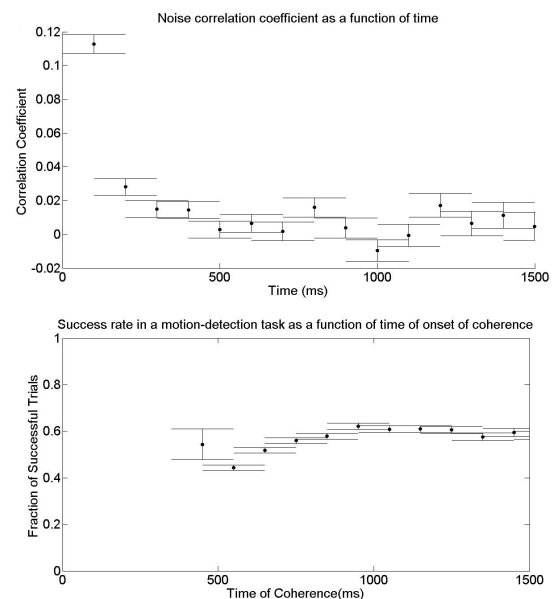


Fig. 3. Top: averaged correlation coefficients in 100 ms bins as a function of time. Bottom: fraction of successful trials, in which a lever was released following detection of motion coherence, as a function of the time of motion coherence onset. Plotted S.E.M. bars per bin.

a function of the time of motion coherence onset. These values were then binned in 100 ms windows. Standard error means were determined for each bin as was done for the correlation coefficients, assuming that each

trial follows a Bernoulli distribution where a successful trial has a value of 1 and a failed trial has a value of 0.

### Correct Versus Failed Trial Separation

To determine if changes in noise correlation would differ between correct trials and failed trials, we performed the same analysis as described in 'Noise correlation as a function of time', but separately for correct versus failed trials.

## Results

To determine if changes in noise correlation in area MT of macaque monkeys were observed during a motion-detection task, we compared spikes recorded from pairs of neurons from the time at which the monkey visually fixated on a point (inclusive) to the time of onset of the motion stimulus (exclusive). Correlations were calculated per correlation window of 100 ms. We found a decrease in noise correlation, from a value of 0.11 to 0, within 500 ms from the time of fixation. After this period, the activity between neurons remained independent ( $r=0$ ) (Fig. 3, top).

To see if this reduction in noise correlation was associated with changes in behavioural performance in the motion-detection task, we compared the success rate, a ratio of successful trials over total trials, to the onset of motion coherence which varied in each trial. We observed a modest increase in the fraction of trials that were successful, from 0.44 for trials with coherence times between 500 ms and 600 ms to 0.60 for trials with coherence times at approximately 1 second (Fig. 3, bottom). The success rate for trials with coherence times between 400 ms and 500 ms was calculated to be 0.54, and thus does not follow the same trend; however, since there were very few trials with coherence times between 400 ms and 500 ms, the discrepancy could be attributed to error due to small sample size. Comparing the two graphs in Fig. 3, we see that noise correlation decreased rapidly within 500 ms from fixation time, where very little data for success rate is available. Between 500 ms and 1000 ms, where success rate increased, there is a moderate negative correlation between average noise correlation and success rate ( $r=-0.42$ ). Both values then plateaued, where noise correlation equaled to 0 and success rate equaled to 0.6. These results suggest that a reduction in noise correlation in area MT may be

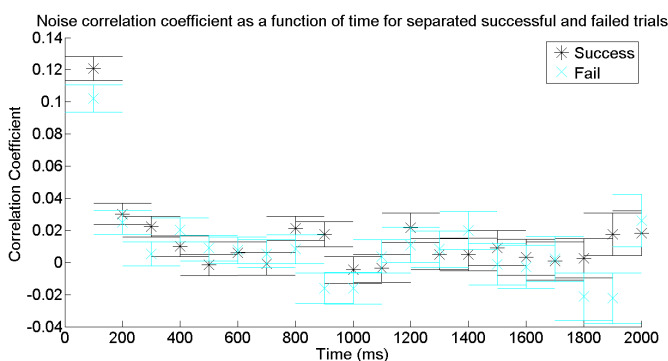


Fig. 4. Averaged correlation coefficients in 100 ms bins as a function of time, separated for successful (black) versus failed (grey) trials. There is no significant difference in the changes in correlation with time between successful and failed trials, although the initial average correlation coefficient for successful trials (0.12) is slightly higher than that of failed trials (0.10). Plotted S.E.M. bars.

associated with improved behavioural performance in the coherent motion-detection task.

To determine if changes in noise correlation differed between successful trials and failed trials, we assessed noise correlation separately for correct versus failed trials from the time of fixation to the onset of motion coherence. There appeared to be no significant difference in the time course of noise correlation between correct and failed trials. There is, however, a

small difference in the initial noise correlation value between correct and failed trials, which were 0.12 and 0.10, respectively (Fig. 4).

## Discussion

It is important to note that while previous experiments (4, 7, 8) calculated noise correlations across trials for a pair of neurons, thus measuring correlations in trial-to-trial fluctuations, we chose to calculate the noise correlation between a pair of neurons for each trial before averaging the correlations across all trials. We chose this because our interests lay primarily in the change in noise correlation as a function of time during anticipation of a stimulus, rather than in trial-to-trial variability. Nevertheless, we obtained initial noise correlations close to those previously reported (7), although a direct comparison of our results would not be appropriate due to the differing methods of calculation.

Our observed reduction in noise correlation appeared to be associated with increased success rates, but the progression did not vary between correct versus failed trials. These results suggest that while noise correlation may facilitate encoding of a visual stimulus, thereby increasing the probability of a successful trial, it may not be the distinguishing factor between correct versus failed trials. In other words, additional parameters, which have been found to be related to behavioural output, such as firing rates, may play a greater role in determining a successful trial. (9) These results contrast a previous study that has shown that behavioural performance in orientation-change detection tasks is improved primarily by reducing noise correlations in visual area V4. (7) It is possible that higher-order processing structures, such as area MT compared to V4, may incorporate a greater number of parameters in processing a visual stimulus. This would reduce the contribution of an individual parameter, such as noise correlation.

The increased success rate was seen in trials with coherence onset between 500 ms and 1 second after fixation, and success rate appeared to plateau at roughly 800 ms, while the average interneuronal correlation coefficient decreased to 0 by 500 ms. A delay of 300 ms from the time at which the noise correlation plateaued to the time at which the success rate plateaued indicates that these two phenomena cannot be said to occur on the same time scale. This delay may have arisen from integration of the noise correlation by downstream structures to area MT. In other words, a delay of at least 300 ms from the time of fixation to the onset of motion coherence may be sufficient to integrate the reduction in noise correlation in area MT in order to improve behavioural performance. Unfortunately, there were very few trials with coherence times before 500 ms and no trials with coherence times before 400 ms. Therefore, we have insufficient data to make conclusive statements.

While the lack of distinction between successful and failed trials when the correlation coefficients were averaged and plotted separately for each trial does not suggest that decreased correlation coefficients lead to improved performance at responding to stimuli, it does not preclude the possibility of a relationship. A potential experiment to test the relevance of noise correlations could involve maintaining weak activity correlations in area MT as the animal performs the same task. If a decrease in correlation coefficient is truly necessary to see an increase in performance, we would expect the increased performance to be abolished. However, we do not have a suitable method for manipulating correlated activity in the brain, as we do not yet know the mechanisms by which interneuronal correlation is modulated. Nevertheless, manipulation of noise correlation has been attempted with optogenetic methods. (10)

The nature of the common input that modulates noise correlation in area MT was not investigated in this study. It is possible that this common input reflects a change in attentional state following fixation. (7) However, given that our data analysis was restricted to the time from fixation to the onset of motion coherence, we did not have an inattention control. With respect to this limitation, it would be of interest to examine noise correlation prior to fixation as a potential measure for inattentiveness.

The observed reduction in noise correlation may also relate to an expected

change. In other words, visually fixating at a point that does not predict a presentation of a stimulus does not lead to a reduction in noise correlation, but fixating at a point that does predict a presentation of a stimulus does lead to a noise correlation reduction at fixation time.

## Conclusion

Understanding the molecular basis of this common input is imperative to establishing a causal relationship between noise correlation and behaviour. One postulation would be that upstream structures release neuromodulators such as acetylcholine, which have been functionally associated with attention (11), thus regulating the activity of neurons from area MT. In addition to previously mentioned optogenetic approaches, it would be feasible to use pharmacological molecular targets in order to assess causality.

It is important to keep in mind while discussing these results that activity from pairs of neurons may not accurately represent activity from a population of neurons. (3) Technique wise, it is difficult to record from multiple neurons simultaneously while still being able to distinguish individual neuronal activity. Extracellular recordings or electroencephalograms only provide summed activity from a focal point. In addition, the data we have presented is only correlational, not causal.

Further investigation is required to better understand how noise correlation can influence behaviours and what mechanisms modulate noise correlation. In the present study, we see a reduction in average noise correlation between pairs of neurons before the onset of an expected stimulus that is associated with improved behavioural performance.

## Acknowledgements

We would like to thank Dr. Erik Cook for providing us with the data, project background, and guiding us through the MATLAB analysis. We would also like to thank Alireza Hashemi for guidance on statistical analysis.

## References

1. Mountcastle VB. The view from within: pathways to the study of perception. *John Hopkins Medical Journal*. 1975; 136:109-31.
2. Averbach BB, Latham PE, Pouget A. Neural correlations, population coding and computation. *Nature Reviews Neuroscience*. 2006; 7(5):358-66.
3. Eyherabide HG, Samengo I. When and why noise correlations are important in neural decoding. *Journal of Neuroscience*. 2013; 33(45):17921-36.
4. Zohary E, Shadlen MN, Newsome WT. Correlated neuronal discharge rate and its implications for psychophysical performance. *Nature*. 1994; 370(6485):140-3.
5. Abbott LF, Dayan P. The effect of correlated variability on the accuracy of a population code. *Neural Computation*. 1999; 11(1):91-101.
6. Moreno-Bote R, Beck J, Kanitscheider I, Pitkow X, Latham P, Pouget A. Information-limiting correlations. *Nature Neuroscience*. 2014; 17(10):1410-17.
7. Cohen MR, Maunsell JH. Attention improves performance primarily by reducing interneuronal correlations. *Nature Neuroscience*. 2009; 12(12):1594-600.
8. Mitchell JF, Sundberg KA, Reynolds JH. Spatial attention decorrelates intrinsic activity fluctuations in macaque visual area V4. 2009; 63(6):879-88.
9. Smith JET, Zhan CA, Cook EP. The functional link between area MT neural fluctuations and detection of a brief motion stimulus. *Journal of Neuroscience*. 2011; 31(38):13458-68.
10. Nandy AS, Nassi JJ, Reynolds JH. Optogenetically induced low-frequency correlations impair perception (Unpublished).
11. Klinkenberg I, Sambeth A, Blokland A. Acetylcholine and attention. *Behavioural Brain Research*. 2011; 221(2):430-42.

Research Article

<sup>1</sup>Department of Anatomy & Cell Biology, McGill University, Montreal, QC, Canada

<sup>2</sup>Faculty of Dentistry, McGill University, Montreal, QC, Canada

Keywords

Osteoclasts, osteoclastogenesis, Ca<sup>2+</sup> oscillations, fluorescence imaging

Email Correspondence

mariya.stavnichuk@mail.mcgill.ca

Mariya Stavnichuk<sup>1</sup>, Gulzhakhan Sadvakassova<sup>2</sup>, Svetlana Komarova<sup>1,2</sup>

# Fluorescence Imaging of Receptor Activator of Nuclear Factor Kappa-B Ligand-Mediated Calcium Oscillations in Osteoclasts

## Abstract

**Background:** Numerous bone diseases are caused by abnormal activity of osteoclasts, cells responsible for physiological bone degradation. Understanding the mechanisms of osteoclast formation and activation is important for developing diagnostic tools and treatments for various bone diseases. Receptor activator of nuclear factor  $\kappa$ B ligand (RANKL), a key osteoclastogenic cytokine, induces changes in intracellular Ca<sup>2+</sup> concentration ([Ca<sup>2+</sup>]<sub>i</sub>) that can be visualized and measured with a fluorescent Ca<sup>2+</sup> binding dye. The objective of the study was to characterize the changes in [Ca<sup>2+</sup>]<sub>i</sub> induced by acute application of RANKL in osteoclast precursors.

**Methods:** We performed calcium imaging in osteoclast precursors generated from RAW 264.7 cells loaded with Fura-2 fluorescent dye using an inverted microscope, Nikon TE2000-U. Data was collected with Volocity software and analysed in Excel and MATLAB.

**Results:** In osteoclast precursors, RANKL induced oscillations in [Ca<sup>2+</sup>]<sub>i</sub> within 2 minutes of exposure. The main frequency of oscillations was approximately 37.7 mHz. However, no significant change in the mean level of intracellular Ca<sup>2+</sup> was observed. Interestingly, when ATP was applied to RANKL-treated osteoclast precursors, it induced a long-lasting increase in [Ca<sup>2+</sup>]<sub>i</sub> compared to control cells.

**Limitations:** The limitations of our study included the small number of replicates and the short duration of fluorescence recording under each condition.

**Conclusions:** Short exposure of osteoclast precursors to RANKL not only induced oscillations in calcium concentration, but also modulated cellular response to the subsequent application of ATP.

## Introduction

Bone is an organ that continuously undergoes remodelling activity to cater to the demands of the organism. Its dynamic equilibrium depends on the balance between bone-forming cells, osteoblasts, and bone-resorptive cells, osteoclasts. Understanding the underlying causes of bone homeostasis is important for developing treatments against various diseases that result from an imbalance in bone remodelling. A large number of bone diseases, such as metastatic cancers, osteoporosis, and rheumatoid arthritis arise from increased resorption of bone by osteoclasts. (1) Osteoclasts are cells of hematopoietic origin formed by differentiation of monocyte or macrophage precursors. (2) Osteoclastogenesis is initiated by receptor activator of nuclear factor  $\kappa$ B's (RANK) stimulation by its ligand, RANKL. (3) Activation of RANK leads to subsequent induction of co-stimulatory receptors such as the osteoclast-associated receptor (OSCAR), which results in activation of phospholipase C (PLC), and formation of inositol-1,4,5- triphosphate (IP<sub>3</sub>), which binds to its receptor on the endoplasmic reticulum releasing stored Ca<sup>2+</sup>. (3) Resulting cytosolic Ca<sup>2+</sup> concentration oscillations are important for stimulation of the calcineurin/NFATc1 that is essential for osteoclastogenesis. (3) In addition to RANKL, multiple other factors are known to affect osteoclast calcium, including extracellular ATP that can be produced by mechanically stimulated cells. (3) Extracellular ATP activates plasma membrane P<sub>2</sub> purinergic receptors inducing a fast transient increase in [Ca<sup>2+</sup>]<sub>i</sub>. (5)

The objective of this study was to investigate changes in cytosolic Ca<sup>2+</sup> concentration in response to RANK-RANKL interaction. Intracellular Ca<sup>2+</sup> oscillation can be visualized using a fluorescence microscope. In this experiment, we used Fura-2, a ratio-metric fluorescent dye that binds free intracellular Ca<sup>2+</sup>. The advantage of ratiometric dyes over single wavelength

dyes is that the obtained ratio is independent of the dye concentration. (4) The dye is loaded into cells in the form of an acetoxy-methyl-ester Fura-2 (Fura-2 AM) and it is de-esterified by cellular esterases, leaving Fura-2 trapped in the cell. (4) Fluorescence microscopes have an excitation filter that allows a specific excitation wavelength to go through. Excitation light is reflected from a dichromatic mirror, which directs light onto the specimen. Fura-2 has the property of being excited at 340 nm in its calcium-free form and at 380 nm when bound to Ca<sup>2+</sup>. The excited sample emits light that passes through the mirror and emission filter of 510 nm for Fura-2. (4)

## Methods

### Cell Culture

We used RAW 264.7 cells (American Type Culture Collection) derived from a mouse leukemic monocyte macrophage cell line as osteoclast precursors. Cells were cultured at 37°C and 5% CO<sub>2</sub> in 2 mL DMEM (319-020-CL, Wisent Inc.) supplemented with 1% penicillin-streptomycin (450-201-EL, Wisent Inc.), 10% FBS (080-150, Wisent Inc.), and 50 ng/mL of recombinant GST-RANKL (produced in-house, 50  $\mu$ g/mL). RANKL was added in order to induce differentiation of monocytes into osteoclast precursors. We plated cells at 5x10<sup>3</sup> cells/cm<sup>2</sup> in 35 mm glass bottom cell culture dishes (MatTek Corp.). After two days, media was changed to DMEM containing 1.5  $\mu$ M Fura-2 AM (F1221, Invitrogen). 30 minutes after media change, cells were washed with 1 mL DMEM buffered with 10 mM HEPES (15630-080, Gibco) and another 1 mL of HEPES-buffered DMEM was added to cells. After addition of Fura-2 AM, dishes were either covered with aluminium foil or manipulated in darkness to prevent bleaching.

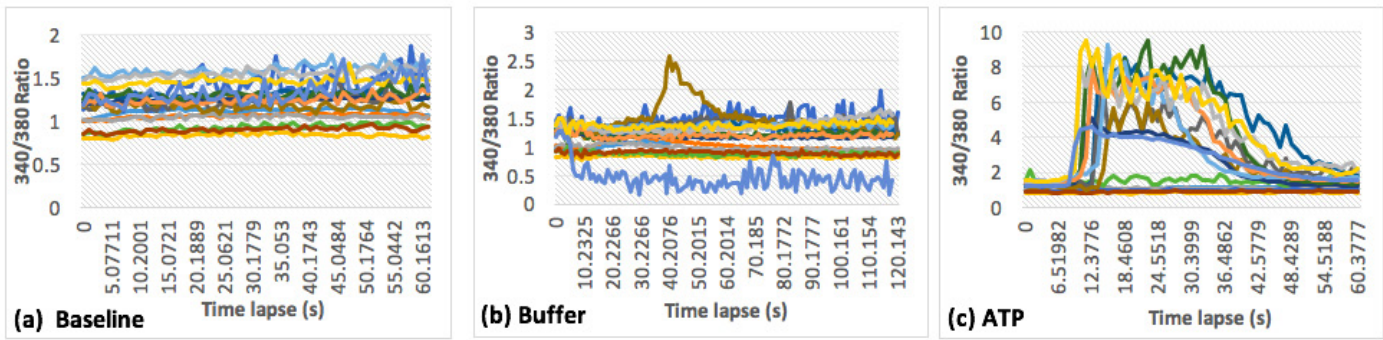


Fig. 1. Changes in  $[Ca^{2+}]_i$  following addition of buffer. Each line graph represents single-cell fluorescence intensity ratio measurement. (A) Baseline measurements of fluorescence intensity. (B) Fluorescence intensity after addition of the buffer. (C) Fluorescence intensity after addition of ATP.

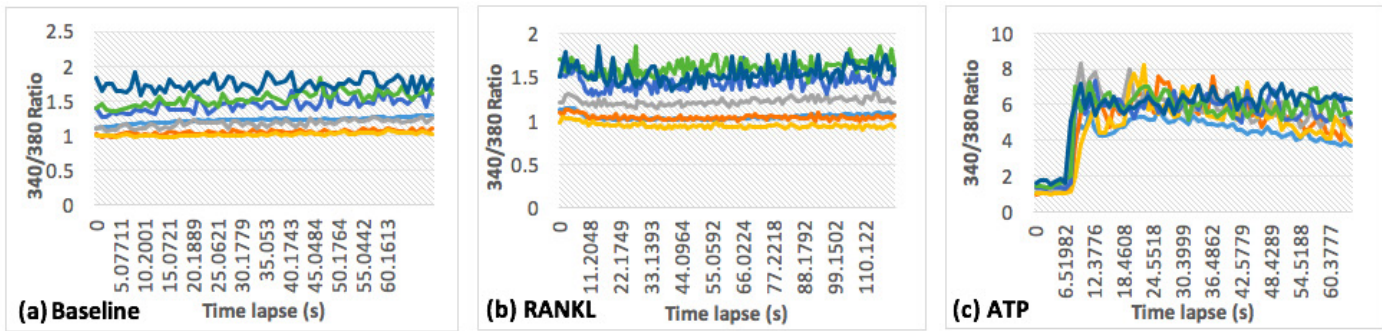


Fig. 2. Changes in  $[Ca^{2+}]_i$  following addition of RANKL. Each line graph represents single-cell fluorescence intensity ratio measurement. (A) Baseline measurements of fluorescence intensity. (B) Fluorescence intensity after addition of RANKL. (C) Fluorescence intensity after addition of ATP.

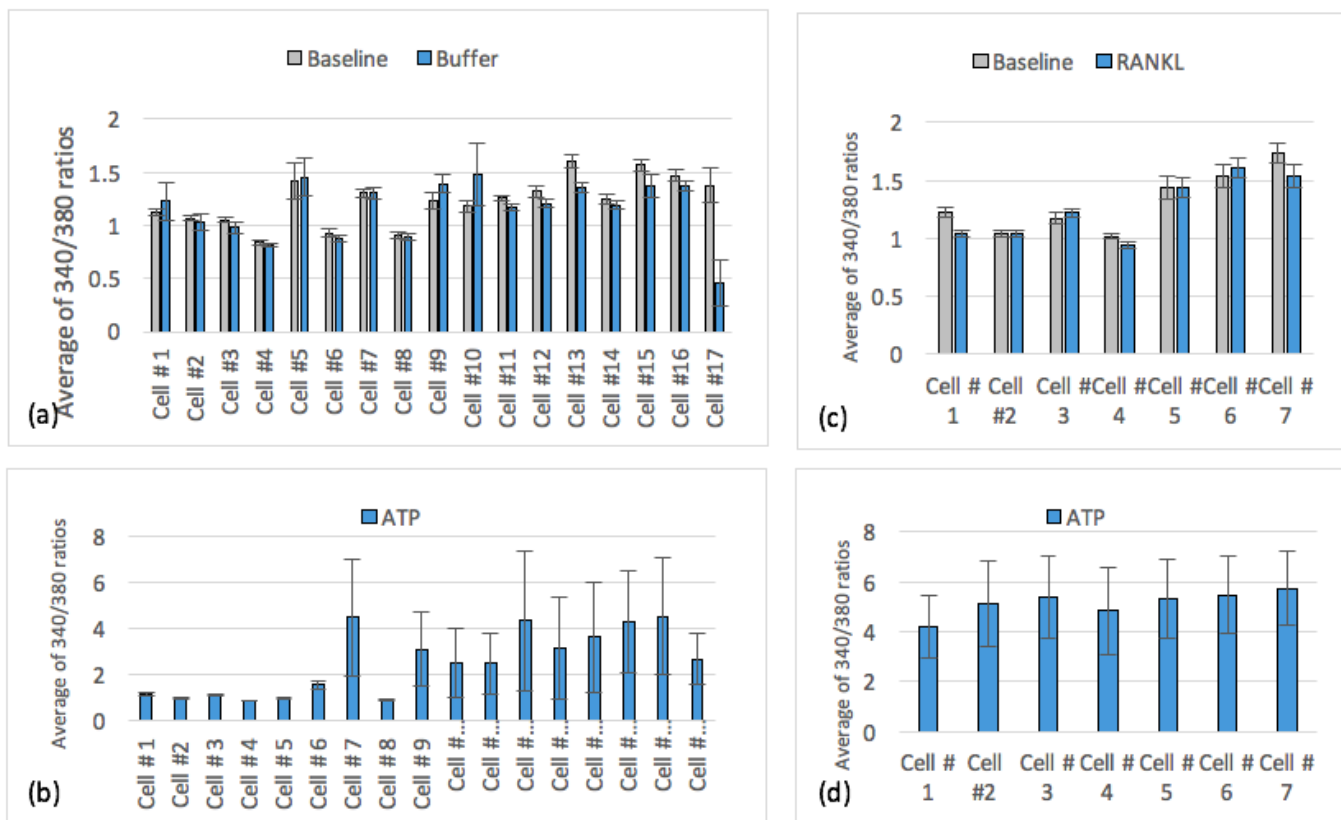


Fig. 3. Average level of  $[Ca^{2+}]_i$  after addition of buffer, RANKL or ATP. The same cells were examined in charts (A) and (B), and in charts (C) and (D). Shown is average fluorescence intensity (A) at the baseline (grey) and after buffer addition (blue); (B) after ATP addition; (C) at the baseline (grey) and after RANKL addition (blue); (D) after ATP addition.

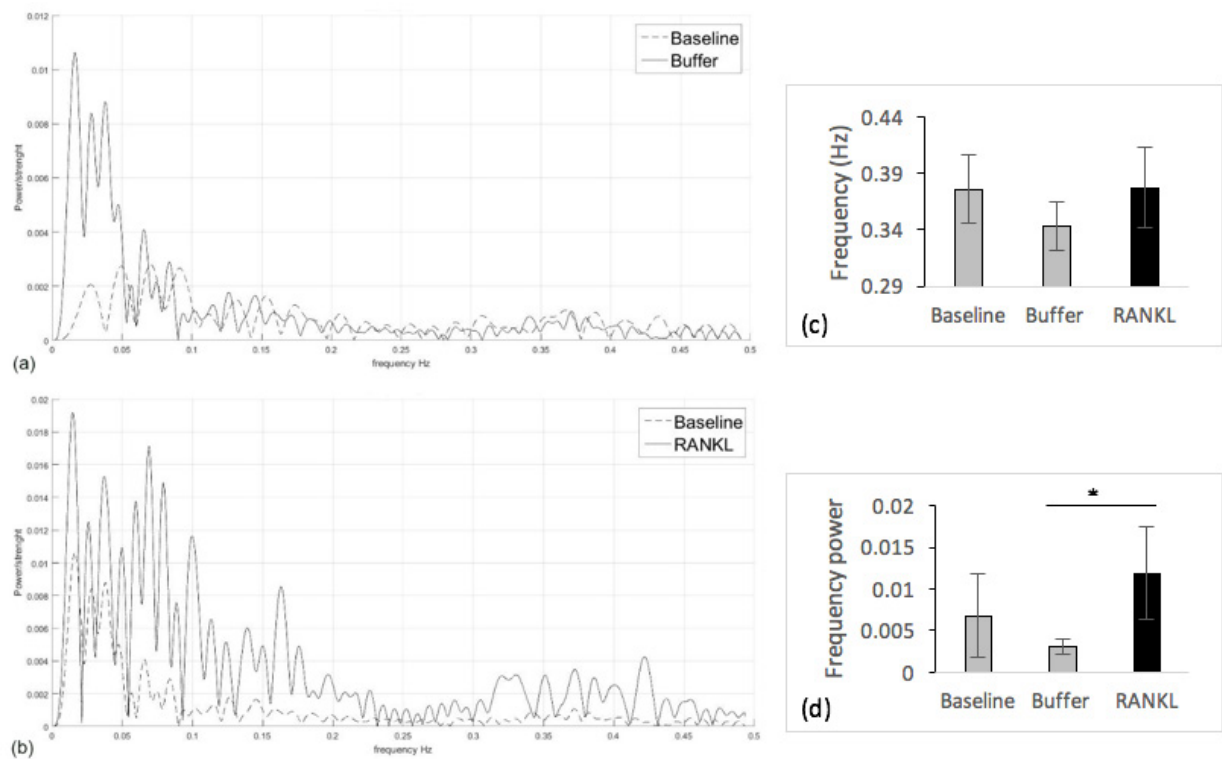


Fig. 4. Spectral analysis of  $[Ca^{2+}]_i$  oscillations. Average power spectrum analysis (A) at the baseline and after buffer addition and (B) at the baseline and after RANKL addition. (C) Average dominant frequency of  $[Ca^{2+}]_i$  oscillations between 20-50 mHz. (D) Average strength of dominant frequency of  $[Ca^{2+}]_i$  oscillations between 20-50 mHz. Data are means  $\pm$  SD, \* indicates  $p < 0.05$  examined by Student's t-test.

## Fluorescence Imaging

The cells were given 15 minutes to acclimatize before imaging. We performed imaging on an inverted Nikon TE2000-U microscope equipped with a cooled charge-couple device (CCD) camera (Hamamatsu) and 40X UV corrected Nikon Fluor oil immersion objective. We recorded fluorescence emission data points every second at 510 nm after excitation at 340 and 380 nm alternated by a high speed wavelength switching device (Lambda DG-4, Quorum Technologies). In each dish, the measurement consisted first of a baseline recording for one minute. Either 50  $\mu$ L of buffer solution or 50 ng/mL of RANKL was added with a micropipette six to eight seconds after the start and fluorescence intensity was recorded for two minutes. Finally, 50  $\mu$ L of 10 mM ATP was added, giving a final concentration of 10  $\mu$ M, and fluorescence was recorded for one minute. Baseline and addition of buffer were used as a negative control, whereas ATP was used as a positive control. The buffer was composed of 150 mM NaCl, 0.25 mM DTT, 0.1 mM PMSE, 25% glycerol.

## Data Analysis

We performed data analysis using Excel and MATLAB R2015a software. Frequency analysis of  $Ca^{2+}$  oscillations was performed using Per Uhlén's protocol from Spectral Analysis of Calcium Oscillations. (6) Statistical significance was assessed using a two-tailed Student's t-test ( $p < 0.05$ ).

## Results

To analyse collected data, we used the region of interest (ROI) tool in VoLocity software to select the cell of interest. Measurements from selected ROI were analysed and changes in  $[Ca^{2+}]_i$  were expressed as a ratio of Fura-2's fluorescent intensity when excited with 340 and 380 nm wavelength (340/380 ratios).  $[Ca^{2+}]_i$  oscillations were present at the baseline and after the buffer addition (Fig. 1), as well as after application of RANKL (Fig. 2). Addition of ATP caused a fast transient increase of  $[Ca^{2+}]_i$  in negative control cells, that recovered by the end of recording (Fig. 1C) and a

fast long-lasting increase of  $[Ca^{2+}]_i$  in RANKL stimulated cells that was observed over the entire time of recording (Fig. 2C). We computed average levels of  $[Ca^{2+}]_i$  for each cell at baseline and after addition of buffer or RANKL (Fig. 3A and C). No significant difference in the average  $[Ca^{2+}]_i$  was observed.

Since the frequency of oscillations appeared to change after addition of RANKL, we next performed frequency analysis using MATLAB R2015a software. Following Per Uhlén's protocol, (6) outliers were discarded. Cells that did not respond to ATP, and cells exhibiting aberrant responses to buffer or RANKL (such as single cells with a transient increase in  $[Ca^{2+}]_i$  on Fig. 1B) were excluded from further analysis. To obtain spectral analy-

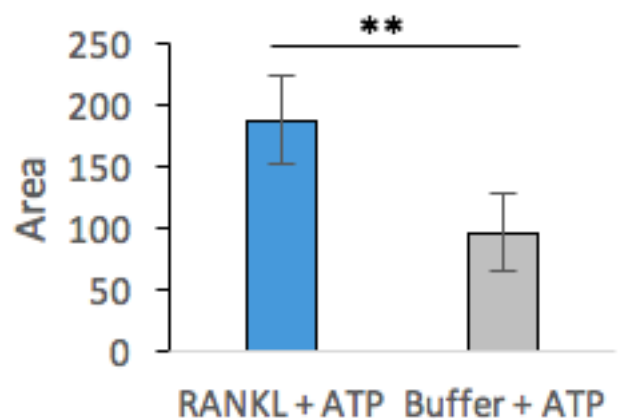


Fig. 5. Acute treatment with RANKL induced a change in a subsequent calcium responses to ATP. ATP responses following application of buffer (grey, same cells as presented on Fig. 1C) or RANKL (blue, same cells as presented on Fig. 2C) were analysed for the area under the calcium response curve. Data are means  $\pm$  SD, \*\* indicates  $p < 0.01$  examined by Student's t-test.

sis of  $[Ca^{2+}]_i$  oscillations, we applied a Hanning window function to previously acquired data to remove noise oscillation, and data was centered and analyzed using a fast Fourier Transform function. Results were displayed as a function of frequency to its relative strength (power) (Fig. 4A,B). Only the frequency of the dominant peak in the region of 20-50 mHz was chosen for analysis per single-cell measurement, as frequencies lower than 17 mHz (1/60 seconds of recording) are artifacts of the application of the Fourier Transform. Dominant peaks in the region between 20-50 mHz were 37.6 mHz for the baseline, 34.4 mHz for the buffer, and 37.7 mHz for RANKL (Fig. 4C). To compare frequencies, the average of their relative strength was analyzed. No significant difference was found between the strength of baseline and RANKL measurements. However, the Student's t-test showed significant difference in frequency strength between buffer and RANKL measurements ( $p < 0.05$ ) (Fig. 4D).

We have noticed that the response to ATP appears to differ in cells exposed to buffer and cells exposed to RANKL. We analysed the area under the curve of the fluorescence intensity ratio using MATLAB (Fig. 5). ATP-induced calcium responses had significantly larger area ( $p < 0.01$ ) in RANKL-stimulated cells than ATP-induced responses in the control group cells.

## Discussion

The objective of this study was to examine the changes in intracellular  $Ca^{2+}$  concentration upon stimulation of osteoclast precursors by RANKL. Using live cell fluorescence imaging we determined that acute application of RANKL did not affect the frequency of calcium oscillations in osteoclast precursors, but resulted in a more prominent appearance of oscillatory behaviour. Interestingly, we also found that short treatment with RANKL significantly affected the cell response to ATP, resulting in longer-lasting release of calcium compared to control cells.

Frequency analysis showed that both the control and experimental groups had calcium oscillations at similar frequencies and with similar values of major frequency peaks. In addition, average levels of calcium were not significantly different between the experimental groups. Although these data appear to contradict the known effect of RANKL in stimulating osteoclast calcium oscillations, it is important to take into account the experimental design of our studies. It has been previously shown that RANKL induces long-lasting  $Ca^{2+}$  oscillations that can last from 24 to 48 hours after RANKL stimulation in a primary cell culture. (7) In our study, we focused on late osteoclast precursors, which were formed from RAW 264.7 cells exposed to RANKL for 48 hours prior to imaging that were then cultured without RANKL for one hour prior to acute addition of RANKL. Nevertheless, we found that acute addition of RANKL allowed the cells to maintain more prominent oscillation compared to those observed after addition of buffer, suggesting that removal of RANKL may lead to a gradual decrease in calcium oscillations in osteoclast precursors. It is also possible that a relatively short recording time did not allow us to explore the whole range of changes induced in osteoclast precursors by acute exposure to RANKL.

We observed a significant difference in calcium response to ATP between the control and RANKL stimulated cells. In both control and RANKL-treated groups, ATP induced fast elevation of calcium that reached similar maximal levels. However, unlike the control group, in the cells that were stimulated by RANKL,  $[Ca^{2+}]_i$  never returned to basal level and continued to oscillate at a new higher level over the course of recording. This resulted in a significantly higher area under the curve of  $Ca^{2+}$  concentration response, indicative of a higher cumulative amount of  $Ca^{2+}$  available for downstream effects (Fig. 5). While the effects of acute treatment of osteoclast precursors by ATP on subsequent stimulation of osteoclastogenesis by RANKL have been previously described, to our knowledge this study is the first to report that short-term exposure to RANKL can change calcium response to a different mediator, such as ATP. (8) It can be hypothesized that long-lasting  $Ca^{2+}$  oscillations induced by RANKL interfere with the activity of plasma membrane or endoplasmic reticulum  $Ca^{2+}$  pumps, thus preventing effective calcium removal from the cytosol and resulting in a longer-duration response to ATP.

Further investigation is required to better understand the regulation of calcium oscillations induced by acute and long-term exposure to RANKL, as well as the implication of the differences in short term signaling for the physiological outcomes of osteoclast differentiation and function. Moreover, the potential role of RANKL-induced signaling on the calcium responses to other mediators, such as ATP, needs to be explored. Better understanding of osteoclast physiology will help in developing new diagnostic and therapeutic approaches in treating various bone diseases that are characterized by excessive osteoclastic bone resorption.

## Acknowledgements

I would like to express my gratitude to Dr. Gulzhakhan Sadvakassova and Dr. Svetlana Komarova for the opportunity to work on this project, for their assistance and guidance, and to Antonio Rosario for help with frequency analysis.

## References

1. Rodan G. Therapeutic Approaches to Bone Diseases. *Science*. 2000;289(5484):1508-1514.
2. Komarova S, Fong J. Breast Cancer Metastases to Bone: Role of the Microenvironment. In: Gunduz M, Gunduz E, ed. *Breast Cancer - Focusing Tumor Microenvironment, Stem cells and Metastasis*. 1st ed. InTech; 2011. p. 531-543.
3. Hwang S, Putney J. Calcium signaling in osteoclasts. *Biochimica et Biophysica Acta (BBA) - Molecular Cell Research*. 2011;1813(5):979-983.
4. Barreto-Chang O, Dolmetsch R. Calcium Imaging of Cortical Neurons using Fura-2 AM. *Journal of Visualized Experiments*. 2009;(23).
5. Yu H, Ferrier J. ATP Induces an Intracellular Calcium Pulse in Osteoclasts. *Biochemical and Biophysical Research Communications*. 1993;191(2):357-363.
6. Uhlen P. Spectral Analysis of Calcium Oscillations. *Science Signaling*. 2004;2004(258):pl15-pl15.
7. Takayanagi H, Kim S, Koga T, Nishina H, Isshiki M, Yoshida H et al. Induction and Activation of the Transcription Factor NFATc1 (NFAT2) Integrate RANKL Signaling in Terminal Differentiation of Osteoclasts. *Developmental Cell*. 2002;3(6):889-901.
8. Buckley K, Hipskind R, Gartland A, Bowler W, Gallagher J. Adenosine triphosphate stimulates human osteoclast activity via upregulation of osteoblast-expressed receptor activator of nuclear factor- $\kappa$ B ligand. *Bone*. 2002;31(5):582-590.

## Research Article

<sup>1</sup>Department of Anatomy & Cell Biology, McGill University, Montreal, QC, Canada

## Keywords

Eukaryotic Initiation Factor 4E, RNA interference, Knockdown, Knockout, Co-immunoprecipitation

## Abbreviations

|   |          |
|---|----------|
| Eukaryotic Initiation Factor 4E                           | eIF4E    |
| Eukaryotic Initiation Factor 4G                           | eIF4G    |
| Eukaryotic Initiation Factor 4A                           | eIF4A    |
| eIF4E Homologous Protein                                  | 4EHP     |
| Upstream Activation Sequence                              | UAS      |
| RNA interference  | RNAi     |
| Germline stem cell  | GSC      |
| Cyst stem cell  | CySC     |
| Individualization complex                                 | IC       |
| Knockdown   | KD       |
| Knockout  | KO       |
| Co-immunoprecipitation                                    | Co-IP    |
| Tris-buffered saline                                      | TBS      |
| Phosphate-buffered saline                                 | PBS      |
| Sodium dodecyl sulfate polyacrylamide gel electrophoresis | SDS PAGE |

## Email Correspondence

liang1712@gmail.com

Liang Chen<sup>1</sup>

# Loss-of-Function Analysis Elucidates Essential Roles of eIF4E Isoforms in *Drosophila* Spermatogenesis

## Abstract

**Background:** Through transcriptional and post-transcriptional regulation, eukaryotic cells can control gene expression to moderate vital cell processes and induce morphological changes. In developmental biology, translation initiation is emerging as a key player in gene expression regulation. Translation initiation begins when eukaryotic initiation factor 4E (eIF4E) binds the 5' mRNA cap to recruit other initiation factors. Eight eIF4E isoforms are present in *Drosophila melanogaster*. The canonical eIF4E-1 is involved in the translation of all genes and is a common target for translational regulation mechanisms. The activity of testis-specific eIF4Es in *Drosophila* are largely unclear, but recent evidence on eIF4E-3 suggests that the other isoforms may also possess distinct, essential functions in spermatogenesis.

**Methods:** Here we provide protein localization data and loss-of-function analysis to characterize eIF4E-4, eIF4E-5, and eIF4E-7.

**Results:** Single KD showed few phenotypes, while eIF4E-4/eIF4E-5 double knockdown males had severe defects in spermatogenesis. In eIF4E-5/eIF4E-7 double knockdowns, mutations manifested in multiple stages of severity.

**Conclusions:** The unique expression patterns and differential mutant phenotypes observed suggest that the testis-specific isoforms contain varying levels of functional redundancy. eIF4E-4 and eIF4E-5, which share close homology, appear to have overlapping roles in regulating germ cell division during early spermatogenesis. However, during spermatid individualization they seem to assume different functions. eIF4E-7 also appears to be involved in germ cell differentiation, but most likely in a separate mechanism due to the inability of other isoforms to compensate for its knockdown.

## Introduction

At the crux of many critical cellular processes is the formation, maintenance, and termination of protein localization patterns. With increasing knowledge on gene expression, post-transcriptional regulation is growing as a frontier in developmental biology. This is highlighted by the fact that while mRNA levels can remain stable, the rate of protein synthesis can vary drastically to affect gene expression. (1) Amongst post-transcriptional processes, eukaryotic initiation factor 4E appears to be a central target for regulation. Canonical translation initiation begins when the mRNA is bound at the 5' methylated cap by eukaryotic initiation factor 4E (eIF4E). (2) eIF4E then interacts with eIF4A and eIF4G to form the eIF4F complex, which binds other factors and eventually recruits the ribosome to the bound mRNA (Fig. 1A). (3) As a characterized proto-oncogene, eIF4E is the limiting factor to translation initiation (4) —exogenously increasing eIF4E protein levels will induce cells into an oncogenic state. (2) *Drosophila melanogaster* has eight eIF4E isoforms, and eIF4E-3, 4, 5, 7 are testis-specific (Fig. 1B). (5) All isoforms have been shown to have 5' cap binding at unequal affinities (Fig. 1C). (6) eIF4E-1 is the ubiquitous 5' cap binding protein involved in broad translation of all genes. eIF4E-3 is essential for meiosis during spermatogenesis, with knockouts (KO) forming multi-nucleated spermatocytes and sterile males. (7) Research on eIF4E homologous protein (4EHP) has revealed that it represses translation by sequestering mRNA from eIF4E-1 and preventing eIF4F formation. (8) The function of the other isotypes are largely unknown with only limited information about localization patterns.

The unique developmental properties of the *Drosophila* male germline make it an excellent model to investigate translational machinery. During post-meiotic stages, transcription is virtually non-existent due to the pro-

gressive condensation of germ cell chromatin. (9) Therefore, virtually all de novo protein production during spermatid morphogenesis is a result of translational control. Spermatogenesis begins in the apical tip of the testis and ends at the distal end (Fig. 2A). Somatic cyst stem cells (CySC) and germ-line stem cells (GSC) asymmetrically divide to produce a single spermatogonium that differentiates and undergoes four incomplete mitotic divisions to form 16 interconnected spermatocytes (Fig. 2B). (10) After growing and accumulating gene products to prepare for the oncoming transcriptional arrest, spermatocytes divide meiotically to yield 64 interconnected spermatids that enter spermiogenesis and execute synchronous morphological changes: organelle remodeling, chromatin condensation, cell polarization, elongation, waste bag formation, and individualization. (11) Towards late spermatogenesis, an individualization complex (IC) develops to push excess cytosolic material away from spermatid heads into visible waste bags at the tail terminus (Fig. 2C). (12) When spermiogenesis completes, sperm coil at the terminal epithelium and eject from the testis into seminal vesicles for storage. (13) The entire process takes 10 days, with spermiogenesis taking 5 days.

Here, we provide evidence implicating the vital roles of eIF4E-4, eIF4E-5, and eIF4E-7 in spermatogenesis. Mutants generated from gene-specific knockdowns reveal both unique and redundant functions between isoforms. With their 5' mRNA cap binding ability, eIF4E isotypes are likely able to selectively target populations of mRNAs for translation or repression. Preferential mRNA binding could dictate gene expression throughout the testis and especially during post-meiotic stages—when germ cells no longer produce new mRNA. We hypothesize that eIF4E-5 and eIF4E-7 are essential for male germ cell development, while eIF4E-4 shares functional redundancies with eIF4E-5.

## Materials & Methods

### Fly Stocks

Flies were raised in glass vials of standard medium as formulated by Bloomington Drosophila Stock Center (BDSC). Stocks were kept in 22°C and flies were crossed in 25°C. Flies were anesthetized and handled on CO<sub>2</sub> pads under a dissecting microscope. Oregon-R flies were used as wild-type controls. To induce gene knockdown, the UAS-GAL4 system was used. (14) Transgenic UAS fly lines express long hairpin RNAi under the control of an upstream activation sequence (UAS). These hairpin constructs are only transcribed when activated by exogenous GAL4 transcription factor, and these are present downstream of endogenous promoters in separate transgenic GAL4 driver lines. We crossed UAS-RNAi lines with a GAL4 driver lines to produce progeny with tissue-specific knockdowns (Fig. 3). (15) Both single and double knockdowns were created (Fig. 4, Fig. 5). The following UAS-RNAi lines from Vienna Drosophila Resource Center (VDRC) and the TRiP project (Harvard Medical School) were used: eIF4E-3 (BL# 42804), eIF4E-4 (VDRC#107595), eIF4E-5 (VDRC#102173), eIF4E-7 (VDRC#107958). The Bam-Gal4;VP16 (gift of M. Fuller) driver was used to express UAS constructs in the spermatogonium. Knockdowns were confirmed with western blot analysis (Fig. 6).

### Microscopy

Testes were dissected and prepared under live squash (16) and whole mount immunofluorescence protocols. For live squash prep, testes were dissected in testis buffer with 1.1µg/mL Hoescht 33342 (Invitrogen#62249) and then immediately mounted onto slides to image using the Leica DM6000B microscope. Images were taken 10 minutes after initial dissection to ensure samples maintained structural integrity. For immunofluorescence staining, testes were dissected in 0.3% PBS-Triton X-100, fixed in 4% paraformaldehyde for 15 min, permeabilized in 2% PBS-Triton X-100 for 1 hour, blocked in 0.3% PBS-Triton X-100- 1% albumin for 2 hours, and then probed with antibodies. Samples were probed with the following primary antibodies (raised by H. Han): rabbit anti-eIF4E-1 (1:500), rat anti-eIF4E-3 (1:500), rabbit anti-eIF4E-4 (1:400), and rat anti-eIF4E-5 (1:500). Additionally, rabbit anti-eIF4G (1:500), rabbit anti-eIF4G2 (1:200), mouse anti-Orb 4H8 (Developmental Studies Hybridoma Bank, 1:250), rat and rabbit anti-vasa (1:500), mouse anti- $\alpha$ -tubulin (Sigma #T6199, 1:10000), and mouse anti-adducin 1B1 (Developmental Studies Hybridoma Bank, 1:250) were probed as protein markers. The secondary antibodies used were: Goat anti-rabbit, anti-rat and anti-mouse antibodies conjugated with Alexa 488 or Alexa 555 (Life Technologies). DAPI (Invitrogen #D3571) was used at 10 µg/mL to stain DNA, and Alexa 555 phalloidin (Invitrogen#A34055) was used at 10 µg/mL to stain F-actin. Immunostaining sample images were taken using the Leica SP8 point-scanning confocal microscope, and the images were processed with Fiji software.

### Western Blot

To create protein lysate, testes were dissected in 0.3% PBS-Triton X-100, promptly flash frozen in liquid nitrogen, and mechanically lysed in lysing buffer containing 8M urea. 12% SDS PAGE was run, and separated proteins were transferred onto Polyvinylidene difluoride (PVDF) membrane. Blots were blocked in 5% milk for 1 hour and probed overnight with primary antibodies: rabbit anti-eIF4E-4 (1:500), rat anti-eIF4E-5 (1:500), and mouse anti- $\alpha$ -tubulin (1:20,000). After washing with 0.1% TBS-Tween 20, blots were probed for 2 hours with secondary antibodies conjugated to horseradish peroxidase. Using luminol and oxidizing reagent, bound secondary antibodies were visualized with x-ray film.

### Co-Immunoprecipitation (Co-IP)

Testes (~80) were dissected in PBS, lysed in 1 mL of lysis buffer (20 mM HEPES pH 7.5, 150 mM KCl, 4 mM MgCl<sub>2</sub>, 0.1% (v/v) NP-40, 0.5 mM DTT, 1x Halt protease inhibitor) and centrifuged at 13,000 x g for 10 min. 20 µl Protein G Dynabeads (Invitrogen) were incubated with rabbit eIF4E-1 (1:500) and rat eIF4E-5 (1:500) antibodies for 1 hour. The supernatant was then incubated with Dynabeads overnight on a rotator.

Subsequently, the beads were washed with lysis buffer 3 times for 20 min. The beads were then boiled in SDS sample buffer and the supernatant was used for SDS-PAGE analysis. For western blot, the primary antibodies were rabbit anti-eIF4E1 (1:500), rabbit anti-eIF4G2 (1:500), and rabbit anti-eIF4E-1 (1:1000). HRP-conjugated goat anti-rabbit (1:5000) and anti-rat (1:2500) antibodies (GE Healthcare) were used as secondary antibodies.

## Results

### Endogenous Expression of eIF4E isoforms in Drosophila Testes

Spermatogenesis begins at the apical tip, and germ cells migrate towards the distal end as they develop (Fig. 7). eIF4E-1 is present in the cytoplasm of both somatic cyst cells and germ cells during early spermatogenesis (Fig. 8). The protein, however, is notably absent in later germ cell stages and instead expresses in somatic cyst cells of spermatid bundles. (17) eIF4E-3 expression is restricted to the cytoplasm of primary spermatocytes, secondary spermatocytes, and early elongating spermatids; it is not localized in stem cells, spermatogonia, or mature spermatid bundles (Fig. 8). (7) eIF4E-4 is found in the cytoplasm of germ cells throughout spermatogenesis. It can be seen that in spermatid bundles, eIF4E-4 preferentially concentrates in the IC and individualized portions of the bundle (Fig. 9A). Interconnected spermatid regions have lower signal strength. eIF4E-5 is also expressed in all stages of germ cell development, including elongating spermatids that produce a ribboning pattern along the testis. The protein abundance increases in waste bags of mature spermatid bundles (Fig. 9A). eIF4E-7 expression patterns were not elucidated. To confirm expression patterns of eIF4E isoforms, antibody specificity was confirmed with western blot (Fig. 6) and immunostaining of knockdown testes (Fig. 9B).

### Protein Markers of Spermatogenesis

To analyze phenotypes from eIF4E isoform knockdowns, both cell morphology and protein markers of spermatogenesis were observed. The following protein markers were used: actin, tubulin, vasa, orb, adducin, eIF4G, and eIF4G2 (Fig. 10). In wild-type male flies, phalloidin stains the actin in the outer muscular sheath of the testis as well as the actin cones of the IC (Fig. 10A). (18)  $\alpha$ -tubulin is ubiquitously found in the testis, and in spermatids it highlights axonemes (Fig. 10B). (11) eIF4G has similar expression patterns as eIF4E-1, and is found in both the somatic cyst cells and germ cells during early stages, while primarily found in the cyst cells of later germ cells (Fig. 10C). (17) eIF4G2 is a germ-line specific protein (17) and is found in all germ cell stages of spermatogenesis; it concentrates in waste bags (Fig. 1D). Orb is found in the waste bags of individualized spermatid bundles (Fig. 10E). Adducin co-localizes with the fusomes of interconnected germ cells and appears as extensive branches amongst germ cell clusters (Fig. 10F). (20) Vasa is a germline specific protein that chiefly localizes in pre-meiotic germ cell stages (Fig. 10G). (21)

### Loss-of-function Analysis of eIF4Es

eIF4E-3 KD flies served as a positive control to test the efficacy of KD mutant generation, and wild-type flies were used as the negative control. eIF4E-3 mutants displayed previously reported phenotypes of male-sterility, multi-nucleated spermatocytes, de-localized nuclei in spermatids, and abnormal orb expression (Fig. 11). (17) eIF4E-4 KD males only showed aberrations towards the distal testis, where coiled spermatids accumulated (Fig. 12). eIF4E-5 KD produced tightly coiled sperm, numerous abnormal cystic bulges, and fewer IC that traveled the entire length of the bundle (Fig. 13).

eIF4E-7 KD males with one UAS-RNAi chromosome driven by Bam-Gal4;VP16 did not display any phenotypes, but after aging males for 4 weeks cells in testes began to over-proliferate and fail to develop into mature sperm. In wild type males, cell proliferation slows as stem cells take longer to divide and differentiate. (22) Males with 2 chromosomes of UAS-RNAi and drivers showed visible phenotypes after only 1-2 weeks of aging. Similarly, these testes were filled with small cells and spermatogenesis was arrested (Fig. 14). Adducin staining showed that only rudimentary fusomes formed in these mutants, indicating these cells did not maintain

connections with each other (Fig. 14)

### Double Knockdowns

Although single KD showed few phenotypes, eIF4E-4/eIF4E-5 double knockdown males had severe defects in spermatogenesis. After aging for one week, germ cell development ceased and distal testes contained coiled sperm. Normally, wild type testes show dense concentration of nuclei at the apical tip, but in these double knockdown mutants high concentrations of small cells were found throughout testis (Fig. 14). As a result of these abnormalities, testes lacking orb expression in waste bags show no IC complexes, and have abnormal eIF4G-2 and  $\alpha$ -tubulin localization (Fig. 15).

In eIF4E-5/eIF4E-7 double knockdowns, mutations manifested in multiple stages of severity. The least affected testes appeared like wild-type with the entire process of spermatogenesis intact. At the onset of mutation, testes began to show signs of abnormal cyst formation, with problems in differentiation and mitotic division appearing. Through vasa and adducin staining, spermatocytes are seen to occupy only a small portion of the testis (Fig. 16). In the most severe cases, testes were filled with small undifferentiated cells. These mutants lacked orb staining in spermatid waste bags, and instead stained coiled sperm at the distal end (Fig. 16).

## Discussion

During germline development, many key cellular processes rely on post-transcriptional gene regulation to establish protein gradients and gene expression patterns. Research across several model organisms point towards translation initiation, namely eIF4E cap binding activity, as a critical stage for post-transcriptional regulation. In *Drosophila*, several control mechanisms target eIF4E. Suppressing translation, eIF4E binding proteins (eIF4E-BP) directly latch onto eIF4E to inactivate it. (23) Repressing translation of specific genes, Bicoid (*bcd*) binds to 3'UTR of Caudal mRNA and recruits 4EHP, a cap-binding protein that is unable to initiate translation, to effectively prevent Caudal protein formation. (8) Recently, eIF4E isoform-mediated translation has been implicated as an alternative way to modulate gene expression. It is important to note that eIF4E-3, eIF4E-4, eIF4E-5, and eIF4E-7 have all been reported to bind eIF4G at varying affinities. (6) This suggests that these male germ-line specific proteins are all able to form the eIF4F complex and initiate translation. However, since only one type of 5' mRNA cap is present in *Drosophila*, eIF4E isoforms would require intermediate proteins like *bcd* to selectively repress or promote translation of specific proteins.

Previous characterizations of eIF4E isoforms have shown that evolutionary conservation between these paralogs differs (Fig. 1B). (6) Amongst the isoforms, eIF4E-4 and eIF4E-5 share the greatest homology. When analyzing single KD's of eIF4E-4 and eIF4E-5, few defects were seen. Spermatogenesis proceeded normally in the mutants up until individualization, during which KD's began to induce mutations. Both eIF4E-4 and eIF4E-5 KD cause sperm to coil at the end of spermatogenesis. Coiling, a morphological deformity, indicates that the mutant sperm are defective and blocked from passing into the seminal vesicle. (13) From observing eIF4E-4/eIF4E-5 double KD, we conclude that the two isoforms share functional redundancies. In stark contrast to single KD, the double KD shuts down spermatogenesis, stimulates uncontrolled cell division, and blocks germ cell differentiation. From immunostaining, eIF4E-4 and eIF4E-5 are seen to co-localize in pre-meiotic cell stages (Fig. 8). This co-localization may explain how the isoforms are able to compensate for the absence of the other in early development. In post-meiotic stages, eIF4E-4 primarily localizes in individuated segments of spermatid bundles while eIF4E-5 is present in all portions of the bundle, including the waste bag. Furthermore, the previously reported reduced fertility of eIF4E-5 may also be explained by these expression patterns: while eIF4E-5 would be able to largely compensate for any absent eIF4E-4 due to the fact that it is ubiquitously present in germ cells, eIF4E-4's absence in non-individuated bundles could contribute to greater cell defects.

From KD analysis, eIF4E-7 seems to be mainly involved in pre-meiotic

germ cell development. These mutants contained a surplus of cells varying in size. Wild type testes usually slow down their rate of stem cell replication and differentiation. (22) While this is likely due to increased production of RNAi, protein and RNA quantification methods need to be performed for confirmation. The phenotypes observed in eIF4E-5 and eIF4E-7 double knockdown are severe, but further analysis is required to determine whether the defects present are merely from eIF4E-7 KD or if they are the result of the KD of both proteins. Therefore it is currently unknown whether eIF4E-7 shares functions with eIF4E-5. Observing eIF4E phylogeny would suggest they do not share functions, as eIF4E-7 has low conservation with other eIF4E isoforms and is almost twice as large as the other eIF4Es.

eIF4E itself is known to be a proto-oncogene (24), and reports have shown that exogenously increasing eIF4E cellular levels can transform cells into tumorous cells. (25) The three eIF4E isoforms observed seem to be involved in cell differentiation and proliferation. Because eIF4E is the rate limiting protein in translation initiation, manipulating native concentrations of this protein can have wide effects on cell metabolism and growth. (3) Over-proliferation can be due to malfunctions in spermatogonial differentiation into spermatocytes or from eliminating the stem cell niche of GSC and CySC through some form of retrograde signaling.

To elucidate the separate functions of the male testis-specific isoforms, Co-IP will be optimized to reveal protein interactions and RNA interactions. This will determine if each isoform forms a preinitiation complex and promotes translation. Previous studies in eIF4E interactions were performed in a Yeast two Hybrid screen, which are known to produce false positives when testing protein interaction. Additionally, performing Co-IP followed by RNA sequencing would elucidate whether isoforms have preferences in binding distinct populations of mRNA. Additionally, knockout (KO) flies can be generated to observe if phenotypes worsen. Since these proteins are overwhelmingly localized in the testis, KO lines should have no effect on the other physiological processes within the fly. Some controls also need to be performed to confirm the phenotypes we observed in the KD flies. RT-PCR and western should be performed on both single knockdowns and double knockdowns. eIF4E-7 localization patterns need to be elucidated. The antibodies raised against this protein that we have is non-specific, so new antibodies raised against a separate peptide of the protein should be created to further characterize this protein. Lastly, mutants should be probed with additional sets of protein markers to discover which molecular mechanisms are disrupted.

## Conclusion

Based on distinct localization patterns, variable knockdown phenotypes, and documented protein interactions, we conclude that eIF4E isoforms have essential roles in spermatogenesis. eIF4E-4 and eIF4E-5 are functionally redundant in pre-meiotic sperm development, while they contain separate functions in post-meiotic development. eIF4E-7 is distinct from all other testis specific isoforms and is involved in cell differentiation, proliferation, and stem cell niche maintenance. Characterizations of eIF4E-4, eIF4E-5, and eIF4E-7 contributes to the growing collective knowledge on eIF4E isoform function. Their unique localization patterns and distinct, vital roles indicate that the isoforms are key players in post-transcriptional regulation.

## References

1. Jackson R, Hellen C, Pestova T. The mechanism of eukaryotic translation initiation and principles of its regulation. *Nature Reviews Molecular Cell Biology*. 2010;11(2):113-127.
2. Mamane Y, Petroulakis E, Rong L, Yoshida K, Ler L, Sonenberg N. eIF4E  $\hat{a}$ € from translation to transformation. *Oncogene*. 2004;23(18):3172-3179.
3. Pelletier J, Graff J, Ruggero D, Sonenberg N. Targeting the eIF4F Translation Initiation Complex: A Critical Nexus for Cancer Development. *Cancer Research*. 2015;75(2):250-263.
4. Richter J, Sonenberg N. Regulation of cap-dependent translation by eIF4E inhibitory proteins. *Nature*. 2005;433(7025):477-480.
5. Chintapalli V, Wang J, Dow J. Using FlyAtlas to identify better *Drosophila*

melanogaster models of human disease. *Nature Genetics*. 2007;39(6):715-720.

6. Hernandez G, Altmann M, Sierra J, Urlaub H, Diez del Corral R, Schwartz P et al. Functional analysis of seven genes encoding eight translation initiation factor 4E (eIF4E) isoforms in *Drosophila*. *Mechanisms of Development*. 2005;122(4):529-543.
7. Hernandez G, Han H, Gandin V, Fabian L, Ferreira T, Zuberek J et al. Eukaryotic initiation factor 4E-3 is essential for meiotic chromosome segregation, cytokinesis and male fertility in *Drosophila*. *Development*. 2012;139(17):3211-3220.
8. Cho P, Poulin F, Cho-Park Y, Cho-Park I, Chicoine J, Lasko P et al. A New Paradigm for Translational Control: Inhibition via 5' cap mRNA Tethering by Bicoid and the eIF4E Cognate 4EHP. *Cell*. 2005;121(3):411-423.
9. White-Cooper H, Caporilli S. Transcriptional and post-transcriptional regulation of *Drosophila* germline stem cells and their differentiating progeny. *Adv Exp Med Biol* 786. 2013;:47-61.
10. de Cuevas M, Matunis E. The stem cell niche: lessons from the *Drosophila* testis. *Development*. 2011;138(14):2861-2869.
11. Fabian L, Brill J. *Drosophila* spermiogenesis. *Spermatogenesis*. 2012;2(3):197-212.
12. Sartain C, Wolfner M. The spermatid individualization complex of *Drosophila melanogaster*. *Mol Reprod Dev*. 2012;79(6):367-367.
13. Tokuyasu K, Peacock W, Hardy R. Dynamics of spermiogenesis in *Drosophila melanogaster*. *Zellforsch*. 1972;127(4):492-525.
14. Dietzl G, Chen D, Schnorrer F, Su K, Barinova Y, Fellner M et al. A genome-wide transgenic RNAi library for conditional gene inactivation in *Drosophila*. *Nature*. 2007;448(7150):151-156.
15. del Valle Rodríguez A, Didiano D, Desplan C. Power tools for gene expression and clonal analysis in *Drosophila*. *Nature Methods*. 2011;9(1):47-55.
16. Bonaccorsi S, Giansanti M, Cenci G, Gatti M. Preparation of Live Testis Squashes in *Drosophila*. *Cold Spring Harbor Protocols*. 2011;2011(3):prot5577.
17. Ghosh S, Lasko P. Loss-of-Function Analysis Reveals Distinct Requirements of the Translation Initiation Factors eIF4E, eIF4E-3, eIF4G and eIF4G2 in *Drosophila* Spermatogenesis. *PLoS ONE*. 2015;10(4):e0122519.
18. Noguchi T, Lenartowska M, Rogat A, Frank D, Miller K. Proper Cellular Reorganization during *Drosophila* Spermatid Individualization Depends on Actin Structures Composed of Two Domains, Bundles and Meshwork, That Are Differentially Regulated and Have Different Functions. *Molecular Biology of the Cell*. 2008;19(6):2363-2372.
19. Xu S, Hafer N, Agunwamba B, Schedl P. The CPEB Protein Orb2 Has Multiple Functions during Spermatogenesis in *Drosophila melanogaster*. *PLoS Genetics*. 2012;8(11):e1003079.
20. Grieder N, de Cuevas M, Spradling A. The fusome organizes the microtubule network during oocyte differentiation in *Drosophila*. *Development*. 2000;127(18):4253-4264.
21. Sano H, Nakamura A, Kobayashi S. Identification of a transcriptional regulatory region for germline-specific expression of *vasa* gene in *Drosophila melanogaster*. *Mechanisms of Development*. 2002;112(1-2):129-139.
22. Boyle M, Wong C, Rocha M, Jones D. Decline in Self-Renewal Factors Contributes to Aging of the Stem Cell Niche in the *Drosophila* Testis. *Cell Stem Cell*. 2007;1(4):470-478.
23. Gingras A. Hierarchical phosphorylation of the translation inhibitor 4E-BP1. *Genes Dev*. 2001;15(14):2852-2864.
24. Carroll M, Borden K. The Oncogene eIF4E: Using Biochemical Insights to Target Cancer. *Journal of Interferon & Cytokine Research*. 2013;33(5):227-238.
25. Lazaris-Karatzas A, Sonenberg N. The mRNA 5' cap-binding protein, eIF-4E, cooperates with v-myc or E1A in the transformation of primary rodent fibroblasts. *Molecular and Cellular Biology*. 1992;12(3):1234-1238.

## Images

The images referenced in this article are presented here. Note that the images are *not* chronologically ordered. Visit [msurj.mcgill.ca](http://msurj.mcgill.ca) for clearer referenced images.

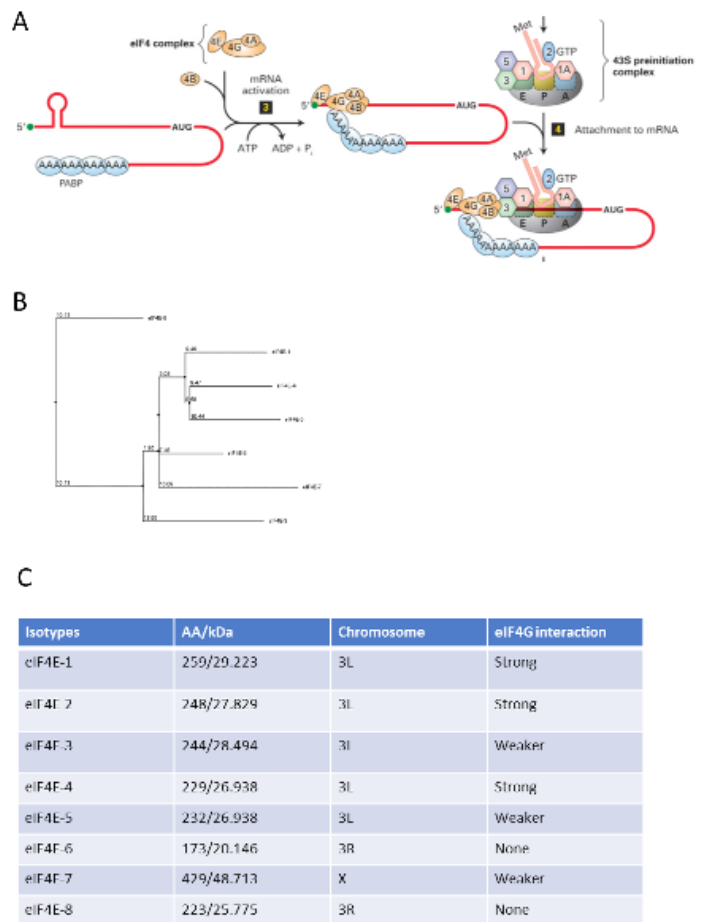


Fig. 1. eIF4E. (A) eIF4E binds to the 5' methyl cap. It then recruits eIF4G that binds eIF4a to form the eIF4F complex and associate with PABP to circularize the mRNA. Afterwards the 43S ribosomal subunit binds to the mRNA. (Molecular cell biology. (Macmillan, 2008)). (B) eIF4E-4 and eIF4E-5 share close homology. (C) eIF4E isoforms are present on the 3rd chromosome. Out of these, eIF4E-6 and eIF4E-8 do not interact with eIF4G.

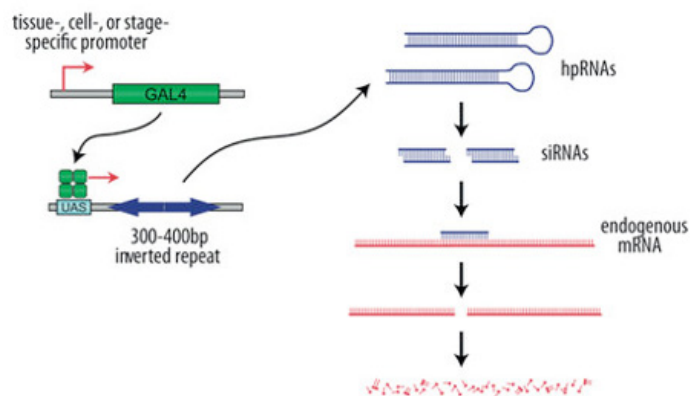


Fig. 3. GAL4/UAS-RNAi System. An endogenous tissue-specific promoter activates GAL4 expression to subsequently bind the UAS promoter and transcribe a ~300 base pair inverted repeat that is complementary to a specific gene. After transcription the RNA forms a hairpin RNA that is processed by Dicer 1 to form small interfering RNA that is recruited and used by RISC to degrade specific mRNAs.

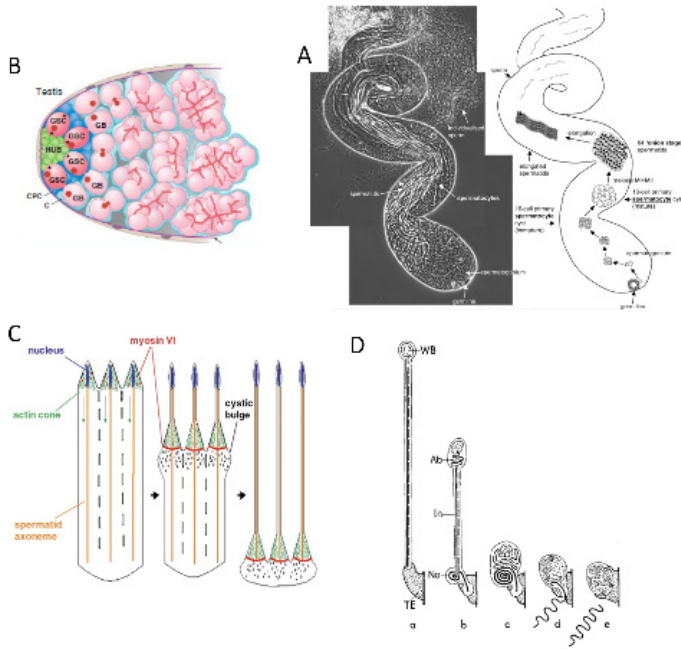


Fig. 2. Spermatogenesis. (A) Spermatogenesis begins at the apical tip where GSC and CySC divide and differentiate. As the cyst develops, it migrates towards the distal end of the testis. Spermatid polarity is maintained with heads facing the distal testis and tails pointing to the apical testis. (B) Fusome develops to interconnect spermatocytes and early spermatids. In spermatogonia, undeveloped fusomes are present as round clusters. (C) Individualization complex (IC) is composed of actin cones and myosin VI that migrates down the spermatid axoneme to individualize sperm and push excess cytosolic content to the tail end, forming waste bags. (D) Only healthy sperm eject from the bundle and eject into the seminal vesicle. Deformed sperm coil into the waste bag, awaiting autophagy.

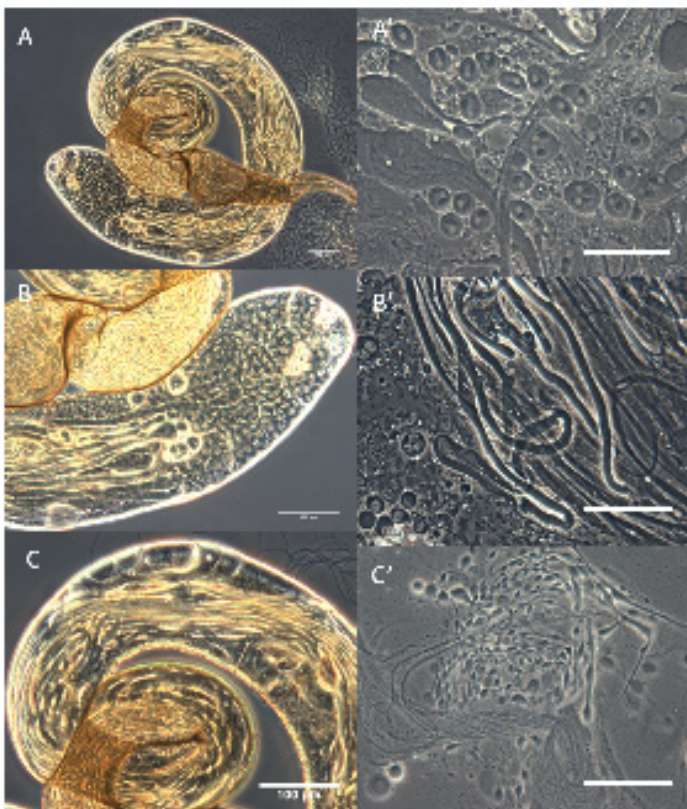


Fig. 7. Wild-type phase contrast testis. (A) Phase contrast image of a wild-type testis. (B) Apical tip can be seen containing CySC, GSC, spermatogonia, and spermatocyte cysts. (C) Distal end shows mature spermatid bundles ready for ejection into the seminal vesicle. (A') Secondary spermatocytes containing dark nebenkern paired with light nuclei. (B') Elongating spermatids that have not yet undergone individualization. (C') Individualized sperm with cystic bulges and waste bags. \*Scale bar 100  $\mu$ m (n=50)

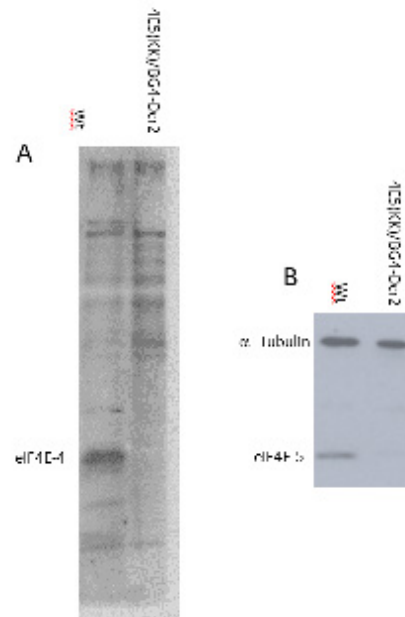


Fig. 6. Knockdown Confirmation. (A) eIF4E-4 is successfully knocked down. The rabbit anti-eIF4E-4 antibody binds non-specifically, and these extraneous bands served as loading controls. (B) eIF4E-5 is knocked down successfully with rat anti-eIF4E-5 antibody. Almost no non-specific bands were bound.

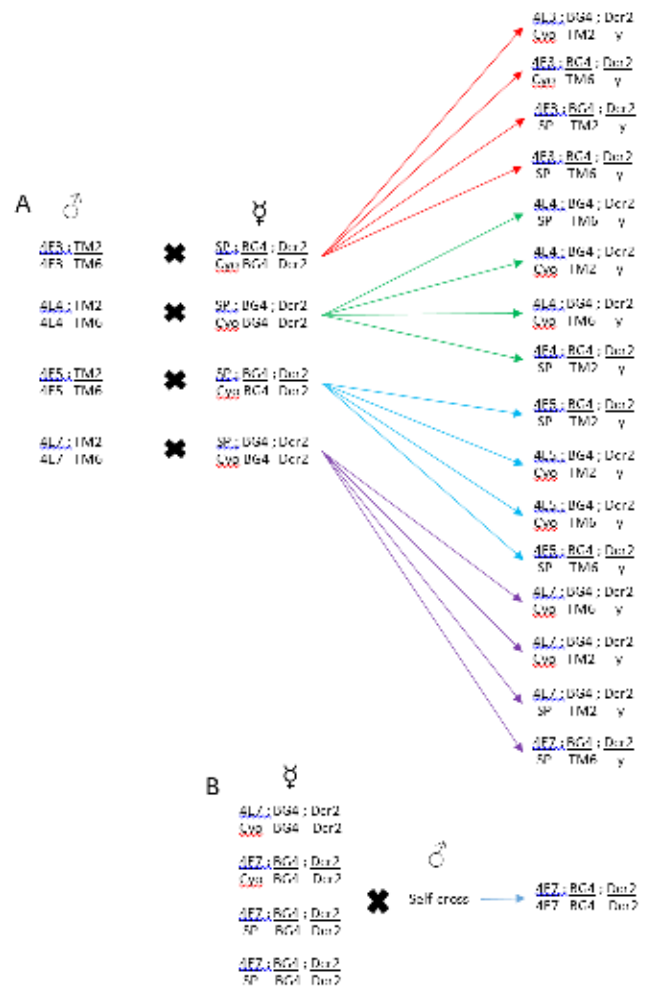


Fig. 4. Single KD Crossing. (A) A single cross was performed to generate single KD crossing. (B) 4E7;BG4;Dcr2 KDs were formed from self-crossing eIF4E-7 single KDs. eIF4E-7 KD males were fertile so crossings were not problematic.

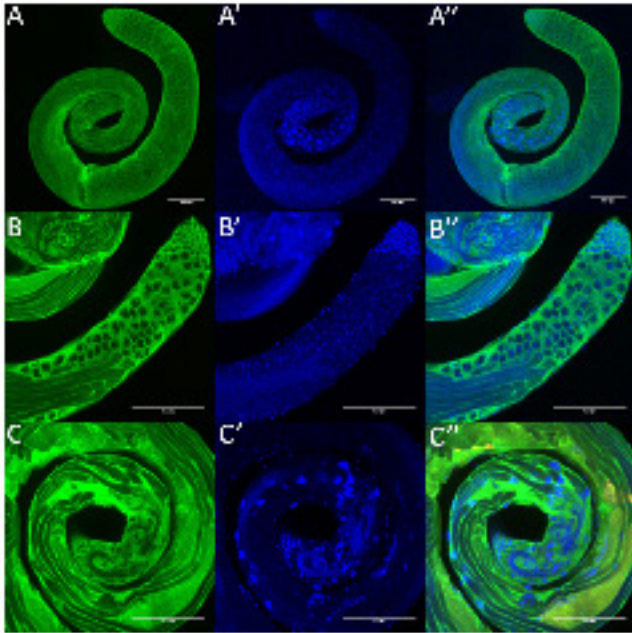


Fig. 8. eIF4E-1 and eIF4E-3 Expression. (A,A') eIF4E-1 stains both somatic cyst cells and germ cells during early spermatogenesis. (B,B') Spermatogonia and spermatocytes contain eIF4E-1 in the cytosol. DAPI staining concentrates at this apical tip. (C,C') eIF4E-1 is only present in somatic cyst cells that surround spermatid bundles during late stage spermatogenesis. DAPI stains clustered nuclei at the heads of spermatids. (D) eIF4E-3 stains germ cells that have not completed meiosis. (E) eIF4E-3 is present in the cytosol of spermatocytes but not in spermatogonia or GSC. (F) eIF4E-3 is seen in early elongating spermatids but becomes absent in subsequent developmental stages.  
\*Scale bar 100  $\mu$ m (n=40)

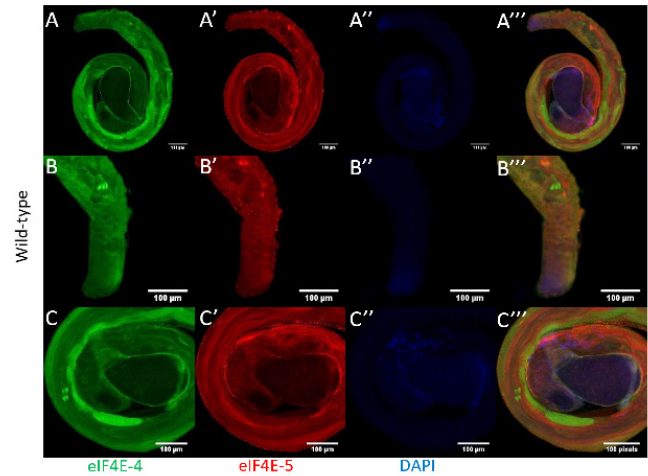


Fig. 9A. eIF4E-4 and eIF4E-5 localization. (A,B,C) eIF4E-4 localizes in germ cells, IC, and post-individualized germ cells. (A',B',C') eIF4E-5 expresses in all germ cells, with increased signal in spermatid bundles and terminal spermatid tails. \*Scale bar 100  $\mu$ m (n=10)

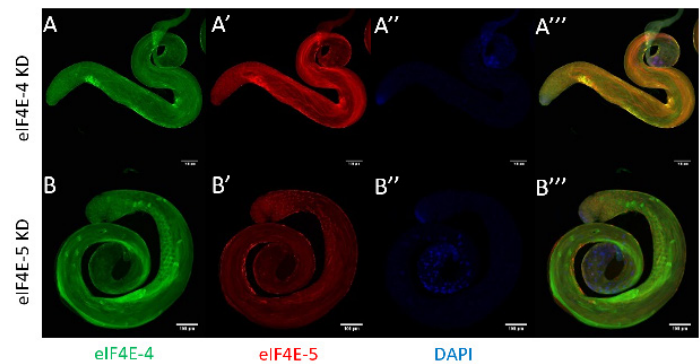


Fig. 9B. eIF4E-4 Antibody confirmation. (A) eIF4E-4 staining is absent in this KD testis. (A') eIF4E-5 staining is unaffected by eIF4E-4 KD. (B) eIF4E-4 staining is unaffected by eIF4E-5 KD, indicating specificity of respective primary antibodies and KDs. (B') eIF4E-5 KD removes eIF4E-5 staining in spermatid bundles. (B'') DAPI in the distal testis shows nuclei remain tightly clustered  
\*Scale bar 100  $\mu$ m (n=10)

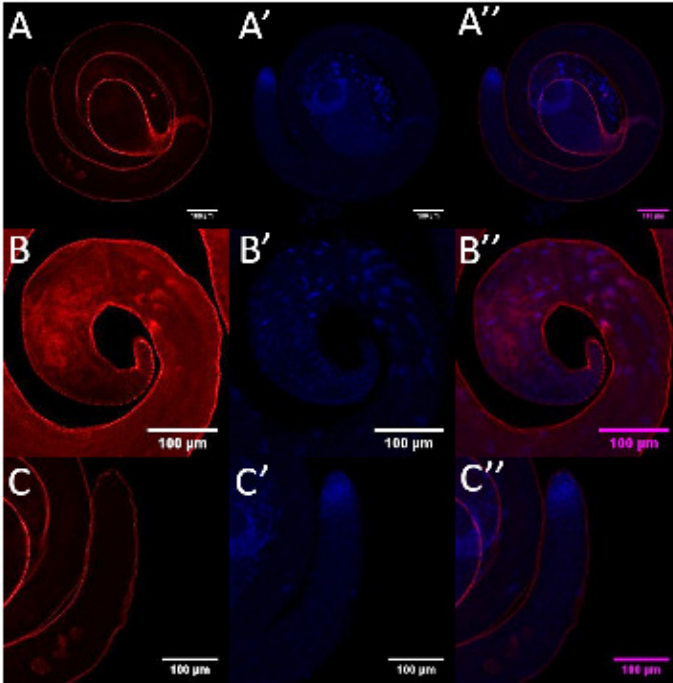


Fig. 10A. Actin localization in testes. The IC is assembled near the distal end (B) and travels down the spermatid towards the tail in the apical end (C)  
\*Scale bar 100  $\mu$ m (n=30)

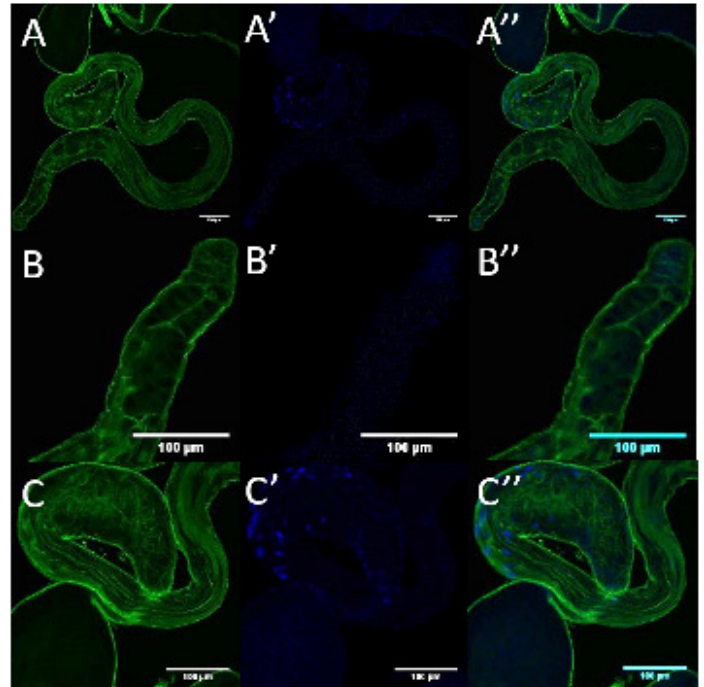


Fig. 10B. A-tubulin localization in testes. a-tubulin is ubiquitously expressed but shows preference for the axoneme (C) and cyst cells (B).  
\*Scale bar 100  $\mu$ m (n=30)

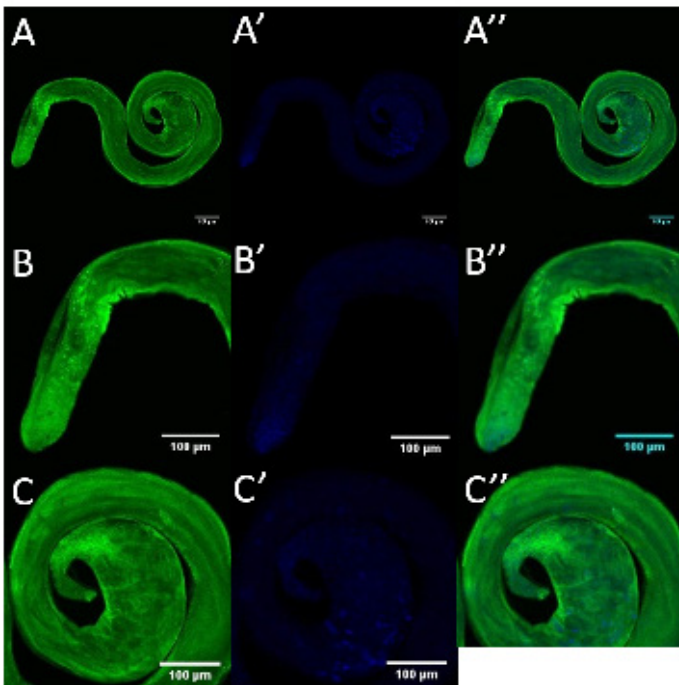


Fig. 10C. eIF4G localization in testes. eIF4G is present in both cyst cells and germ cells at the apical end (B), but only in cyst cells at the distal end (C)  
\*Scale bar 100  $\mu$ m (n=30)

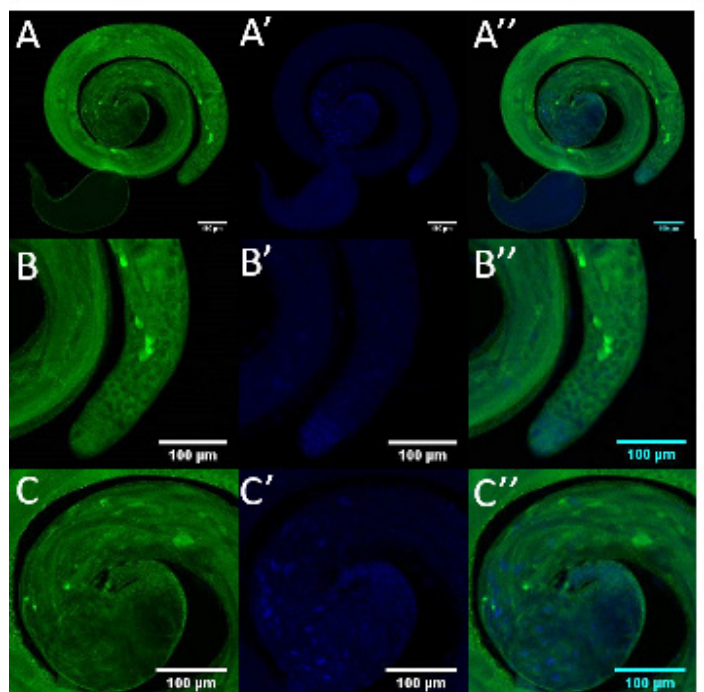


Fig. 10D. eIF4G-2 localization in testes. eIF4G-2 localizes in all germ cells, and shows increased concentration in the terminal ends of spermatid tails (B)  
\*Scale bar 100  $\mu$ m (n=30)

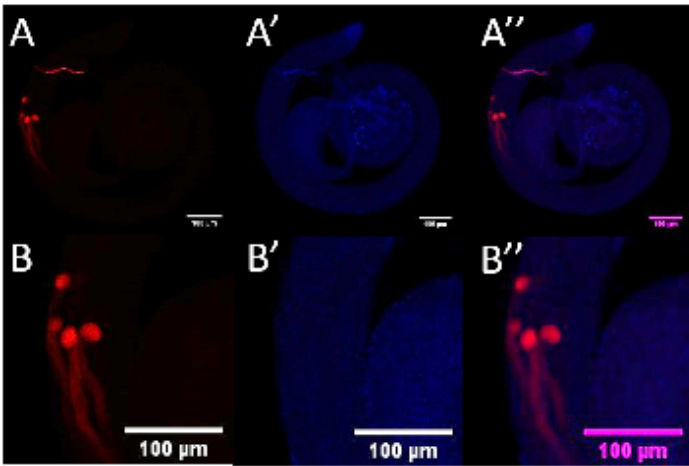


Fig. 10E. Orb localization in testes. Orb exclusively stains the terminal tails of individualized sperm bundles. They collect in the waste bags (B)  
\*Scale bar 100 μm (n=30)

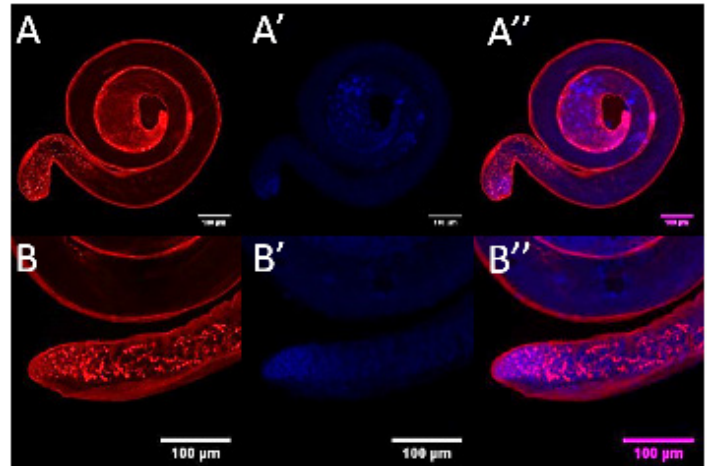


Fig. 10F. Adducin localization in testes. Adducin co-localizes with the fusome, a structure mainly present in pre-meiotic germ cells. This organ maintains interconnections between cell clusters (B) to ensure synchronous development  
\*Scale bar 100 μm (n=30)

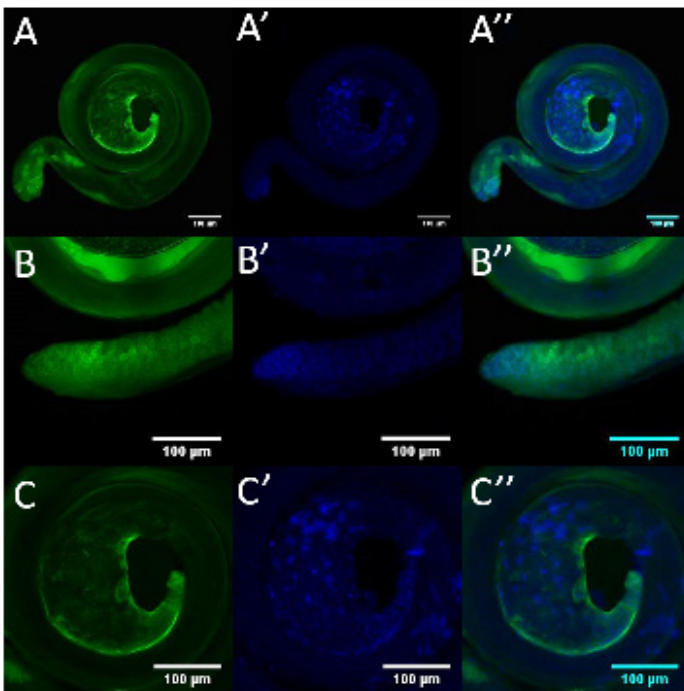


Fig. 10G. Vasa localization in testes. Vasa is a germ-line specific protein that primarily localizes in GSC, spermatogonia, and spermatocytes.  
\*Scale bar 100 μm (n=30)

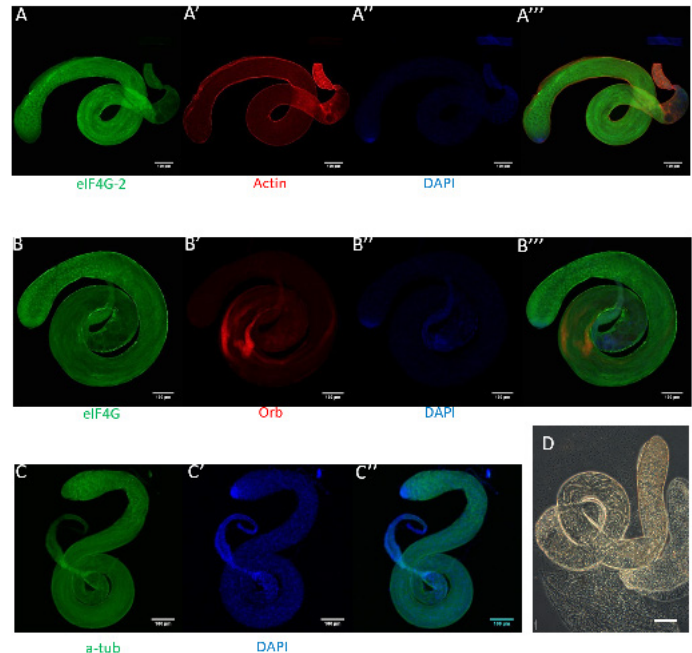


Fig. 11. eIF4E-3 KD. (A) eIF4G-2 distribution in germ cells is normal. (A') Individualization complexes are not present. (A'') Apical DAPI staining remains normal, but subsequent stages show nuclei dispersed along spermatid tails and lack clustered needle nuclei. (B) eIF4G expression is normal. (B') Orb is mislocalized and does not concentrate in waste bags. (C) a-tubulin is ubiquitously expressed and shows axoneme formation. (D) No mature sperm are formed. Spermatocytes contain multiple nuclei per cell.  
\*Scale bar 100 μm (n=40)

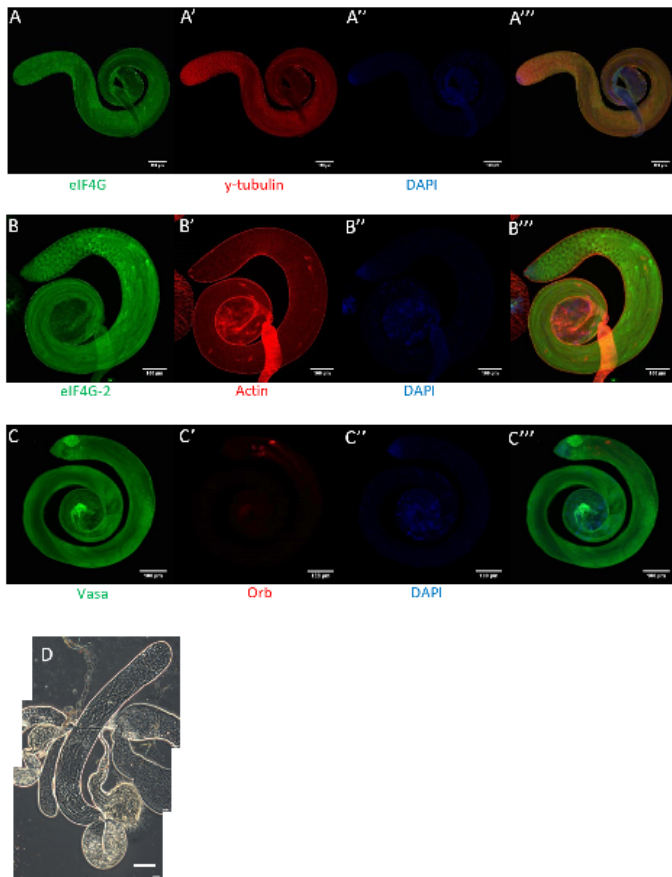


Fig. 12. eIF4E-4 KD. (A,A') eIF4G distribution is undisturbed. (B) eIF4G-2 expression remains the same, with extra signal in terminal spermatid tails. (B') Actin stains IC seen traveling down spermatid bundles. (C) Vasa stains spermatocytes, spermatogonia, and GSC. (C') Orb formation occurs normally in waste bags. (D) Coiled sperm are seen at distal end  
\*Scale bar 100  $\mu$ m (n=40)

Fig. 14. eIF4E-7;BG4;Dcr2 Single KD. (A,B) Vasa continues to stain early germ cell stages, but it can be seen that cell division of these cells occurs with errors. (B) shows that vasa is strikingly absent in these spermatogonia. In (A), cyst formation has ceased and cells no longer form clusters. (A') Adducin shows the fusome is underdeveloped and present throughout the testis, showing that these cells are undifferentiated. (B) shows normal fusome branching, indicating that early germ cells maintain interconnections in some mutants. (C,D) eIF4G-2 appears to have decreased levels in stages before secondary spermatocytes. (C,D') orb staining here is altered. The protein is dispersed and is seen to localize in the middle segment of some spermatids. Distribution is not solely in waste bags. (E) Testis is filled with undifferentiated germ cells. No spermatids are seen  
\*Scale bar 100  $\mu$ m (n=20, 11/20 exhibit phenotypes)

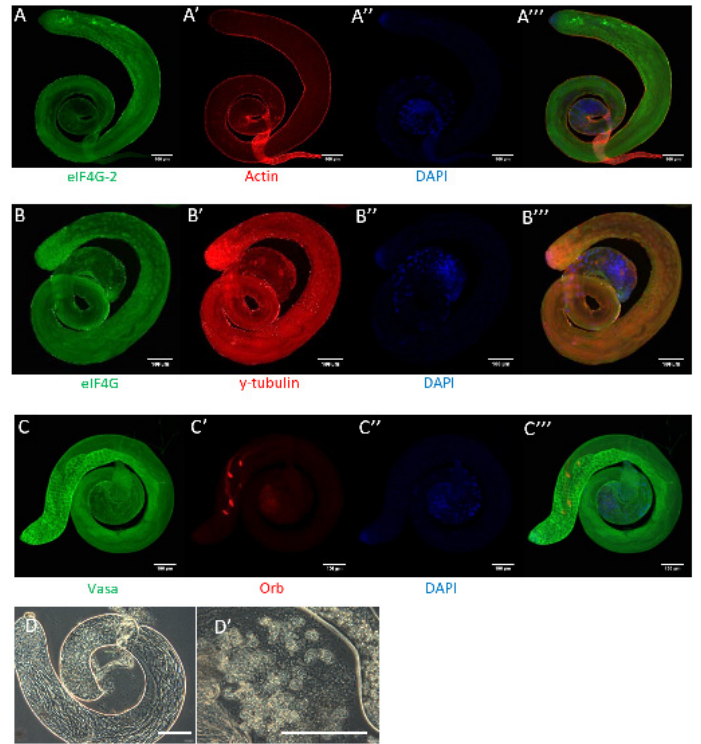
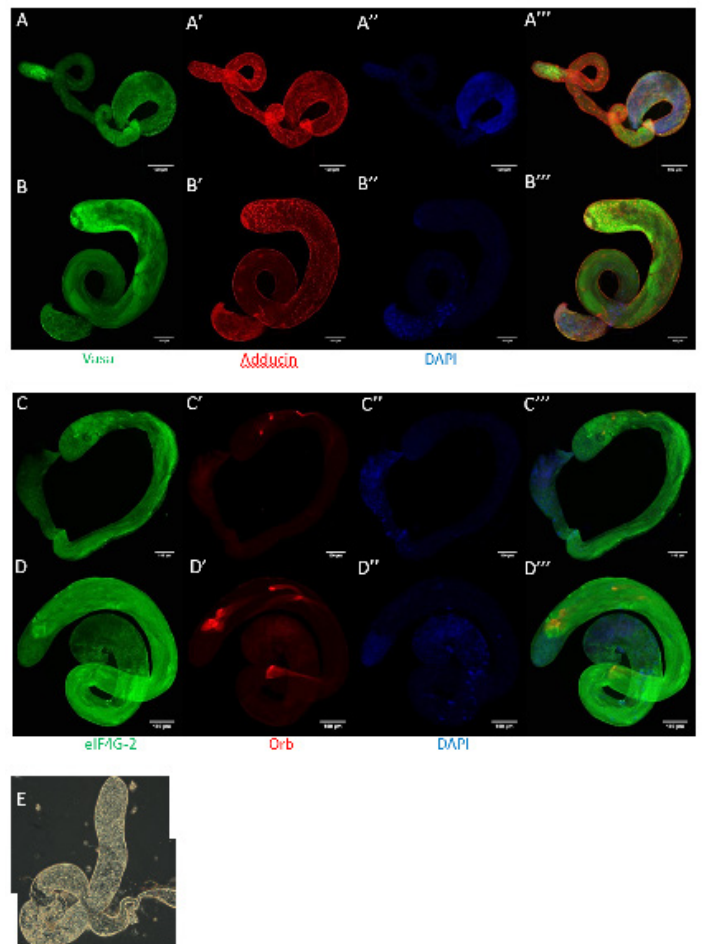


Fig. 13. eIF4E-5 KD. (A) eIF4G-2 expression appears normal. (A') IC are seen in the distal end of the testis but is absent from the apical tip. (B) eIF4G is expressed in germ cells in spermatocytes, but localizes in cyst cells afterwards, as is seen in wildtype (B')  $\gamma$ -tubulin is found ubiquitously in the testis and normally distributed. (C) Vasa is seen primarily staining GSC, spermatogonia, spermatocytes, and early spermatids. (C') Orb formation at the tails of spermatids highlights wastebags. (D) Germ cell development is altered at the distal tip. Abnormal spermatids collect here. (D') Mutant coiled sperm are shown here. They are isolated within cyst cells  
\*Scale bar 100  $\mu$ m (n=50)





Alistair Barton<sup>1</sup>, Ling Lin<sup>1</sup>, Shoma Yamanouchi<sup>1</sup>

# Cosmic Strings and The Origins of Globular Clusters

## Abstract

**Background:** Globular clusters are galactic structures whose origin is not well understood. In this paper we propose that their origin may be found in the accretions formed around cosmic string loops.

**Methods:** To test this hypothesis we derived the mass distribution that would be associated with the accretions and compared it to the observed mass distribution of globular clusters in our galaxy. Our derived distribution left us one free parameter (cosmic string tension) which we varied to optimize the fit. Once optimized, we compared the shape of the distribution and the number density that our model predicted with empirical observations. Later, we derived how velocity effects would alter the shape of this distribution.

**Results:** We achieved significant agreement between our model and observed values. Furthermore, the optimal tension corresponds to particle physics theories that have not been ruled out. Our analysis further suggests that globular clusters form around slowly moving (< 3% the speed of light) cosmic string loops; any model with significantly faster cosmic string loops would contradict our hypothesis.

**Limitations:** Our results were obtained by using numerous approximations (such as the Zel'dovich approximation) and thus should be treated as an order of magnitude estimation. Our data was also limited to observed globular clusters within the Milky Way, limiting our sample size to approximately 120 globular clusters.

**Conclusions:** We managed to obtain strong agreement between our model and observed globular clusters, suggesting that they may be seeded by cosmic string loops. This also serves to explain many other characteristics of globular clusters, such as age, density and location. The analyses used in this report can also be used when considering the formation of other accretion objects, such as ultra-compact-minihalos.

## Background

### Inflationary Cosmology

The main focus of cosmology is the study of the Universe on the largest of scales. In the inflationary model, the Universe expanded exponentially after the Big Bang. This exponential growth era is known as the inflationary epoch, and lasted from  $10^{-36}$  seconds to  $10^{-32}$  seconds after the Big Bang, after which the Universe continued to grow, but at a less accelerated rate. It is important to note that “growth” here signifies a stretching of space in all directions at all points.

Following inflation were the successive radiation-dominated and matter-dominated eras. The transition time between the two, or the time of equal matter and radiation, is denoted  $t_{eq}$ . Fig. 1 shows the timeline of the Universe, and how it evolved over time. Before  $t_{eq}$ , much of the energy in the Universe was in the form of radiation, dominating the Universe in a state of disorder and preventing electrons from being captured by nuclei. It is only after  $t_{eq}$  that we begin to see the formation of neutral hydrogen and large structures such as stars and galaxies (this occurs slightly after  $t_{eq}$ ; the time of Cosmic Microwave Radiation). It is in explaining the formation of these stellar objects that cosmic strings come into play.

### Cosmic String Loops

The early Universe is known to have been nearly uniform in all aspects. This raises the question of how the mass discrepancies in today’s Universe arose (e.g., the difference in stellar density within and outside of galaxies). The inflationary model partially solves this problem by allowing random early Universe quantum fluctuations to grow to a large scale and have a

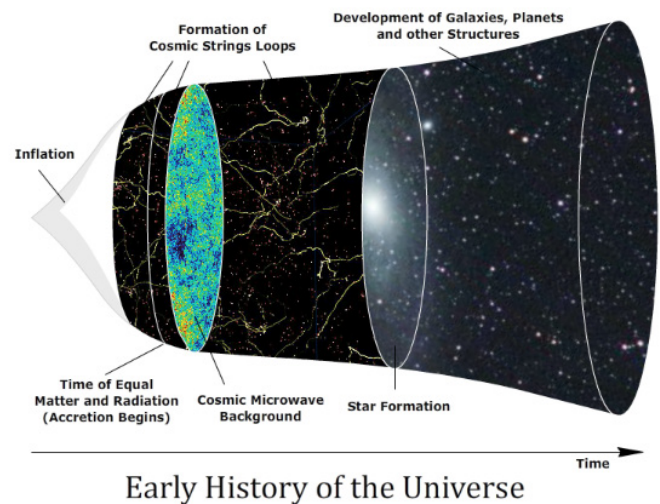


Fig. 1. Artistic impression of the early history of the Universe with reference to (1, 2) by Ling Lin. Note that cosmic string loops form during both the radiation and matter dominated epochs (to the left and right of the time of equal matter and radiation respectively), while structure formation occurs much later.

significant role in the evolution of our Universe. However, it is not successful at explaining the origin of globular clusters, so we turn to cosmic string loops as a potential source.

In the early Universe, all of space was highly dense and energetic (a “cosmic soup”). This corresponds to an excited state in each of the elementary-particle-fields. It is imperative to note that these excitations were statistically homogenous throughout the field. However, as the Universe cooled down, the excitations in the field died down. During this cooling period, topological defects in the fields may have formed. These defects arise in cases where the field values minimizing the potential energy form a circle in field space around a region of higher energy (we will call it a ‘hole’). Thus, as the excitations cool, the field values at different points in space take on values, bordering the hole, corresponding to the minimum potential (this is referred to as *symmetry breaking*). However, due to causality (no information can travel faster than the speed of light), there can be no correlation between the field values of distant enough regions of space. This causes the field values along some closed paths to take the minimum values encircling the hole in field space, requiring a location in the interior of the path where there must be, to retain continuity of the field, a core where the potential energy is not at its minimum value, causing a defect of extremely high energy density. For certain potentials (arising in a large class of particle physics models beyond the Standard Model of particle physics), these defects are cosmic strings: one-dimensional regions of extremely high energy density. Because these strings form early in the Universe (before  $t_{eq}$ ), they would have ample time to attract enough matter to form large scale objects such as galaxies (see Fig. 1).

Cosmic strings may be seen as analogous to defect lines in crystals and vortex lines in superfluids and conductors. These strings may also intersect each other and form closed loops (Fig. 2). These loops could also play a role in structure formation, and would start to accrete matter at  $t_{eq}$ ; when matter becomes the dominant form of energy.

## Introduction

Globular clusters are very tightly bound spherical collections of high star population. They are unique for being found in galactic halos, rather than in the galactic disks, and being much older than other star clusters. Their origin is not yet well understood. (3, 4)

In this paper, we propose that globular clusters may have their origin in the activity of cosmic string loops: onedimensional objects of trapped energy arising from symmetry breaking in certain particle physics models. These models will result in a network of cosmic strings of infinite length in the early Universe that will persist until the present day.

The network of cosmological strings is characterized by a mean separation distance  $\zeta(t)$  that scales with the expansion of the Universe. This separa-

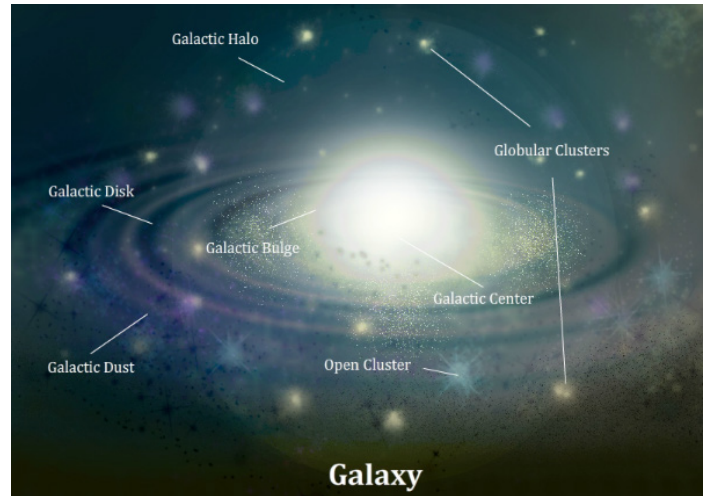


Fig. 3. Artistic impression of the Milky Way Galaxy by Ling Lin.

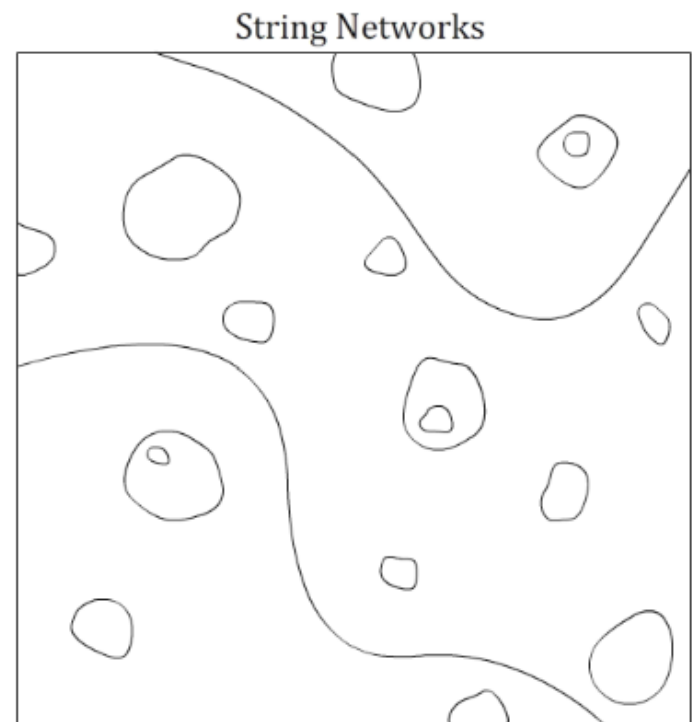


Fig. 4. A network of strings. We can see two infinite strings in addition to numerous loops of various radii.

### String Loop Formation

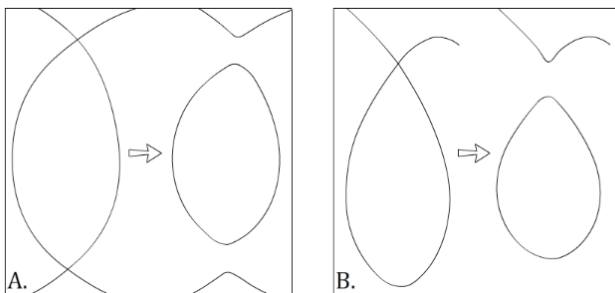


Fig. 2. Here we can see loop formation by two different mechanisms: intersection of two string segments on the left (resulting in a loop in addition to the two original string segments), and self-intersection of a segment on the right (resulting in a loop in addition to the original string segment).

tion distance determines the likelihood of the collision of cosmic strings, which produces loops. Likewise, the resulting network of cosmic string loops, which we will focus on, is characterized by a critical loop radius  $R_{cl}(t)$  whose corresponding mass dominates the mass distribution of loops.

These loops are present at very early times, forming non-linear objects before the formation of galaxies. The objects could then evolve into dense clumps which would be distributed through the galactic halo (as string loops would initially be roughly uniformly distributed in the region that falls in to form the galaxy).

Meanwhile, the cosmological effect of the cosmic strings is characterized by the constant mass per unit length of the strings  $\mu$  (usually expressed as the dimensionless  $G\mu$ , where  $G$  is the gravitational constant).

In this study, we fix  $G\mu$  by demanding that the mass accreting around a loop with radius  $R_{cl}$  agree with the observed peak in the globular cluster mass distribution. From fixing  $G\mu$ , we are then able to predict both the number density and mass distribution of globular clusters and find that they agree

with the observed results. As accretion around loops starts shortly after creation—at the time of matter and radiation equality—this mechanism offers an explanation for why globular clusters are the oldest structures in a galaxy. Our proposed mechanism further offers an explanation for why globular clusters are found in the galactic halo, as previously described.

In the following sections, we will first review the relevant literature on cosmic string loop distributions. Then, we will present our computations of  $G\mu$  and the resulting predictions it makes about globular clusters, comparing with observed values. We analyze how incorporating the initial velocity of loops affects our predicted mass distribution of globular clusters. This is then once more compared with the observed mass distribution of globular clusters in our Milky Way galaxy. Finally, we present our conclusions.

## Cosmic String Loop Distribution

We can characterize cosmic strings by their tension (or mass per unit length)  $\mu$  which is related to the energy scale  $\eta$  of the new physics by  $\mu = \eta^2$ . It is important to note that  $\mu$  is proportional to the gravitational strength generated by the string.

Cosmic strings have historically been hypothesized (5) to have seeded various cosmic structures. The ‘one string–one galaxy’ hypothesis—that galaxies originated by coalescing around cosmic strings—required a string tension of  $G\mu \sim 10^{-6}$ , corresponding to an energy scale beyond observed physics. However this model has since been ruled out by observations of the Cosmic Microwave Background (CMB) radiation (6, 7, 8, 9, 10, 11, 12, 13, 14) which set an upper limit on the string tension of

$$G\mu < 2 (10^{-7}) [1]$$

This is a generous bound which may be lowered by further analyzing CMB maps (15, 16, 17) or by constraints on the gravitational waves generated by strings. (18) These constraints restrict string loops from being heavy enough to produce large scale structures, however, strings can still play a significant role in cosmology while observing this bound, as we will explore.

In this paper, we will consider a model for the distribution of strings which implies that the loop’s radius  $R$  (which remains approximately constant) is proportional to its time of formation  $t_f$  (19, 20) Once formed, the number density of loops of radius  $R$  will decrease due to the expansion of space, and existing loops will slowly decay as they lose energy to gravitational radiation. (21) This leads to loops with a radius less than a certain critical radius  $R_{c_l}(t)$  decaying within the age of the Universe.

From what we know, we can determine the number density,  $n(R,t)$ , of string loops of radius  $R$  for times after matter-radiation equality, to depend on whether loops were formed before or after  $t_{eq}$ . (22) We can simplify this by ignoring loops forming at a time  $t_i$  after  $t_{eq}$  (as they would have less times to accrete matter), giving us the number density seen in Fig. 5. We can then find the total number density of strings by integrating  $n(R,t)$  over  $R$ . It is important to note that the number density will reach its peak at  $R \leq R_{c_l}(t)$ , and its peak will be proportional to  $(G\mu)^{-5/2}$ . (22) We also can see that smaller values of  $G\mu$  will lead to larger loop number densities, allowing more to fall into galaxies during galaxy formation.

Using the results we’ve obtained from this section, we are now prepared to examine the possibility that string loops seed the globular clusters situated in the galactic halo.

## Globular Clusters from Cosmic Strings

Linear cosmological perturbation theory tells us that accretion of matter around a cosmic string loop starts at  $t_{eq}$ . At this time, the mass distribution of the string loops is dominated by the mass  $M_c$  associated with loops of the critical radius  $R_{c_l}$ . Though these cosmic string loops will have decayed by the present time, the objects they seed will continue to grow.

## Loop Number Density

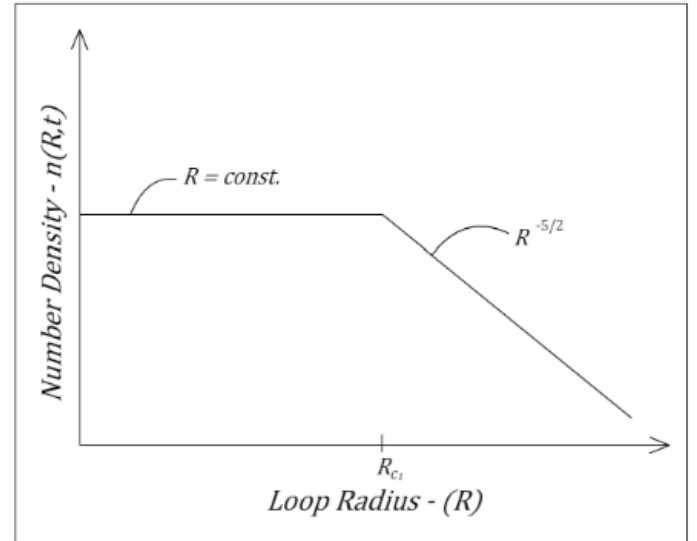


Fig. 5. The distribution of cosmic string loop radii. Note that there is a large drop-off after  $R_{c_l}$ .

Assuming accretion continues to the present time, the mass which has accreted about these seed loops will have a dependence on  $G\mu$ . (23) Taking the peak mass of globular clusters in our galaxy to be  $M_{GC} \sim 10^5$  solar masses into the number density formula, we obtain

$$G\mu \sim 10^{-9.5} \approx 3(10^{-10}) [2]$$

We estimate the number density of globular clusters within a galaxy by integrating the number density in Fig. 5 over all radius values  $R$ , and including a factor to compensate for the collapsing of loops around the galaxy into the galaxy. (24) Inserting our estimate for  $G\mu$  from Equation [2], we get a number density of globular clusters within galaxies of: (22)

$$n_{local} \sim 10^{-2} (kpc)^{-3} [3]$$

Note that this is of the same order of magnitude as the observed number density of globular clusters inside the Milky Way.

In our analysis so far, we have taken only the peak mass of our string mass distribution  $M_c$  to fix our only free parameter: the string tension. We now derive the rest of the mass distribution. As loops with radius  $R > R_{c_l}$  barely decay over the time scale of the Universe, we can say that for  $M > M_c$  the mass distribution will follow the radius distribution and scale as  $M^{-5/2}$ . For loops of smaller radius (and  $M < M_c$ ) that do decay, we predict a linear decay since the loop radius distribution is constant; however, loops with radius smaller than  $R_{c_l}$  live only a fraction of the age of the Universe.

In Fig. 6, we compare the predicted distribution (the solid lines) and the observed distribution (25) (histogram values) of globular clusters in the Milky Way. The curves are obtained by making a change of variable from  $R$  to  $M$  on the number density of loops when accretion starts at  $t_{eq}$  ( $n(R, t_{eq}) \rightarrow n(M, t_{eq}) (dR/dM)$ ), and then accounting for the expansion of space and the accretion of matter (using cosmological red-shift and the Zel’dovich approximation), (24) finally we multiply by the bin size and the volume of the Milky Way. We also plot various values of  $G\mu$  and see that increasing  $G\mu$  increases the peak mass but decreases the predicted number of globular clusters. The solid blue curves minimize  $\chi^2$  and is a surprisingly good fit of both the shape and the peak number density at the same value of  $G\mu$  at  $G\mu = 5.43(10^{-10})$ . The shape and the order of magnitude accuracy in particular are reassuring, as the scale of the function depends on a few approximations and values obtained from simulation results, and therefore has some wiggle room while the shape of the function is precisely derived.

A notable omission in this section is that we have neglected the interactions between globular clusters and the highly chaotic processes of galaxy

## Theorized and Observed Mass Distribution of Globular Clusters

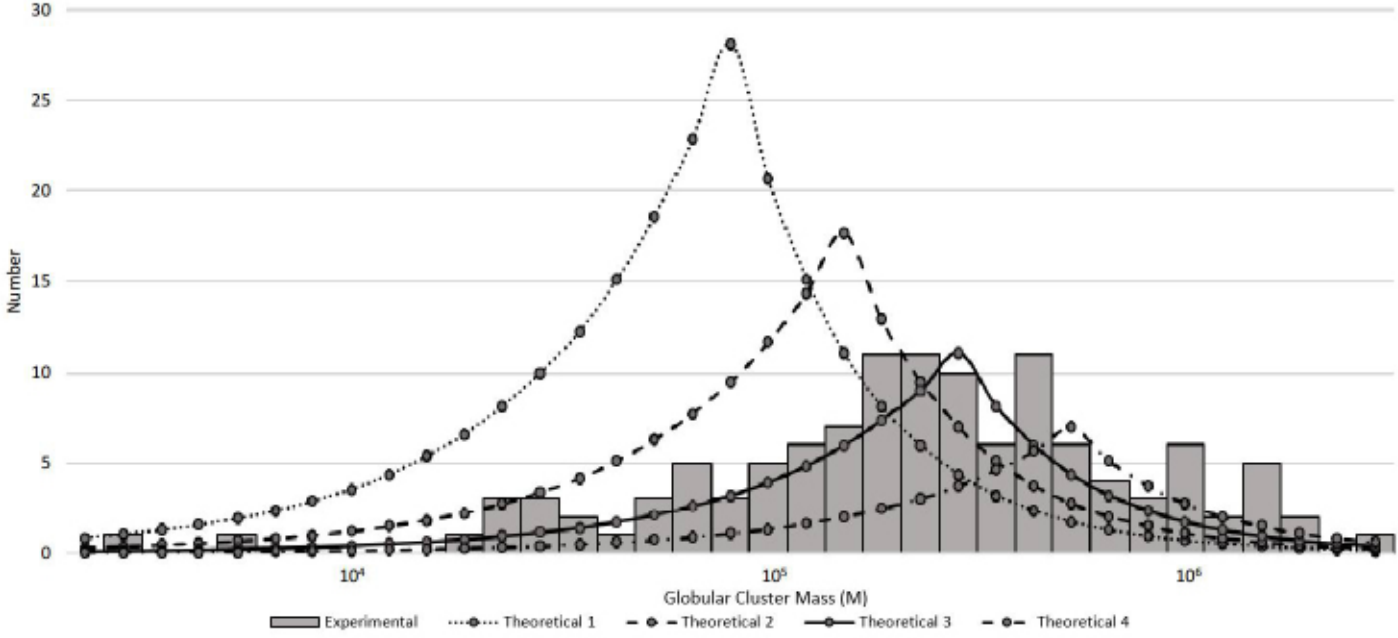


Fig. 6. Our model's predicted globular cluster mass distributions in the Milky Way for various values of  $G\mu$ . The horizontal axis is mass on a logarithmic scale, the vertical axis gives the expected number of clusters on a linear scale. The histogram show the data taken from (25). For the curves Theoretical 1, 2, 3, 4 we set  $G\mu$  as  $2.92(10^{-10})$ ,  $3.98(10^{-10})$ ,  $5.43(10^{-10})$  and  $7.41(10^{-10})$  respectively. Curve 3 ( $G\mu = 5.43(10^{-10})$ ) minimizes  $\chi^2$ .

formation that may cause changes to the mass function as a function of time in our analysis.

### Effect of Cosmic String Velocity

All of the calculations above assumed that cosmic strings are created, and remain, at rest. Recent numerical simulations (26) tell us that loops are typically born with translational velocities that are sizable fractions of the speed of light. Since long string segments usually have relativistic speeds, it is unsurprising that string loops will also gain significant velocities as they split off from string segments. When velocities are taken into consideration, accretion will not be spherically symmetric. Additionally, accretion onto a moving loop may be much less efficient compared to accretion on a stationary loop. It should be noted, however, that loop velocities also slow down as they age due to the expansion of space (so called 'red-shifting'), dampening the effect. In this section, we will approach the effect velocities through two different analyses: one considering spherical accretions and one considering more irregular accretions.

#### Analysis 1

We first focus on loop velocities that give a tight spherical accretion by making sure the distance  $\Delta r(R)$  the centre of the loop has moved before decaying is smaller than the current physical distance  $h(R, t_p)$  (27) from the center of a string loop to the accreted mass shell (in such a way we can be sure the loop remains within the accretion region):

$$\Delta r(R) < h(R, t_p) \quad [4]$$

If the loop moves further than this, we assume that no globular clusters forms. Writing the displacement  $\Delta r(R)$  in (Equation [4]) as the integral of velocity from  $t_{eq}$ , when strings loops begin accreting mass, to the present time, we obtain an upper bound  $v_i$  on the initial velocity of accreting loops. Approximating the distribution of initial velocities in each of three spatial directions to be a step function and taking the integral of the velocity distribution over accreting velocities (from zero to  $v_i$ ), we find that the rate of globular cluster formation is suppressed by a multiplicative factor  $S(R)$ :

$$S(R) \text{ proportional to } (G\mu)R^{-1/2}v_{max}^{-3} \quad [5]$$

where  $v_{max}$  is the maximum velocity of string loops, obtained through simulations. Note that this suppression factor only applies if it is less than 1. Thus, setting  $R_{c2}(G\mu, v_{max})$  such that  $S(R_{c2}) = 1$ , we find that for values of  $R < R_{c2}$  there is no suppression from velocity effects and for  $R > R_{c2}$  the suppression is given by Equation [5]. It is important to note that  $R_{c2}$  is a decreasing function of  $v_{max}$ —unlike  $R_{c1}$ , which is independent of  $v_{max}$  (re-

### $G\mu$ vs. $v_{max}^c$

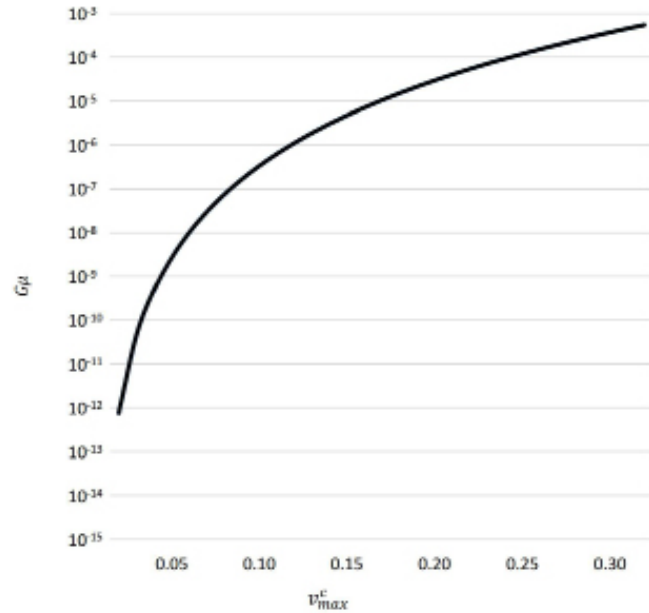


Fig. 7. Analysis 1 - Relation between  $G\mu$  and  $v_{max}^c$ . The horizontal axis is velocity on a linear scale and the vertical axis gives the  $G\mu$  on a logarithmic scale. Note that if, for a given  $G\mu$ ,  $v_{max}^c$  (as determined by simulations) falls into the region below the curve then  $R_{c1} > R_{c2}$ ; likewise,  $R_{c1} < R_{c2}$  if  $v_{max}^c$  is in the region above the curve.

### Accounting for Velocity Suppression

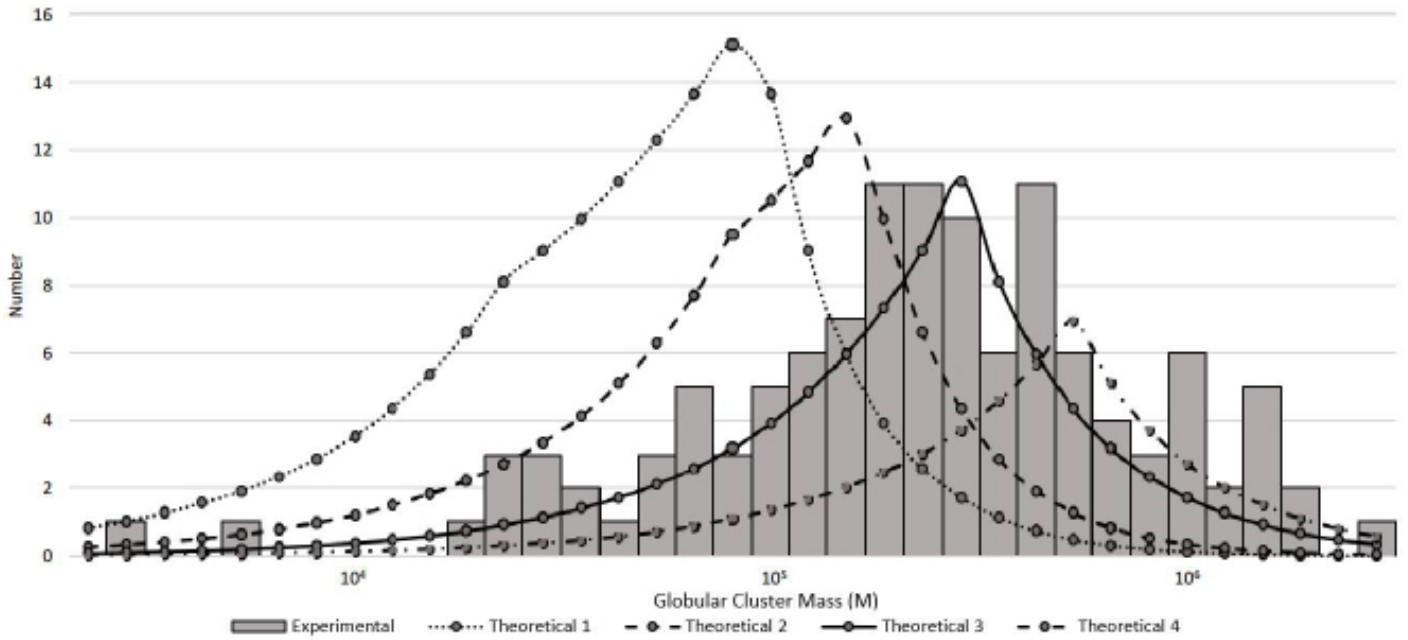


Fig. 8. Analysis 1 - Dependence of the mass function on  $G\mu$  at  $v_{max} = 3.00(10^{-2})$ . The horizontal axis is mass on a logarithmic scale, the vertical axis gives the number density on a linear scale. The histogram shows data taken from (25). For the curves Theoretical 1, 2, 3, 4 we set  $G\mu$  as  $2.92(10^{-10})$ ,  $3.98(10^{-10})$ ,  $5.43(10^{-10})$ , and  $7.41(10^{-10})$ , respectively. Notice that for curves 1 and 2,  $R_{c2} < R_{c1}$ ; for curve 3,  $R_{c2} = R_{c1}$ ; and for the solid green curve  $R_{c2} > R_{c1}$ . Curve 3 minimizes  $\chi^2$  for this particular  $v_{max}$ .

### $v_{max}^c$ Dependency of Distribution

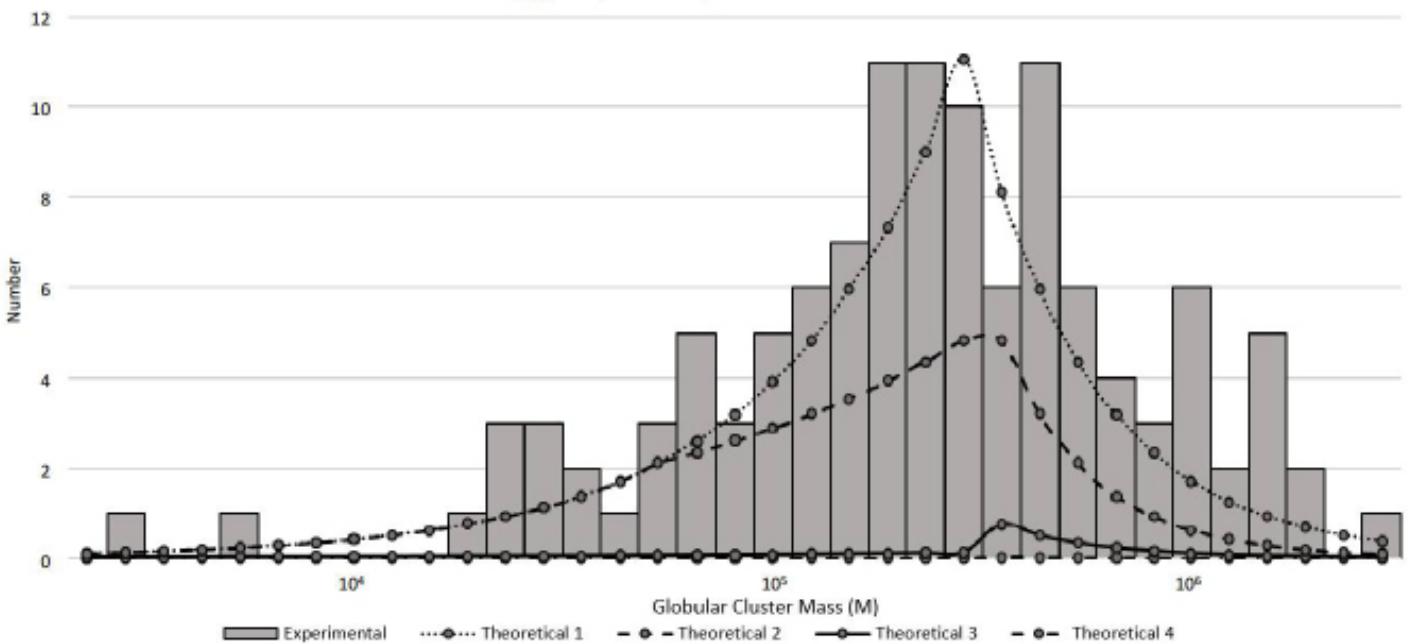


Fig. 9. Analysis 1 - Dependence of the mass function at  $G\mu = 5.43(10^{-10})$  on  $v_{max}^c$ . For the curves Theoretical 1, 2, 3, 4 we set  $v_{max}^c$  as  $1.00(10^{-1})$ ,  $6.46(10^{-2})$ ,  $3.44(10^{-2})$  and  $3.00(10^{-2})$  respectively. Notice that for all  $v_{max}^c < 3.00(10^{-2})$  we would obtain curve 4. The axes and data are the same as in the previous figure.

call that  $R_{c1}$  is the peak of the mass distribution when we ignore velocity effects). We can then obtain a critical maximum velocity  $v_{max}^c$  at which  $R_{c2}(v_{max}^c) = R_{c1}$ :

$$v_{max}^c \text{ proportional to } (G\mu)^{1/6} \quad [6]$$

Note that  $v_{max}^c$  is solely a function of  $G\mu$ , whose relation is graphed in Fig. 7. Hence, improving cosmic string loop simulations will determine if  $v_{max}^c$  is reliable and will give insight to the bounds on the string tension pa-

rameter. The importance of  $v_{max}^c$  is that it allows us to classify our models into two species. If we have  $v_{max}^c$  such that  $R_{c2}(v_{max}^c) > R_{c1}(=R_{c2}(v_{max}^c))$ , then  $v_{max}^c$  is an upper bound for  $v_{max}^c$ ; likewise, for  $R_{c2}(v_{max}^c) < R_{c1}$ , we will have  $v_{max}^c > v_{max}^c$ . This is illustrated in Fig. 7. Inputting the suppression factor into our earlier calculations, we obtain an updated relation between  $G\mu$  and the distribution in Fig. 8 and a new dependence on  $v_{max}^c$  in Fig. 9. In the case where  $R_{c2} > R_{c1}$ , the mass distribution scales as  $M^{-3}$  for  $R > R_{c2}$ , as  $M^{-5/2}$  for  $R > R > R_{c1}$  and as a linear decay for mass smaller than  $M_{c1}$  by the

same reasoning as before. Meanwhile, for  $R_{c2} < R_{c1}$ , the mass scales as  $M^3$  for  $R > R_{c1}$ , as  $M^{1/2}$  for  $R_{c2} < R < R_{c1}$  and decays linearly for  $R < R_{c2}$ . Note that the mass function when  $R_{c2} > R_{c1}$  is very similar to the previous mass function. In Fig. 8, we show that varying  $G\mu$  shifts the peak position and amplitude of the mass for a fixed  $v_{max}^c$ . For  $R_{c2} > R_{c1}$ , initial velocity effects are negligible. However, for  $R_{c2} < R_{c1}$ , but very close to the value of  $R_{c1}$  there is a slight suppression in the region  $R_{c2} < R < R_{c1}$  from velocity effects. This is where the importance of  $v_{max}^c$  comes into play. Given a  $G\mu$  value, we can run simulations to obtain the associated  $v_{max}^c$ . From plotting it in Fig. 7, we are immediately able to tell the general shape of its accretion distribution.

In Fig. 9, we consider  $G\mu = 5.43(10^{-10})$  which minimizes  $\chi^2$  in Fig. 6, we find from varying  $v_{max}^c$  that for  $v_{max}^c < 3.00(10^{-2})$ , velocity has little effect on mass distribution of globular clusters in the Milky Way galaxy. However, for  $v_{max}^c \gg 3.00(10^{-2})$  we will not obtain a mass distribution as the majority of strings will be moving too fast to maintain their accretion.

## Analysis 2

In this analysis we relax the condition that accretion is exactly spherical using the loop accretion sphericity equation  $b(t)$  (described in, (28) such that  $b(t) = 1$  for a nearly spherical object and decreases for more elliptical shapes) by consider a slightly lower bound by setting  $b(t) > 10^{-1}$ . Evaluating for  $v_i$  we find that the upper bound on the initial velocity of accreting loops in this analysis differs by only a factor of  $10^{1/3}$  from the upper bound found in the first analysis. From here, performing the same steps as in Analysis 1 would obtain results that are larger by a factor  $10^{1/3}$ . We can understand this as being due to the accretion being stretched in the direction of loop motion; this forces the loop to travel further to disrupt its accretion. This effect can be seen clearly by determining the new  $v_{max}^c$  and graphing it as in Fig. 10.

## Accretion Retention in Different Geometries

As an interesting aside, we can model highly nonspherical accretions that arise from very fast-moving loops by following the analysis in. (28) First, we determine half of the turnaround mass from a string with some initial velocity approximated by a paraboloid. Assuming that the accreted mass has uniform density, we then approximate the other half of the accreted

mass to be spherical. This gives the total mass:

$$M_t^{ns} = (4/5)ma(t). [7]$$

Comparing this to the mass from spherical accretion  $M_t^s = (2/5)ma(t)$ , we see that non-spherical accretion results in a mass that is larger by a factor of two.

## Conclusion & Discussions

The calculations above indicate that the mass distribution of string loops with mass per unit length  $G\mu \sim 10^{-9.5}$  accurately explains the origin of globular clusters. In our model, we hypothesize that the string loops that dominate the loop mass distribution at  $t_{eq}$  act as seeds for globular cluster formation. Without taking into account velocities (i.e. loops have no initial velocity,  $v_i$ ), we predict that the number of globular clusters in a galaxy will be proportionate to the mass of the galaxy.

When initial velocity is taken into account, we see that these translational motions play a small but noticeable role in the accretion of matter during the matter-dominated era. We see that cosmic string loops, born in the radiation era with initial velocity  $v_i$ , will travel a certain distance. Comparing this distance with the total size of the accreted matter gave rise to two distinct critical radii,  $R_{c1}$  and  $R_{c2}$ . In another analysis, we demanded that  $b(t) > 10^{-1}$ . This ensures that the accreted object is roughly spherical in shape. Our theory predicts a cutoff velocity: any loops with higher translational speeds will simply not form any observable objects.

Aside from globular clusters, it is noteworthy to mention that the analyses discussed in this report may also be applied to ultra-compact-mini-halos, as they too can be manifestations of cosmic string loop accretions. One question not discussed here is the formation of stars inside the accreted matter. (29, 30) It is entirely possible that there will be a significantly different star formation process for matter accreting onto a string loop inside a galaxy, as opposed to in a field (open area) in between galaxies.

## Acknowledgements

We wish to thank R. Brandenberger for useful discussions and encouragement

## References

1. Centre for Theoretical Cosmology, "The Origins of the Universe: Cosmic defects," Web. Aug. 2016.
2. R. Nemiro and J. Bonnell, "Astronomy Picture of the Day," Web. Aug. 2016.
3. W. E. Harris, "Massive star clusters in galaxies," Philosophical Transactions of the Royal Society of London Series A, vol. 368, pp. 889–906, Jan. 2010.
4. J. P. Brodie and J. Strader, "Extragalactic Globular Clusters and Galaxy Formation," ARA&A, vol. 44, pp. 193–267, Sept. 2006.
5. R. Battye and A. Moss, "Updated Constraints on the Cosmic String Tension," Phys. Rev. D, vol. 82, p. 023521, 2010. [arXiv:1005.0479].
6. P. D. Mouskops and et al. [Boomerang Collaboration], "Measurement of a Peak in the Cosmic Microwave Background Power Spectrum from the North American test flight of BOOMERANG," Astrophys. J, vol. 536, p. L59, 2000. [arXiv:astro-ph/9911444].
7. A. K. [the ACT Collaboration], "The Atacama Cosmology Telescope Project: A Progress Report," NewAstron. Rev, vol. 50, p. 969, 2006. [arXiv:astro-ph/0608549].
8. J. L. Sievers and et al. [Atacama Cosmology Telescope Collaboration], "The Atacama Cosmology Telescope: Cosmological parameters from three seasons of data," JCAP, vol. 1310, p. 060, 2013. [arXiv:1301.0824].
9. J. E. Ruhl and et al. [The SPT Collaboration], "The South Pole Telescope," Proc. SPIE Int. Soc. Opt. Eng., vol. 5498, p. 11, 2004. [arXiv:astro-ph/0411122].
10. Z. Hou, C. L. Reichardt, K. T. Story, B. Follin, R. Keisler, K. A. Aird, B. A. Benson, L. E. Bleem, and et al., "Constraints on Cosmology from the Cosmic Microwave Background Power Spectrum of the 2500 deg<sup>2</sup> SPT-SZ Survey," Astrophys. J., vol. 782 no. 2, p. 74, 2014. [arXiv:1212.6267].
11. C. L. Bennett and et al., "First Year Wilkinson Microwave Anisotropy Probe

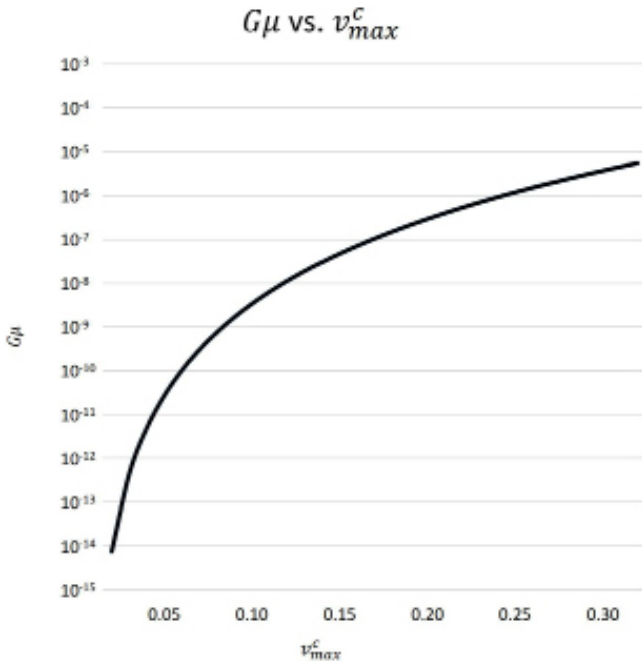


Fig. 10. Analysis 2 - Relation between  $G\mu$  and  $v_{max}^c$  for  $b(t) = 10^{-1}$ . The horizontal axis is velocity on a linear scale and the vertical axis gives the  $G\mu$  on a logarithmic scale. As before if, for a given  $G\mu$ ,  $v_{max}$  (as determined by simulations) falls into the region above the curve then  $R_{c1} > R_{c2}$ , and  $R_{c1} < R_{c2}$  if  $v_{max}$  is in the region below the curve.

- (WMAP) Observations: Preliminary Maps and Basic Results,” *Astrophys. J. Suppl.*, vol. 148, p. 1, 2003. [arXiv:astro-ph/0302207].
12. P. A. R. Ade and et al. [Planck Collaboration], “Planck 2013 results. XVI. Cosmological parameters,” *Astron. Astrophys.*, vol. 571, p. A16, 2014. [arXiv:1303.5076].
  13. C. Dvorkin, M. Wyman, and W. Hu, “Cosmic String constraints from WMAP and the South Pole Telescope,” *Phys. Rev. D*, vol. 84, p. 123519, 2011. [arXiv:1109.4947].
  14. P. A. R. Ade and et al. [Planck Collaboration], “Planck 2013 results. XXV. Searches for cosmic strings and other topological defects,” *Astron. Astrophys.*, vol. 571, p. A25, 2014. [arXiv:1303.5085].
  15. R. J. Danos and R. H. Brandenberger, “Canny Algorithm, Cosmic Strings and the Cosmic Microwave Background,” *Int. J. Mod. Phys. D*, vol. 19, p. 183, 2010. [arXiv:0811.2004].
  16. S. Amsel, J. Berger, and R. H. Brandenberger, “Detecting Cosmic Strings in the CMB with the Canny Algorithm,” *JCAP*, vol. 0804, p. 015, 2008. [arXiv:0709.0982].
  17. A. Stewart and R. Brandenberger, “Edge Detection, Cosmic Strings and the South Pole Telescope,” *JCAP*, vol. 0902, p. 009, 2009. [arXiv:0809.0865].
  18. R. Battye and A. Moss, “Updated constraints on the cosmic string tension,” *Phys. Rev. D*, vol. 82, p. 023521, 2010. [arXiv:1005.0479].
  19. A. Vilenkin, “Cosmic Strings,” *Phys. Rev. D*, vol. 24, p. 2082, 1981.
  20. T. W. B. Kibble, “Evolution of a System of Cosmic Strings,” *Nucl. Phys. B*, vol. 252, p. 227, 1985.
  21. T. Vachaspati and A. Vilenkin, “Gravitational Radiation from Cosmic Strings,” *Phys. Rev. D*, vol. 31, p. 3052, 1985.
  22. A. Barton, R. H. Brandenberger, and L. Lin, “Cosmic strings and the origin of globular clusters,” *JCAP*, vol. 06, 2015.
  23. R. H. Brandenberger, “Topological Defects and Structure Formation,” *Int. J. Mod. Phys. A9*, p. 93, 1994. [arXiv:astro-ph/9310041].
  24. Y. B. Zel’dovich, “Gravitational Instability: An Approximate Theory for Large Density Perturbations,” *A&A*, vol. 5, p. 84, 1970.
  25. O. Y. Gnedin and J. P. Ostriker, “Destruction of the Galactic Globular Cluster System,” *ApJ*, vol. 474, p. 223, 1997. [arXiv:astro-ph/9603042].
  26. J. J. Blanco-Pillado, K. D. Olum, and B. Shlaer, “Large Parallel Cosmic String Simulations: New Results on Loop Production,” *Phys. Rev. D*, vol. 83, p. 083514, 2011. [arXiv:1101.5173].
  27. M. Pagano and R. H. Brandenberger, “The 21cm Signature of a Cosmic String Loop,” *JCAP*, vol. 05, p. 014, 2012. [arXiv:1201.5695].
  28. E. Bertschinger, “Cosmological Accretion Wakes,” *ApJ*, vol. 316, p. 489, 1987.
  29. B. Shlaer, A. Vilenkin, and A. Loeb, “Early Structure Formation from Cosmic String Loops,” *JCAP*, vol. 05, p. 026, 2012. [arXiv:1202.1346].
  30. F. Duplessis and R. Brandenberger, “Note on Structure Formation from Cosmic String Wakes,” *JCAP*, vol. 1304, p. 045, 2013. [arXiv:1302.3467].

# Understanding the 2013-2015 Ebola Outbreak

## Abstract

**Background:** The 2013-2015 Ebola outbreak caused severe human suffering and a global health crisis. Ebola Virus (EBOV) is a naturally zoonotic RNA virus that has several immune-evasion mechanisms and can cause serious disease and death in humans. The massive impact of the recent epidemic is unique in the 40-year history of this pathogen. Scientists and public health officials around the world are researching the factors that may have contributed to the scale and devastating nature of the 2013-2015 outbreak.

**Methods:** Terms searched online through the McGill library and Medline Ovid included “Ebola”, “immune evasion”, “sequencing”, “Ebola glycoprotein” and “zoonotic transmission”. Only articles published since 2014 were selected.

**Summary:** In this review article, we will provide discussion on the principal factors contributing to the unusually destructive nature of the 2013-2015 Ebola outbreak. Interestingly, although several nonsynonymous mutations have been observed in the recently circulating strains, they were not the principal cause of the unusually devastating nature of the outbreak. Instead, the high rate of transmission was likely caused by sociological factors, such as population dynamics and late detection of the outbreak. However, there is evidence to suggest that once the high rate of transmission in humans was established there was selective pressure on the virus to evade the human immune system. This selective pressure may have exacerbated an already deadly outbreak. Ongoing research efforts indicate that there is still much to be discovered about the virus and the control of outbreak management.

## Introduction

The 2013-2015 outbreak of Ebola Virus Disease (EVD) had 28,637 reported cases and 11,314 deaths in West Africa, with widespread transmission in Guinea, Liberia and Sierra Leone. (1) Several other regions have also been affected, with cases in other parts of Africa, Europe, and the United States. (1) In comparison, in the 24 previously recorded outbreaks from 1976 to 2013, a total of 2,400 cases were reported, with only seven of these outbreaks resulting in greater than 100 reported cases. (2) The unprecedented scale of the 2013-2015 Ebola outbreak has raised many questions in scientific and public health communities about the factors which contributed to the virulence and high level of human-to-human transmission that characterized this outbreak. The long-term impacts of EVD on survivors as well as the affected regions are still unclear.

Early sequencing data from strains circulating in Guinea suggested that a single introduction event from an unknown reservoir was the source of the outbreak. (3) This strain of EBOV had not been previously defined, and was named “Makona”, after the Makona River situated at the border of Liberia, Guinea, and Sierra Leone. (3) In addition to Makona, a second strain, named “Lomela” was associated with approximately 70 cases of EVD in the Democratic Republic of the Congo. (3) Research suggests that fruit bats may be the natural reservoir of EBOV; however many other organisms, such as gorillas and chimpanzees have been found to harbor the virus. (4, 5) The identification of the unknown natural reservoir of EBOV and the characteristics that differentiate Makona from previous EBOV strains will continue to be important in gaining a more complete understanding of EVD.

EBOV, also known as *Zaire Ebolavirus*, is a negative-sense single-stranded RNA virus of the *Ebolavirus* genus of *Filoviridae* family. (6) Of the 5 species in the *Ebolavirus* genus, *Zaire Ebolavirus* is the member species, and there are four other species in the *Ebolavirus* genus including the most virulent. (7) The RNA genome codes for seven genes that are processed into eight proteins. (8) The ribonucleoprotein complex is made up of the viral genome and viral proteins nucleoprotein (NP), large structural protein (L) (the RNA-dependent RNA polymerase), and viral proteins 35

(VP35) and 30 (VP30). (8) The viral envelope is derived from the host cell surface, which has been lined with viral proteins 40 and 24 (VP40/VP24), the matrix proteins. (8) The glycoprotein gene codes for a transmembrane protein, called GP or GP<sub>1,2</sub>, and a soluble glycoprotein called sGP. (9) GP is cleaved after translation to form the GP<sub>1</sub> and GP<sub>2</sub> subunits, and allows the virus to interact with host cells. (9) Specifically, GP<sub>1</sub> mediates attachment to the host cell, while GP<sub>2</sub> mediates fusion. (9) The exact role of the, (sGP), is unknown. (6)

Two mechanisms have been described which allow EBOV to evade the human immune system during infection. (6) The first mechanism is mediated by VP35 and VP24. (6) These viral proteins inhibit type 1 interferon (IFN) production and signaling, an important part of the innate immune response against viruses. (10) VP35 binds to double-stranded (ds) RNA as well as the 5' cap structure to protect the viral dsRNA from being recognized by cellular sensors of foreign RNA. (10) As depicted in Fig. 1, this prevents the activation of the retinoic acid inducible gene I (RIG-I) pathway and therefore the production of IFN- $\alpha$  and IFN- $\beta$ , which are necessary in establishing an early immune response. (11) VP24 interferes with karyopherin-1 $\alpha$ , the protein that transports signal transducer and activator of transcription 1 (STAT1) into the nucleus. (12) There is also evidence that VP24 interacts directly with STAT1. (13) When STAT1 is inhibited from entering the nucleus, it cannot activate transcription of the genes needed for an effective IFN response (Fig. 2). (11) Both VP24 and VP35 are necessary to attenuate IFN signaling and effectively evade the immune response. This IFN antagonism is of great importance as it allows EBOV to be persist in its human host.

The second major immune evasion mechanism used by EBOV is mediated by the viral glycoproteins. (14) sGP has been found to reduce the amount of antibody production specific to GP<sub>1,2</sub> by stimulating the production of antibodies that cross-react with sGP and GP<sub>1,2</sub>. (9) Additionally, GP<sub>1,2</sub> has a “steric shielding effect” that blocks the major histocompatibility complex 1 (MHC-1),  $\beta$ 1-integrin, and FAS from detection by the immune system. (15, 16) These surface proteins are important for infected cells to interact with the cells of the immune system, so their inaccessibility in the case of steric shielding greatly inhibits the host's ability to protect against viral infection. (15, 16) GP<sub>2</sub> subunit can also inhibit the cell's ability to prevent

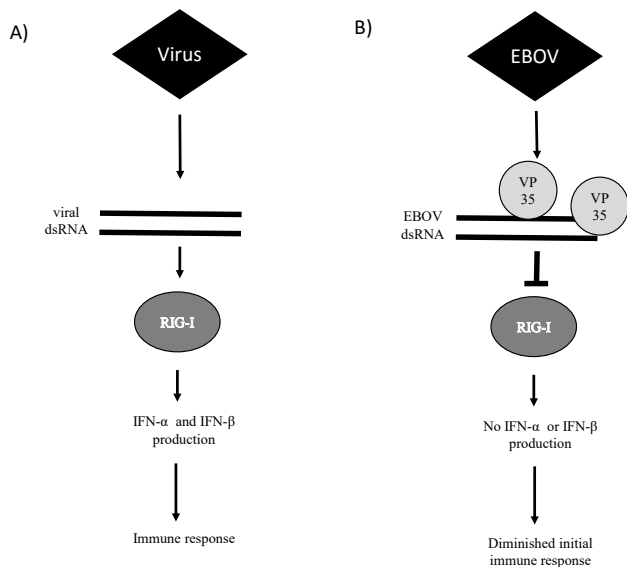


Fig. 1: VP35 Immune Evasion. (A) Normal RIG-I pathway. RIG-I senses double stranded RNA in the cell and promotes the expression of interferon- $\alpha$  and interferon- $\beta$  (5). (B) In a cell infected by EBOV, VP35 binds to viral double stranded RNA at the phosphate backbone and the 5' cap to prevent RIG-I from sensing the infection (4).

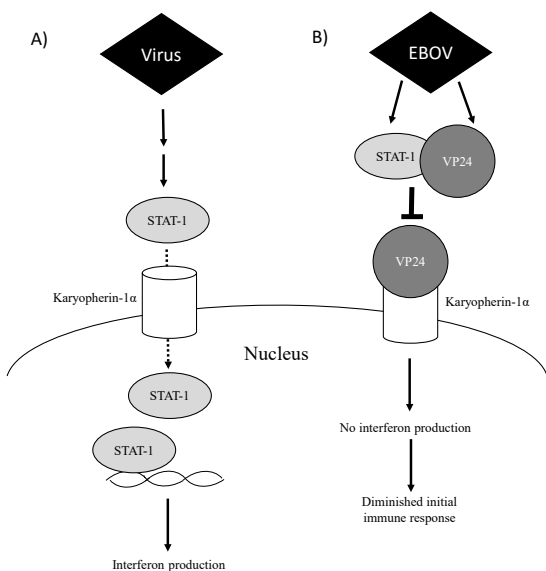


Fig. 2: VP24 Immune Evasion. (A) Normal STAT-1 pathway. Viral infection activates STAT-1, which enters the nucleus and acts as a transcription factor to activate interferon production (5). (B) In a cell infected by EBOV, VP24 binds to STAT-1, preventing it from entering the nucleus. VP24 also interacts with karyopherin-1 $\alpha$ , further preventing STAT-1 translocation into the nucleus (4).

viral release by moving the tetherin in the cell. (17) Tetherin is a transmembrane glycoprotein that retains viral particles in the infected cell and is therefore an anti-viral mechanism. (17) Through its interaction with tetherin, GP<sub>2</sub> allows EBOV to evade this host defense strategy. (17) Hence, it is likely that both sGP and GP<sub>1,2</sub> contribute to the pathogenicity of EBOV in humans.

In addition to immune evasion, EBOV infection results in severe consequences for the human host. Although the clinical course of EVD is well known, the mechanisms associated with EBOV pathogenicity are not well defined. EBOV is able to invade almost all host cells, but early replication is thought to occur primarily in macrophages and dendritic cells. (18) The virus destroys infected cells, thus inhibiting several crucial physiological systems, such as the immune system. (19) This is yet another immune

evasion strategy of EBOV. In particular, infections become fatal when the inflammatory response is dysregulated, leading to systemic inflammation. (20) In addition, EBOV has been shown to decrease endothelial-cell barrier function and affect the synthesis of blood coagulation protein in the liver. (21) These host-virus interactions are central to the clinical course of EVD.

In the aftermath of the 2013-2015 Ebola outbreak, it is evident that the mechanisms underlying the severe pathogenicity and rapid spread of the virus are not completely elucidated. These questions are especially perplexing when comparing the scale of this most recent outbreak to the other EBOV outbreaks over the past 40 years. This review article suggests that evolution of EBOV leading up to and during the 2013-2015 epidemic contributed only minimally to the severity of the outbreak.

## Results

### Evolution Rates Between and Within Outbreaks

A logical place to start in forming an understanding of the virulence of the 2013-2015 Ebola epidemic is a comparison between the circulating strains during the most recent epidemic and strains found in previous, less severe epidemics. In a study by Gire and colleagues, they sequenced 99 Ebola virus genomes from 78 patients in Sierra Leone in 2014. (22) When compared to all previously published EBOV sequences, these strains contained 341 fixed substitutions, including 35 nonsynonymous, 173 synonymous and 133 noncoding mutations. (22) In 2015, Park *et al.* sequenced and analyzed 232 EBOV genomes from Sierra Leone and compared them to the 78 genomes that had been previously reported in 2014. (23) In the 232 sequences analyzed, 85 contained at least one intra-host single-nucleotide variant (iSNV). Interestingly, several iSNVs were found in two or more sequences. (23) iSNVs are important because they can be tracked from patient to patient and provide information about chains of transmission. (22) The presence of iSNVs shared between samples indicates that the transmission bottleneck allowed for a mutation acquired in one host to be transferred to another. (23) This sequencing data was a crucial first step in determining whether mutations in specific regions of the EBOV genome contributed to its high virulence in the 2013-2015 outbreak.

Comparing the genomes originally sequenced by Gire *et al.* to those later sequenced by Park *et al.* provided significant insight as to the impact of large-scale human-to-human transmission of EBOV. The substitution rate observed by Gire *et al.* was found to be almost twice as high, with more nonsynonymous mutations within the 2014 outbreak, compared to the rate of evolution since the emergence of EBOV. This early evidence suggested that the progression of the epidemic allowed the virus to adapt. (22) Park *et al.* challenge these findings and, specifically, the high reported rate of nonsynonymous mutations. (23) The authors found that in contrast to the original estimations by Gire *et al.*, the evolution rate of Makona was similar to the long-term evolution rate observed between outbreaks. (23) This phenomenon was attributed to purifying selection whereby mutations that have a deleterious effect on protein structure or function are eliminated. (24) Purifying selection is observed when there are more synonymous mutations than nonsynonymous in the genome. (24) In the case of EBOV from 2013-2015, although a higher than expected rate of nonsynonymous mutations was found early in the outbreak, these mutations were often deleterious, and impaired viral fitness. (23) As a result, they were transmitted to new hosts with a low frequency and were often only observed in a single individual. To visualize this phenomenon, Park *et al.* created a phylogenetic tree of derived alleles at genomic position 18.911. (23) The deleterious mutations occur on the external branches of this phylogenetic tree. (23) On internal branches of the phylogenetic tree, there are mutations present in multiple samples. (23) In these internal branches, nonsynonymous mutations accumulated at a much lower rate compared with synonymous mutations. As the epidemic progressed most of the mutations that were sustained in multiple hosts were synonymous, since if the mutation was sustained, then the virus was fit enough to replicate and therefore did not suffer any major deleterious nonsynonymous mutation. (23) This may explain why

the initially high rate of evolution during the outbreak did not continue further into the epidemic. Although the evolutionary rates found in these two studies contradict each other, both studies suggest that there were several nonsynonymous mutations in the Makona strain, when compared to EBOV strains isolated in previous outbreaks. (22, 23) It was hypothesized that these mutations may have contributed to the high virulence of the Makona strain.

### Evolution of the IFN Antagonism System Between Outbreaks

A study by Dunham and colleagues in 2015 built on the genetic sequence data provided by the Gire and Park studies. (25) Their research assessed whether the nucleotide substitutions that differentiated the VP24 and VP35 genes of the Makona virus from the prototype strain, Mayinga, increased viral fitness or the ability to inhibit the host IFN response. (25) The authors used a monocistronic minigenome system as a model of viral replication and transcription. (25, 26) This allowed them to measure whether the Makona VP24 and VP35 proteins had an increased ability to function as a cofactor for the viral RNA polymerase, thus resulting in an overall increase in viral fitness. (25) By measuring transcription and replication rates, they found that the VP35 and VP24 proteins from Makona virus had indistinguishable effects on genome replication from the prototype virus. (25)

In a second experiment Dunham *et al.* tested VP35 and VP24's IFN interferon antagonism. (25) The ability of VP35 to inhibit IFN- $\beta$  production was measured with cells that were transfected with a reporter plasmid under the control of an IFN- $\beta$  promoter and various concentrations of a VP35 construct. (25) Reporter gene expression was stimulated by co-transfection of plasmids containing the caspase activation and recruitment domain (CARD) of RIG-I. (25) The CARD domain is constitutively active and stimulates the production of IFN through the IFN- $\beta$  promoter. (25) A similar experiment was carried out to assess VP24's IFN antagonism. In this experiment a reporter plasmid under the control of an IFN stimulated response element, which was stimulated with human IFN- $\beta$ , was used. (25) For both VP24 and VP35, there was no statistical difference in function between the Makona and Mayinga variants in IFN antagonism. (25) Thus, these results suggest that none of the nonsynonymous mutations investigated provide Makona virus with an increased fitness over the Mayinga virus, with respect to either EBOV replication or IFN antagonism.

### Evolution of Glycoprotein

Two studies investigated the effect of evolution of the EBOV GP on Makona virulence. (23, 27) In a study by Azarian *et al.*, 65 glycoprotein sequences from epidemic waves between 1976 and 2014 were used to reconstruct the evolutionary history of EBOV. (27) This analysis found that, over time, the evolution of EBOV has been driven by neutral genetic drift, demonstrated by the similar rates of synonymous and non-synonymous mutations. Furthermore, specific amino acid substitutions were found to be mostly transient, rather than established in the population. (27) This indicates that over a large time scale, there has been little selection acting on the EBOV glycoprotein. This may be because GP is implicated in host cell attachment and fusion. (27) Therefore, mutations in this protein may affect the virus' ability to infect host cells making it impossible for the virus to survive.

A second analysis, carried out by Park *et al.* focused on a shorter timescale to determine the effect of human-to-human transmission on the EBOV genome. (23) They found that although the general rate of non-synonymous mutations decreased as the outbreak progressed, this was not true for the mucin-like domain of the EBOV GP. (22) The authors compared the rate of nonsynonymous to synonymous mutations, both during the outbreak and between outbreaks, for all of the major proteins in EBOV. They found that the mucin-like domain of the glycoprotein was the only region in which the log of the rate was greater than 1. This implies that both between and within outbreaks, there were more non-synonymous substitutions than would be expected under neutral genetic drift. (23) According to the authors, the higher rate of nonsynonymous substitutions suggests that the evolution of GP, the primary target of host antibodies, may be subject to faster than usual evolution and diversifying

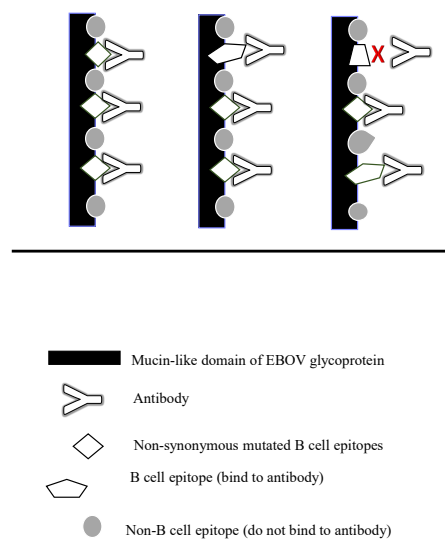


Fig. 3: Evolution of the EBOV Glycoprotein During the Epidemic. A schematic representation of the evolution of different regions of the mucin-like domain of the EBOV glycoprotein from September 2014 to June 2015. Non-synonymous mutations occurred more often than under neutrality only in the B-cell epitopes. This indicates that, under the selective pressure of the human immune system, EBOV may have evolved to evade host antibodies (8).

selection. In the context of virus-host interactions, this could change the antibody-binding sites on GP and allow the protein to evade the host humoral immune response. To test this hypothesis, the authors needed to determine whether the nonsynonymous mutations occurred within regions of the mucin-like domain that are bound by antibodies. Park *et al.* used the Virus Pathogen Database to find experimentally determined sequences of B cell epitopes. (23, 28) They found that there were in fact more nonsynonymous mutations in the regions of GP that bind to antibodies would be expected by chance (Fig. 3). (23) This finding supports the idea that the selective pressure acting on the virus is the human humoral immune response and that due to extensive human-to-human transmission, the EBOV evolved to better evade the host immune system.

### Sociological Factors

Other studies in Ebola viral dynamics have argued that further genomic sequencing will not allow us to understand the severity of the recent outbreak. (27) Instead of changes in viral phenotype, research points to human behavior, population dynamics, and late detection of the outbreak as important contributing factors.

It can be argued that changes in land use and cultural practices have increased human exposure to zoonotic hosts, making an outbreak more likely. (29) Specifically, forested land which previously blocked human-animal contact, is now being used for agriculture, industry, and residential areas, which do not afford the same protection from zoonotic reservoirs of EBOV. (29) Further increasing this risk of exposure are practices such as bush meat hunting and burial traditions. (30) As zoonotic transmission events become increasingly possible, EBOV has the ability to infect more and more people. Furthermore, since it is believed that Ebola virus is harbored in many animal hosts, there is a possibility of various strains from different animals being introduced into human populations. (4, 5)

Other research points to rapidly changing population dynamics in areas where zoonotic transmission is possible as a factor contributing to the scale of the recent outbreak. (30) Over the past 40 years, the proportion of people living in urban areas has increased from 25.5% to 59.2% in the predicted zoonotic niche of EBOV. (30) As people live in closer proximity to each other, the likelihood of viral transmission increases. (30) Furthermore, populations are significantly more interconnected than they

were in 1976. During the eight-year period from 2005-2012 alone, global airline passenger volumes increased by one third. (30) Importantly, increased mobility has made it easier for the virus to be transmitted across national borders.

A final factor that has been explored is the impact of late detection of the zoonotic transmission event and the subsequent human-to-human transmission. The early symptoms of EVD are non-specific, making it difficult for health practitioners to recognize early cases as being EVD. (31) Furthermore, poor health infrastructure and epidemiological surveillance systems in place in Western Africa contributed to late detection. (31) In analyzing the response times in previous Ebola outbreaks, it is not surprising that when the outbreak is not detected early, there is a greater likelihood that it will migrate from rural to urban areas. (31) While it is difficult to quantify the effects of these various sociological factors, changes in behavior, land use, and undeveloped public health systems likely contributed to the scale of the 2013-2015 EBOV outbreak.

## Discussion

### Genetic Variation

The major conclusion that can be drawn from these results is that no major mutations of the EBOV have been identified that allowed it to spread more quickly and cause greater human suffering compared to the previous 24 recorded Ebola outbreaks. However, sustained transmission afforded the virus an unprecedented opportunity to adapt in the human host, leading to some mutations in GP involved in immune evasion. (23) This indicates that evading the human immune system may be the pressure that is driving evolution. Since this pressure requires sustained transmission to have a lasting effect on the viral genome, it cannot be the initial cause of the high rate of transmission or what dictated the unprecedented scale of this outbreak. Once the outbreak was underway however, it is possible that the mutations in this domain may have exacerbated the spread of disease and contributed to the Makona strain's pathogenicity and transmission. Furthermore, if the virus has in fact evolved to be more pathogenic during this outbreak, future outbreaks may be increasingly destructive.

The idea that the initial scale of the outbreak was not due to a mutation is supported by four main studies that investigated EBOV sequences in the 2013-2105 outbreak (Makona) and previous outbreaks (Mayinga). (22, 23, 25, 27) While the Gire and Park studies focused on comparing overall rates of synonymous to nonsynonymous mutations, the Azarian and Dunham studies focused on the proteins involved in EBOV immune evasion. Taken together, their findings demonstrate that the evolution of the EBOV has been generally driven by neutral genetic drift. Furthermore, between outbreaks, there is no known selective evolutionary pressure on the virus to become more pathogenic to humans, and thus

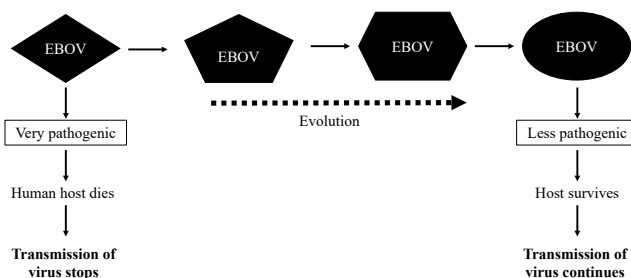


Fig. 4: The Effect of Extended Human-to-Human Transmission of EBOV- Dead-End Host Concept. Humans are a dead-end host for EBOV. If the virus is too pathogenic, it will kill the host and the chain of transmission will be broken. Therefore, over the course of an epidemic, natural selection will select a virus that is less pathogenic, so the host can survive and continue transmission, thus ensuring survival of the virus (9).

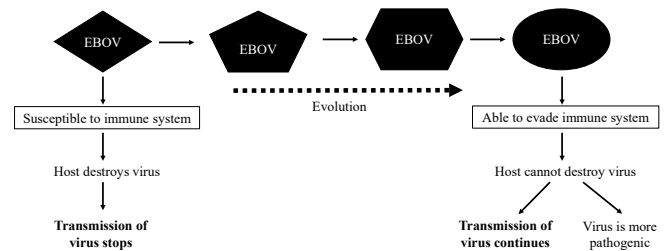


Fig. 5: The Effect of Extended Human-to-Human Transmission of EBOV – Immune Evasion Concept. If EBOV is susceptible to the host immune system, the virus will die and transmission will stop. Therefore, over the course of an epidemic, natural selection will select for a virus that is better able to evade the immune system, so transmission can continue (8). However, this selective pressure also makes the virus more pathogenic to the host.

there have been no sustained mutations that have led to a hyper-virulent strain of EBOV.

The continued human-to human transmission of EBOV observed during the recent outbreak was unprecedented for this virus. (23) There is currently contention within the scientific community as to the effects of this sustained transmission. Dunham *et al.* argue that conceptually, since sustained human-to-human transmission is not characteristic of EBOV, evolutionary pressure would select a less pathogenic virus, thus increasing the chances that the host survives and can transmit the virus (Fig. 4). (25) This was supported by their findings that neither VP24 nor VP35 of the Makona strain have an increased ability to aid in viral transcription or replication, or to interfere with the host IFN response. (25) On the other hand, Park *et al.* argue that there is a selective pressure on the virus to evade the host immune system. (23) While the main reason for this evolutionary pressure is to ensure the survival of the virus, as a by-product, these mutations may also make the virus more pathogenic (Fig. 5). This argument was supported by the higher than expected rate of non-synonymous mutations observed in the mucin-like domain of GP. This indicates the possibility of host antibodies driving the selection of altered B-cell epitopes, which inhibit the humoral immune response. (22) However, as the authors noted, these findings were based on a very small sample size. Furthermore, since the B-cell epitopes used in the analysis were not determined from an *in vivo* study, they may not be immunodominant. (23) Although the selective pressures that arose during the outbreak are still not completely understood, elucidating these mechanisms may yield critical information in understanding past outbreaks and managing EBOV in the future.

Continued genetic analysis of EBOV is necessary to understand the factors that made the recent Ebola outbreak so destructive. Due to the high level of pathogenicity of the virus and the geographical location of the outbreak, research has been slow and laborious. Park *et al.* suggest that an important research topic in the immediate future is to develop methods to deactivate the virus while maintaining the integrity of the sample so that it can be used for high-quality genomic sequencing. (23) The ultimate goal of continued research efforts is to be able to prevent the transmission and the suffering associated with EVD.

### Sociological Factors

The evidence that none of the mutations in the viral genome over the past four decades can explain the scale of the 2013-2015 epidemic supports the idea that sociological factors played a critical role. (27) To assess the impact of these factors, we must determine if there has been a change since previous EBOV outbreaks and if this change affected viral transmission patterns. For example, although there were changes in land use that lead to increased exposure to zoonotic hosts, this was unlikely to affect viral transmission. This is because epidemiological analysis of the 2013-2015 outbreak suggests that there was a single event that introduced the virus into humans. (22) Therefore, though changes in land

use may have allowed for the initial transmission event, this does not account for the scale of the outbreak.

On the other hand, changes in population dynamics did lead to the possibility of “superspreading events”. For example, the burial of a single patient in Sierra Leone is linked to 300 EVD cases. (2) Furthermore, in contrast to the recent urban Ebola outbreak, past outbreaks began in isolated rural areas and did not spread to urban settings. (31) This allowed for more effective outbreak-control strategies. (31) Based on the above evidence, it is likely that urbanization and mobility significantly contributed to the high number of cases of EBOV during the 2013-2015 outbreak. Finally, late detection has a significant impact on the effectiveness of control interventions. (31) Once the virus has travelled to a densely populated area, it becomes increasingly difficult to control. (30) This suggests that along with changing population dynamics, late detection of the outbreak had a large impact on the level of Ebola transmission.

## Conclusion

In conclusion, analysis of the 2013-2015 Ebola outbreak indicates that sociological conditions, rather than genetic mutations, were the main factors contributing to the unprecedented scale and impact of the outbreak. While mutations during sustained human-to-human transmission may have exacerbated the outbreak, the initial causes were likely the increase in urban populations and late detection of the zoonotic transmission event. Therefore, research into how Ebola virus infects hosts, how it evades the immune system and the sociological factors surrounding EVD are vital to controlling future outbreaks.

## Acknowledgements

I would like to thank Dr. Martin Richer of the McGill Department of Microbiology and Immunology for his guidance and suggestions.

## References

- Control CfD. 2014 Ebolae Outbreak in West Africa. In: Services USDoHaH, editor. 2015.
- Osterholm MT, Moore KA, Kelley NS, Brosseau LM, Wong G, Murphy FA, et al. Transmission of Ebola viruses: what we know and what we do not know. *MBio*. 2015;6(2):e00137-15.
- Kuhn JH, Andersen KG, Baize S, Bào Y, Bavari S, Berthet N, et al. Nomenclature- and Database-Compatible Names for the Two Ebola Virus Variants that Emerged in Guinea and the Democratic Republic of the Congo in 2014. *Viruses*. 2014;6(11):4760-99.
- Leroy EM, Rouquet P, Formenty P, Souquière S, Kilbourne A, Froment J-M, et al. Multiple Ebola Virus Transmission Events and Rapid Decline of Central African Wildlife. *Science*. 2004;303(5656):387-90.
- Leroy EM, Kumulungui B, Pourrut X, Rouquet P, Hassanin A, Yaba P, et al. Fruit bats as reservoirs of Ebola virus. *Nature*. 2005;438(7068):575-6.
- Audet J, Kobinger GP. Immune evasion in ebolavirus infections. *Viral immunology*. 2015;28(1):10-8.
- Feldmann H, Jones S, Klenk H-D, Schnittler H-J. Ebola virus: from discovery to vaccine. *Nature Reviews Immunology*. 2003;3(8):677-85.
- Hoenen T, Groseth A, Falzarano D, Feldmann H. Ebola virus: unravelling pathogenesis to combat a deadly disease. *Trends in Molecular Medicine*. 2006;12(5):206-15.
- Lee JE, Fusco ML, Hessel AJ, Oswald WB, Burton DR, Saphire EO. Structure of the Ebola virus glycoprotein bound to an antibody from a human survivor. *Nature*. 2008;454(7201):177-82.
- Kimberlin CR, Bornholdt ZA, Li S, Woods VL, MacRae IJ, Saphire EO. Ebolavirus VP35 uses a bimodal strategy to bind dsRNA for innate immune suppression. *Proceedings of the National Academy of Sciences of the United States of America*. 2010;107(1):314-9.
- Murphy K. *Janeway's Immunobiology*. Ney York: Garland Science; 2012.
- Shabman RS, Gulcicek EE, Stone KL, Basler CF. The Ebola Virus VP24 Protein Prevents hnRNP C1/C2 Binding to Karyopherin  $\alpha$ 1 and Partially Alters its Nuclear Import. *The Journal of Infectious Diseases*. 2011;204(Suppl 3):S904-S10.
- Zhang APP, Bornholdt ZA, Liu T, Abelson DM, Lee DE, Li S, et al. The Ebola Virus Interferon Antagonist VP24 Directly Binds STAT1 and Has a Novel,

- Pyramidal Fold. *PLoS Pathogens*. 2012;8(2):e1002550.
- Mohan GS, Li W, Ye L, Compans RW, Yang C. Antigenic Subversion: A Novel Mechanism of Host Immune Evasion by Ebola Virus. *PLoS Pathogens*. 2012;8(12):e1003065.
- Francica JR, Varela-Rohena A, Medvec A, Plesa G, Riley JL, Bates P. Steric Shielding of Surface Epitopes and Impaired Immune Recognition Induced by the Ebola Virus Glycoprotein. *PLoS Pathogens*. 2010;6(9):e1001098.
- Noyori O, Nakayama E, Maruyama J, Yoshida R, Takada A. Suppression of Fas-mediated apoptosis via steric shielding by filovirus glycoproteins. *Biochemical and Biophysical Research Communications*. 2013;441(4):994-8.
- Kaletsky RL, Francica JR, Agrawal-Gamse C, Bates P. Tetherin-mediated restriction of filovirus budding is antagonized by the Ebola glycoprotein. *Proceedings of the National Academy of Sciences of the United States of America*. 2009;106(8):2886-91.
- Geisbert TW, Hensley LE, Larsen T, Young HA, Reed DS, Geisbert JB, et al. Pathogenesis of Ebola Hemorrhagic Fever in Cynomolgus Macaques: Evidence that Dendritic Cells Are Early and Sustained Targets of Infection. *The American Journal of Pathology*. 2003;163(6):2347-70.
- Falasca L, Agrati C, Petrosillo N, Di Caro A, Capobianchi MR, Ippolito G, et al. Molecular mechanisms of Ebola virus pathogenesis: focus on cell death. *Cell Death and Differentiation*. 2015;22(8):1250-9.
- Baize S, Leroy EM, Georges AJ, Georges-Courbot MC, Capron M, Bedjabaga I, et al. Inflammatory responses in Ebola virus-infected patients. *Clinical and Experimental Immunology*. 2002;128(1):163-8.
- Wahl-Jensen VM, Afanasieva TA, Seebach J, Ströher U, Feldmann H, Schnittler H-J. Effects of Ebola Virus Glycoproteins on Endothelial Cell Activation and Barrier Function. *Journal of Virology*. 2005;79(16):10442-50.
- Gire SK, Goba A, Andersen KG, Sealfon RSG, Park DJ, Kanneh L, et al. Genomic surveillance elucidates Ebola virus origin and transmission during the 2014 outbreak. *Science (New York, NY)*. 2014;345(6202):1369-72.
- Park Daniel J, Dudas G, Wohl S, Goba A, Whitmer Shannon LM, Andersen Kristian G, et al. Ebola Virus Epidemiology, Transmission, and Evolution during Seven Months in Sierra Leone. *Cell*. 2015;161(7):1516-26.
- Hughes AL. Micro-scale signature of purifying selection in Marburg virus genomes. *Gene*. 2007;392(1-2):266-72.
- Dunham EC, Banadyga L, Groseth A, Chiramel AI, Best SM, Ebihara H, et al. Assessing the contribution of interferon antagonism to the virulence of West African Ebola viruses. *Nature communications*. 2015;6.
- Mühlberger E, Weik M, Volchkov VE, Klenk H-D, Becker S. Comparison of the Transcription and Replication Strategies of Marburg Virus and Ebola Virus by Using Artificial Replication Systems. *Journal of Virology*. 1999;73(3):2333-42.
- Azarian T, Presti AL, Giovanetti M, Cella E, Rife B, Lai A, et al. Impact of spatial dispersion, evolution, and selection on Ebola Zaire Virus epidemic waves. *Scientific reports*. 2015;5.
- Pickett BE, Sadat EL, Zhang Y, Noronha JM, Squires RB, Hunt V, et al. ViPR: an open bioinformatics database and analysis resource for virology research. *Nucleic Acids Research*. 2012;40(Database issue):D593-D8.
- Walsh MG, Haseeb MA. The landscape configuration of zoonotic transmission of Ebola virus disease in West and Central Africa: interaction between population density and vegetation cover. *PeerJ*. 2015;3:e735.
- Pigott DM, Golding N, Mylne A, Huang Z, Henry AJ, Weiss DJ, et al. Mapping the zoonotic niche of Ebola virus disease in Africa. *eLife*. 2014;3:e04395.
- Chowell G, Nishiura H. Transmission dynamics and control of Ebola virus disease (EVD): a review. *BMC medicine*. 2014;12(1):196.

Research Article

<sup>1</sup>Department of Biochemistry,  
McGill University, Montreal,  
QC, Canada

Keywords

Phosphatase, Pseudophosphatase,  
Post-translational modification,  
Oncoprotein, Membrane trans-  
porter, Structural biology, Pro-  
tein-protein interaction, Active site,  
Enzyme kinetics

Email Correspondence

howie.wu@mail.mcgill.ca

# Dead but not gone: The case for PRL as a pseudo-phosphatase

## Abstract

**Background:** Protein phosphorylation and dephosphorylation is an integral component of many cellular signaling pathways and regulatory mechanisms. Phosphatases are enzymes that catalyze the removal of phosphate groups from proteins. The phosphatases of regenerating liver (PRLs) are a family of phosphatases which have been correlated with cancer development and metastasis. However, they appear to have weak phosphatase activity and little is known about their physiological substrates. This review discusses PRL from a structural and functional perspective, including recent findings on its interaction with another family of proteins, cyclin M (CNNM).

**Methods:** Articles were obtained from the scientific literature using databases like PubMed and McGill University's open access institutional repository. This paper specifically focuses on those articles that provided an overview of phosphatases, PRLs, CNNMs, and structural and functional studies of PRLs and CNNMs. In total, 40 articles were selected for the purpose of this review.

**Summary:** Although PRLs retain many of the structural features of other protein tyrosine phosphatases (PTPs) including the phosphatase catalytic motif and regulation via oxidation, other structural features such as mutation of a conserved serine/threonine residue to alanine in the active site disfavor catalytic activity. Moreover, PRL interaction with CNNM appears to be responsible for its oncogenic potential, yet this interaction does not appear to require PRL phosphatase activity. Thus, PRL may be best classified as a pseudo-phosphatase, which are phosphatase-like proteins that are structurally similar to phosphatases but have acquired a dominant function that does not require phosphatase activity.

## Introduction

Protein phosphorylation is a key post-translational modification that is involved in the regulation of protein structure and function. Two classes of protein kinases, serine/threonine kinases and tyrosine kinases, catalyze the majority of phosphorylation reactions. (1) However, there are also two classes of protein phosphatases: protein serine/threonine phosphatases and protein tyrosine phosphatases (PTPs) (Fig. 1), which both mediate the dephosphorylation of proteins. (2) Both phosphorylation and dephosphorylation play critical roles in cellular signaling pathways, enzyme regulation, and protein diversity. (3)

Protein phosphatases are grouped into several classes, the largest of which are the PTPs. This class consists of the classical PTPs and the dual-specificity phosphatases (DUSPs), which can dephosphorylate both tyrosine and serine/threonine residues. (4) Examples of classical phosphatases include tyrosine-protein phosphatase non-receptor type 1 (PTP1B), which can dephosphorylate phospho-tyrosine sites on the insulin receptor kinase (5), and receptor-like protein-tyrosine phosphatase (RPTP $\alpha$ ), which has been implicated in the activation of the protein-tyrosine kinase c-Src. (6) Members of the DUSPs include phosphatase and tensin homolog (PTEN), which dephosphorylates both polypeptide and phosphatidylinositol substrates (7), and VHR-related (VHR), which dephosphorylates phospho-tyrosine and phospho-threonine residues on c-Jun N-terminal kinase (JNK) to downregulate apoptosis-associated signaling. (8) The three phosphatases of regenerating liver (PRL1-3) are also classified as DUSPs, and although investigations have shown that PRL expression is correlated with various cancers (9, 10), there is no consensus on the physiological substrates of the PRLs. Detailed reviews of the PRLs in cancer and studies of PRL substrates can be found in Bessette et al. (11) and Rios et al. (12), respectively. Although PRLs share many similarities with the other DUSPs, there are key differences in their structure and function which suggest that PRLs may not function in vivo as phosphatases. This is supported by recent results that show another protein, cyclin M (CNNM), can bind to PRLs (13, 14) while structural studies of this interaction suggest that this

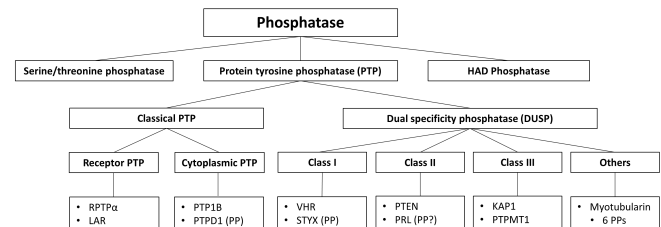


Fig. 1: Classification of protein phosphatases. Major families and subfamilies are shown with examples of phosphatases from each PTP subfamily. Those phosphatases which have been identified as pseudophosphatases are labelled in brackets with "PP". Although PRLs are not generally classified as pseudophosphatases, they share characteristics of pseudophosphatases: weak catalytic activity and a role in mediating protein-protein interactions.

interaction may not be dependent on PRL phosphatase activity. (15) In this review, I use structural and functional considerations to suggest that PRLs may be best classified as pseudophosphatases.

## Structure Characteristics of PRLs and the Other PTPs

One feature of cysteine-based PTPs like PRLs is the presence of the phosphatase signature motif, HCXXGXXR, in the active site of the enzyme. (7) The cysteine residue in this motif mediates a nucleophilic attack on the phosphate group attached to the substrate, forming a phospho-enzyme intermediate and releasing the dephosphorylated substrate. (16) A conserved aspartic acid residue in a neighboring WPD loop is involved in protonation of the dephosphorylated substrate and in subsequent activation of a water molecule by deprotonation, leading to regeneration of the

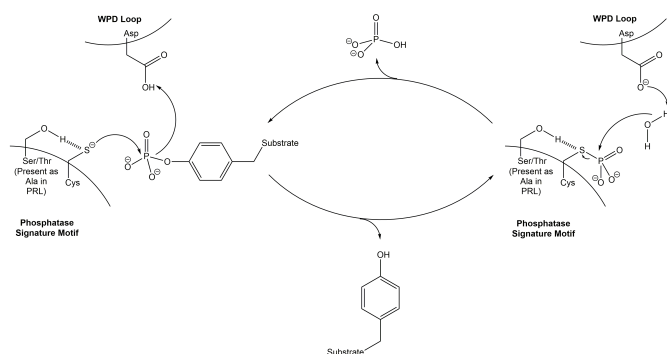


Fig. 2. Mechanism of dephosphorylation by PTPs. A conserved cysteine residue in the signature motif mediates nucleophilic attack and removal of the phosphate group from the substrate. Then, a conserved aspartate residue in the WPD loop activates a water molecule for regeneration of the active enzyme. A conserved serine/threonine residue in the catalytic pocket also stabilizes the catalytic cysteine residue.

active enzyme (Fig. 2). (17)

The size of the catalytic pocket of PTPs is also responsible for conferring substrate specificity. In PTP1B, the catalytic pocket is approximately 9 Å in depth, which corresponds well with the length of a phospho-tyrosine residue. (18) On the other hand, in the case of most DUSPs, the catalytic pocket is relatively shallow, and this feature is thought to confer the ability to dephosphorylate the shorter phospho-serine and phospho-threonine residues. PRLs have particularly shallow catalytic pockets, with the pocket of PRL-3 being the shallowest of the known phosphatases. (19) Conversely, PTEN has a large catalytic pocket even though it is a DUSP, and this is consistent with PTEN's ability to dephosphorylate the larger PI(3,4,5)P<sub>3</sub> substrate. (7) Thus, the depth of the catalytic pocket is indicative of the size of the phosphatase substrate, and in regard to PRL, the relatively shallow pocket appears to predict broad substrate specificity.

The physical and chemical characteristics of the residues in and around the active site are also responsible for PTP substrate specificity. For example, PTP1B is known to dephosphorylate the insulin receptor kinase at a region with tandem phospho-tyrosine residues. (20) While the first phospho-tyrosine interacts with the active site of PTP1B, another groove in PTP1B near the active site binds to the second phospho-tyrosine residue, thus conferring greater affinity for the tandemly phosphorylated site in insulin receptor kinase. (20) Interestingly, the G129E mutation of PTEN, observed in Cowden syndrome (18), abolishes lipid phosphatase activity but not protein phosphatase activity. (21) Thus, G129 appears to be responsible for the distinctive ability of PTEN to dephosphorylate PI(3,4,5)P<sub>3</sub>. The active site of PRLs, unlike the basic active sites of other DUSPs like PTEN and VHR, is unusually hydrophobic. (19) Although this predicts a preference for hydrophobic substrates, there has been no conclusive evidence identifying such substrates of PRLs.

One feature particular to PRLs is their slow enzymatic activity, which is thought to be the result of a mutation of the conserved serine/threonine in the PTP active site to alanine in PRLs (Fig. 2). (19) This eliminates the stabilizing hydrogen bonding interactions that normally occur between the serine/threonine and the catalytic thiolate intermediate (Fig. 2). (22) Therefore, the phosphatase activity of PRLs appears to be either intrinsically low or binding to physiological substrates may be required for sufficient PRL enzymatic activity. Studies with PRL-1 and PRL-3 also show that regeneration of the enzyme is the rate-limiting step, resulting in a relatively long-lived phospho-enzyme intermediate. (19, 23) In fact, due to its stability, this phospho-enzyme intermediate may be better viewed as a phosphorylated variant of PRL, where phosphorylation acts as a post-translational modification rather than as a transient step in the catalytic mechanism.

Like many of the other PTPs and DUSPs, PRL appears to be regulated by redox reactions that occur at its catalytic cysteine residue. Several studies have demonstrated that PRLs can form an intramolecular disulfide bond

between its catalytic cysteine residue and a neighboring cysteine residue (C49 in PRL-1 and PRL-3, C46 in PRL-2). (13, 14, 19, 23) Similar disulfide bond formation in other DUSPs like KAP (24) and PTEN (25) is associated with a loss of catalytic activity. One contributing factor to the prevalence of the disulfide bond is the comparatively low pK<sub>a</sub> of the catalytic cysteine residue in the active site, which leaves the cysteine prone to oxidation. (26) In fact, even in PTPs where disulfide bond formation is not observed, oxidation of the catalytic cysteine still occurs. In PTP1B, the catalytic cysteine reacts with the backbone nitrogen of the adjacent serine residue to form a sulfenyl-amide bond. (27, 28) This sulfenyl-amide is thought to prevent irreversible oxidation and inactivation of the catalytic cysteine to the sulfinic or sulfonic acid species. Thus, oxidation of PTPs, although inactivating catalytic activity, also serves a protective role.

The structural features of PRLs, particularly the mutation of the conserved PTP serine/threonine residue to alanine, the shallow catalytic pocket, and the susceptibility of the catalytic cysteine residue to oxidation, predict weak and indeterminate phosphatase activity. Thus, based on structural considerations, PRL does not appear to be particularly suited to function as a phosphatase. However, as will be seen later, this does not mean that PRL cannot act at all as a phosphatase, and only with consideration of functional properties does PRL's status as a pseudophosphatase become clear.

## PRLs as Pseudophosphatases

Pseudophosphatases are broadly defined as phosphatases that lack catalytic activity. In the majority of cases, this is due to the mutation of conserved residues of the phosphatase signature motif. For example, in the pseudophosphatase, STYX, the catalytic cysteine is replaced by a glycine residue. (29) Moreover, the presence of tandem PTP domains with an active domain closer to the membrane (D1) and an inactive pseudophosphatase domain farther from the membrane (D2) is conserved throughout the receptor protein tyrosine phosphatases (RPTPs). Although the function of the D2 domain has not been well-characterized, it is thought to have a role in regulation of the D1 domain. In LAR, the D2 domain can lower the catalytic activity of the D1 domain and can regulate the type of substrates to which the D1 domain can bind. (30) In contrast, in another RPTP found in *Drosophila*, PTP99A, the presence of the D2 domain augments the catalytic activity of the D1 domain. (30) Moreover, the D2 domain appears to have greater sensitivity to oxidation than the D1 domain, which postulates a redox-sensing role for this domain in the function of RPTPs. (31) Although pseudophosphatases may not have catalytic activity, their structural similarity to active phosphatases makes them susceptible to many of the regulatory modifications, such as oxidation, seen in active phosphatases.

Although pseudophosphatases have been classified as so because of lack of catalytic activity, this criterion is not very robust. Pseudophosphatases that lack catalytic activity *in vivo* can show catalytic activity *in vitro* or vice versa. (32) Moreover, some pseudophosphatases such as PTPN14 do not have a mutation at the catalytic cysteine residue, and their classification as pseudophosphatases is primarily due to undetected phosphatase activity. (33) This does not exclude the existence of physiologically relevant substrates, and another possibility is that the protein may have a dominant function that does not involve phosphatase activity. Further studies have found that PTPN14 binds in a phosphatase-independent manner to another oncoprotein, YAP1, in order to inhibit its activity. (34) Therefore, an alternative classification of a pseudophosphatase would not focus solely on lack of catalytic activity, but rather on the dominance of some other function of the phosphatase, such as protein-protein interaction, over the expected phosphatase activity of the enzyme.

Like PTPN14, PRLs also have low *in vitro* phosphatase activity even though there is no mutation of the catalytic cysteine residue. (15, 19) The substitution of the conserved serine/threonine residue in the phosphatase signature motif of other PTPs to alanine in PRL may confer such low enzymatic activity (15, 19) that PRL phosphatase activity becomes essentially nonexistent. Recent studies are now revealing that PRL binding and inhibition of a class of putative magnesium transporters, CNNMs, may be the predominant PRL activity in cells. (13, 14) Features which were thought to be a consequence of PRL phosphatase activity such as the long-lived phos-

phorylated intermediate and redox regulation now appear to be responsible for mediating the binding of PRLs to CNNMs.

## PRL and CNNM: The Developing Story

CNNMs were originally termed ancient conserved domain proteins (ACDP). The family has four members (CNNM1-CNNM4), and each member consists of a transmembrane region, a cystathionine  $\beta$ -synthase pair (CBS-pair) domain, a cyclin box motif, and a cNMP-binding domain. (35) The presence of the cyclin box motif initially suggested these proteins were involved in regulation of the cell cycle, hence the name, cyclin M (CNNM). (35) The role of these proteins, however, in the cell cycle has not been fully characterized, and the CNNM proteins have been found to localize primarily to the plasma membrane. (36) Homology to  $Mg^{2+}$  transport proteins like CorC and MgtE along with recent functional studies postulate a  $Mg^{2+}$  transport role for the CNNM family. (14, 19, 36, 37) There is disagreement, however, about whether CNNM mediates  $Mg^{2+}$  efflux (38) or  $Mg^{2+}$  influx (14). Nonetheless, experiments show that PRL can bind to CNNM and that this protein-protein interaction causes an increase in intracellular  $Mg^{2+}$  levels by either inhibiting  $Mg^{2+}$  efflux (13) or by stimulating  $Mg^{2+}$  influx (14). Since  $Mg^{2+}$  is linked to cellular energy state and to the activation of processes that lead to cancer development (39), PRL binding to CNNM and subsequent increase in intracellular  $Mg^{2+}$  affords one explanation for the correlation between PRL and cancer. (9, 10) Notably, this explanation does not require the phosphatase activity of PRL.

Results from structural studies reveal that PRL binds to CNNM via its phosphatase catalytic pocket. (15) Since this interaction effectively blocks off the PRL catalytic pocket, it is unlikely that PRL would be able to function as a phosphatase for other substrates when bound to CNNM. Furthermore, the binding between PRL and CNNM can be modulated by oxidation of the PRL catalytic cysteine residue since a decrease in binding affinity is observed when PRL is placed in oxidizing conditions. (11, 12) These results suggest that structural modifications on PRL traditionally associated with its role as a phosphatase may also influence its interaction with CNNM. Further studies are needed to determine if PRL catalytic activity is dispensable in its biological function.

## Conclusion

The term 'pseudophosphatase', while formally denoting those phosphatases that lack catalytic activity, is in reality ambiguous and often open to interpretation in its application. There are examples of 'pseudophosphatases' that show catalytic activity towards small molecule substrates yet not towards larger synthetic peptides. (40) Moreover, it is not entirely accurate to infer catalytic activity using synthetic substrates. The structure of many phosphatases require specific interactions with properly shaped physiological substrates before manifestation of any catalytic activity.

On the other hand, there are phosphatases like PRL for which it appears some other function has taken precedence over phosphatase activity. The term 'pseudophosphatase' would best be applied to these proteins. For one, they may still retain catalytic activity, which in the case of PRL is observable in vitro albeit very slow. More importantly though, this classification would come with a recognition that this group of phosphatases, while similar to traditional protein phosphatases in structure, have a completely different function. For PRL, this function appears to come from its interactions with CNNM, a class of ion transporters. From what is currently known, PRL interaction with CNNM could potentially be a significant player in regulation of cellular energy state through  $Mg^{2+}$  levels. Thus, PRLs, once viewed as laggard members of the PTP family, have now been shown to have a completely different side - one which promises to be a source of intrigue in the future.

## Acknowledgements

I would like to thank Dr. Kalle Gehring for having me in his laboratory to

conduct my undergraduate honours project and for guiding me through this review. I would also like to thank the Natural Sciences and Engineering Research Council of Canada (NSERC) for funding me during the summer with an Undergraduate Student Research Award while I was working on the project.

## References

1. Hanks S, Quinn A, Hunter T. The protein kinase family: conserved features and deduced phylogeny of the catalytic domains. *Science*. 1988;241(4861):42-52.
2. Tonks NK. Protein tyrosine phosphatases—from housekeeping enzymes to master regulators of signal transduction. *FEBS Journal*. 2013;280(2):346-78.
3. Hunter T. Protein kinases and phosphatases: The Yin and Yang of protein phosphorylation and signaling. *Cell*. 1995;80(2):225-36.
4. Kharitidi D, Manteghi S, Pause A. Pseudophosphatases: methods of analysis and physiological functions. *Methods*. 2014;65(2):207-18.
5. Seely BL, Staubs PA, Reichart DR, Berhanu P, Milarski KL, Saltiel AR, et al. Protein tyrosine phosphatase 1B interacts with the activated insulin receptor. *Diabetes*. 1996;45(10):1379-85.
6. Tracy S, van der Geer P, Hunter T. The Receptor-like Protein-tyrosine Phosphatase, RPTP, Is Phosphorylated by Protein Kinase C on Two Serines Close to the Inner Face of the Plasma Membrane. *Journal of Biological Chemistry*. 1995;270(18):10587-94.
7. Lee JO, Yang H, Georgescu MM, Di Cristofano A, Maehama T, Shi Y, et al. Crystal structure of the PTEN tumor suppressor: implications for its phosphoinositide phosphatase activity and membrane association. *Cell*. 1999;99(3):323-34.
8. Todd JL, Rigas JD, Rafty LA, Denu JM. Dual-specificity protein tyrosine phosphatase VHR down-regulates c-Jun N-terminal kinase (JNK). *Oncogene*. 2002;21(16):2573-83.
9. Bardelli A, Saha S, Sager JA, Romans KE, Xin B, Markowitz SD, et al. PRL-3 expression in metastatic cancers. *Clinical Cancer Research*. 2003;9(15):5607-15.
10. Wang Q, Holmes DI, Powell SM, Lu QL, Waxman J. Analysis of stromal-epithelial interactions in prostate cancer identifies PTPCAAX2 as a potential oncogene. *Cancer Letters*. 2002;175(1):63-9.
11. Bessette D, Qiu D, Pallen C. PRL PTPs: mediators and markers of cancer progression. *Cancer Metastasis Rev*. 2008;27(2):231-52.
12. Rios P, Li X, Köhn M. Molecular mechanisms of the PRL phosphatases. *FEBS Journal*. 2013;280(2):505-24.
13. Funato Y, Yamazaki D, Mizukami S, Du L, Kikuchi K, Miki H. Membrane protein CNNM4-dependent  $Mg^{2+}$  efflux suppresses tumor progression. *The Journal of Clinical Investigation*. 2014;124(12):5398-410.
14. Hardy S, Uetani N, Wong N, Kostantin E, Labbe DP, Begin LR, et al. The protein tyrosine phosphatase PRL-2 interacts with the magnesium transporter CNNM3 to promote oncogenesis. *Oncogene*. 2015;34(8):986-95.
15. Gulerez IE. Structural Characterization of the Complex between the Oncogenic Phosphatase PRL2 and the CBS pair domain of the Magnesium Transporter CNNM3. McGill University; 2015.
16. Gulerez IE, Gehring K. X-ray crystallography and NMR as tools for the study of protein tyrosine phosphatases. *Methods*. 2014;65(2):175-83.
17. Andersen JN, Mortensen OH, Peters GH, Drake PG, Iversen LF, Olsen OH, et al. Structural and Evolutionary Relationships among Protein Tyrosine Phosphatase Domains. *Molecular and Cellular Biology*. 2001;21(1):7117-36.
18. Jia Z, Barford D, Flint AJ, Tonks NK. Structural basis for phosphotyrosine peptide recognition by protein tyrosine phosphatase 1B. *Science*. 1995;268(5218):1754-8.
19. Kozlov G, Cheng J, Ziomek E, Banville D, Gehring K, Ekiel I. Structural insights into molecular function of the metastasis-associated phosphatase PRL-3. *The Journal of Biological Chemistry*. 2004;279(12):11882-9.
20. Salmeen A, Andersen JN, Myers MP, Tonks NK, Barford D. Molecular basis for the dephosphorylation of the activation segment of the insulin receptor by protein tyrosine phosphatase 1B. *Molecular Cell*. 2000;6(6):1401-12.
21. Myers MP, Pass I, Batty IH, Van der Kaay J, Stolarov JP, Hemmings BA, et al. The lipid phosphatase activity of PTEN is critical for its tumor suppressor function. *Proceedings of the National Academy of Sciences of the United States of America*. 1998;95(23):13513-8.
22. Denu JM, Dixon JE. A catalytic mechanism for the dual-specific phosphatases. *Proceedings of the National Academy of Sciences of the United States of America*. 1995;92(13):5910-4.
23. Sun JP, Wang WQ, Yang H, Liu S, Liang F, Fedorov AA, et al. Structure and biochemical properties of PRL-1, a phosphatase implicated in cell growth, differentiation, and tumor invasion. *Biochemistry*. 2005;44(36):12009-21.
24. Song H, Hanlon N, Brown NR, Noble MEM, Johnson LN, Barford D. Phosphoprotein-Protein Interactions Revealed by the Crystal Structure of Kinase-Associated Phosphatase in Complex with PhosphoCDK2. *Molecular*

- Cell. 2001;7(3):615-26.
25. Lee SR, Yang KS, Kwon J, Lee C, Jeong W, Rhee SG. Reversible inactivation of the tumor suppressor PTEN by H<sub>2</sub>O<sub>2</sub>. *The Journal of Biological Chemistry*. 2002;277(23):20336-42.
  26. Tonks NK. Protein tyrosine phosphatases: from genes, to function, to disease. *Nat Rev Mol Cell Biol*. 2006;7(11):833-46.
  27. Salmeen A, Andersen JN, Myers MP, Meng T-C, Hinks JA, Tonks NK, et al. Redox regulation of protein tyrosine phosphatase 1B involves a sulphanyl-amide intermediate. *Nature*. 2003;423(6941):769-73.
  28. van Montfort RLM, Congreve M, Tisi D, Carr R, Jhoti H. Oxidation state of the active-site cysteine in protein tyrosine phosphatase 1B. *Nature*. 2003;423(6941):773-7.
  29. Wishart MJ, Denu JM, Williams JA, Dixon JE. A Single Mutation Converts a Novel Phosphotyrosine Binding Domain into a Dual-specificity Phosphatase. *Journal of Biological Chemistry*. 1995;270(45):26782-5.
  30. Madan LL, Veeranna S, Shameer K, Reddy CCS, Sowdhamini R, Gopal B. Modulation of Catalytic Activity in Multi-Domain Protein Tyrosine Phosphatases. *PLoS ONE*. 2011;6(9):e24766.
  31. Persson C, Sjöblom T, Groen A, Kappert K, Engström U, Hellman U, et al. Preferential oxidation of the second phosphatase domain of receptor-like PTP- $\alpha$  revealed by an antibody against oxidized protein tyrosine phosphatases. *Proceedings of the National Academy of Sciences of the United States of America*. 2004;101(7):1886-91.
  32. Reiterer V, Eyers PA, Farhan H. Day of the dead: pseudokinases and pseudophosphatases in physiology and disease. *Trends in Cell Biology*. 2014;24(9):489-505.
  33. Zhu JH, Chen R, Yi W, Cantin GT, Fearn C, Yang Y, et al. Protein tyrosine phosphatase PTPN13 negatively regulates Her2/ErbB2 malignant signaling. *Oncogene*. 2007;27(18):2525-31.
  34. Wang W, Huang J, Wang X, Yuan J, Li X, Feng L, et al. PTPN14 is required for the density-dependent control of YAP1. *Genes & Development*. 2012;26(17):1959-71.
  35. Wang C-Y, Shi J-D, Yang P, Kumar PG, Li Q-Z, Run Q-G, et al. Molecular cloning and characterization of a novel gene family of four ancient conserved domain proteins (ACDP). *Gene*. 2003;306:37-44.
  36. de Baaij JHF, Stuver M, Meij IC, Lainez S, Kopplin K, Venselaar H, et al. Membrane Topology and Intracellular Processing of Cyclin M2 (CNNM2). *Journal of Biological Chemistry*. 2012;287(17):13644-55.
  37. Corral-Rodriguez MA, Stuver M, Abascal-Palacios G, Diercks T, Oyenarte I, Ereno-Orbea J, et al. Nucleotide binding triggers a conformational change of the CBS module of the magnesium transporter CNNM2 from a twisted towards a flat structure. *The Biochemical Journal*. 2014;464(1):23-34.
  38. Yamazaki D, Funato Y, Miura J, Sato S, Toyosawa S, Furutani K, et al. Basolateral Mg<sup>2+</sup> Extrusion via CNNM4 Mediates Transcellular Mg<sup>2+</sup> Transport across Epithelia: A Mouse Model. *PLoS Genet*. 2013;9(12):e1003983.
  39. Castiglioni S, Maier JA. Magnesium and cancer: a dangerous liason. *Magnesium Research*. 2011;24(3):92-100.
  40. Barr AJ, Ugochukwu E, Lee WH, King ON, Filippakopoulos P, Alfano I, et al. Large-scale structural analysis of the classical human protein tyrosine phosphatome. *Cell*. 2009;136(2):352-63.